SCUOLA DI DOTTORATO

UNIVERSITÀ DEGLI STUDI DI MILANO-BICOCCA

Department of Materials Science
PhD school in Materials Science and Nanotechnology
Cycle XXXVII

Green fabrication of biodegradable biopolymer carriers of radioisotopes and markers for personalized internal radiotherapy and diagnostics

Giulia Tamburini
790364

Supervisor: Prof. Alberto Paleari
Co-supervisor: Prof. Roberto Lorenzi
Coordinator: Prof. Francesco Montalenti

ACADEMIC YEAR 2023/2024

Abstract

The need for innovative solutions is driving the rapid development of biomedical science and materials science to address the pressing challenges in medicine. Among these, the diagnosis and treatment of cancer, in particular hepatocellular carcinoma (HCC), continues to be a significant global concern. This research addresses these challenges by developing biodegradable biopolymer carriers for radioisotopes, focusing on their application in personalized internal radiotherapy and diagnostics.

Recent advancements in imaging technologies, including MRI, CT, and PET, have significantly enhanced the precision of tumor localization and characterization, thereby establishing the foundation for targeted therapeutic strategies. However, conventional cancer treatments frequently encounter limitations, including toxicity, inefficiencies, and restricted targeting capabilities. Selective Internal Radiation Therapy (SIRT) has emerged as a promising alternative, employing radiolabeled microspheres to deliver localized radiation directly to tumors. This method significantly minimizes collateral damage to healthy tissues and enhances therapeutic efficacy. The efficacy of SIRT depends on developing microspheres that exhibit optimal properties, including biocompatibility, stability, and effective radiation delivery.

This thesis investigates the potential of poly(lactic acid) (PLA), a biodegradable and biocompatible polymer derived from renewable resources, as a material for fabricating these microspheres. The physicochemical properties of PLA, including its thermal stability, crystallinity, and controlled degradation, contribute to its versatility for biomedical applications. Experimental investigations have been conducted to understand the effects of radiation on the molecular structure and thermal behavior of PLA, providing valuable insights into its suitability for therapeutic use. Additionally, the study examines how synthesis parameters influence the size, crystallinity, and stability of PLA-based microspheres, emphasizing the importance of precise processing techniques in optimizing their performance.

The thesis also introduces an innovative approach by incorporating europium, a rare-earth element, into PLA microspheres to mimic the presence of a radioisotope. This modification alters the microspheres' structural, morphological, and thermal properties. Detailed spectroscopic analyses elucidate the interactions between the polymer matrix and europium that form cross-links between the chains and make the material more resistant to both the hydrolytic and radiation degradation mechanisms.

PLA microspheres can be customized to fulfill the specific needs of targeted therapies and diagnostics. The findings presented here contribute to developing innovative materials for SIRT, addressing the challenges in cancer therapy and using greener and more sustainable healthcare solutions. The outcomes advance the radiotherapeutic systems field and set the stage for future innovations in personalized medicine and sustainable biomedical technologies.

Riassunto

La crescente necessità di soluzioni innovative sta accelerando lo sviluppo della scienza biomedica e della scienza dei materiali per affrontare le sfide emergenti della medicina. In particolare, la diagnosi e il trattamento del cancro, in particolare del carcinoma epatocellulare (HCC), continuano a rappresentare una preoccupazione significativa a livello globale. Questa ricerca affronta tali sfide sviluppando vettori biodegradabili per radioisotopi, con un focus sulla loro applicazione nella diagnostica e nella radioterapia interna personalizzata. I recenti progressi nelle tecnologie di imaging, come la risonanza magnetica (RM), la tomografia computerizzata (TC) e la tomografia a emissione di positroni (PET), hanno migliorato notevolmente la precisione nella localizzazione e caratterizzazione dei tumori, creando così le basi per strategie terapeutiche mirate. Tuttavia, i trattamenti antitumorali convenzionali presentano tuttora diversi limiti, tra cui tossicità, inefficienza e capacità di targeting limitata. La radioterapia interna selettiva (SIRT) si è proposta come una valida alternativa, che impiega microsfere radiomarcate per somministrare radiazioni localizzate direttamente ai tumori. Questo approccio riduce significativamente i danni collaterali ai tessuti sani e migliora l'efficacia terapeutica. Quest'ultima dipende dalla realizzazione di microsfere con proprietà ottimali, come biocompatibilità, stabilità e somministrazione efficace di radiazioni. Questa tesi esplora il potenziale del poli(acido lattico) (PLA), un polimero biodegradabile e biocompatibile derivato da risorse rinnovabili, come materiale per la produzione di microsfere per applicazioni terapeutiche. Le sue proprietà fisico-chimiche, tra cui stabilità termica, cristallinità e degradazione controllata, contribuiscono alla sua versatilità per le applicazioni biomediche. Sono state condotti studi sperimentali per valutare e comprendere gli effetti delle radiazioni sulla struttura molecolare e sul comportamento termico del PLA, fornendo preziose indicazioni sulla sua idoneità all'uso terapeutico. Inoltre, la ricerca ha esaminato come i parametri di sintesi influenzino dimensioni, cristallinità e stabilità delle microsfere a base di PLA, evidenziando l'importanza di precise tecniche di produzione per ottimizzarne le prestazioni. Un aspetto innovativo della tesi è l'incorporazione dell'europio, un elemento delle terre rare, nelle microsfere di PLA per simulare la presenza di un radioisotopo. Questa modifica altera le proprietà strutturali, morfologiche e termiche delle microsfere. Analisi spettroscopiche dettagliate hanno rivelato le interazioni tra la matrice polimerica e l'europio, che forma legami a ponte tra le catene del polimero, conferendo al materiale maggiore resistenza alla degradazione idrolitica e da radiazioni. Le microsfere di PLA possono essere progettate e personalizzate per rispondere alle esigenze specifiche di terapie e diagnostica mirate. I risultati di questa tesi contribuiscono allo sviluppo di materiali innovativi per la SIRT, affrontando le sfide della terapia del cancro e proponendo soluzioni terapeutiche più ecologiche e sostenibili. Gli esiti di questo studio fanno avanzare il campo dei sistemi radioterapici e pongono le basi per future innovazioni nella medicina personalizzata e nelle tecnologie biomediche sostenibili.

Contents

List of Acronyms

ATR-FTIR Attenuated Total Reflectance Fourier Transform IR

DCM Dichloromethane

DMC Dimethylcarbonate

DSC Differential Scanning Calorimetry

Eu(acac)$_3$ Europium(III) acetylacetonate

EXAFS Extended X-ray Absorption Fine Structure

GIXD Grazing Incidence X-ray Diffraction

HCC Hepatocellular carcinoma

micro-CT Micro Computed Tomography

MRI Magnetic Resonance Imaging

MS Microsphere

NMR Nuclear Magnetic Resonance

PBS Phosphate Buffer Saline

PDLA Poly(D-lactic acid)

PET Positron Emission Tomography

PLA Poly(lactic acid)

PLLA Poly(L-lactic acid)

PVA Poly(vynil alcohol)

PXRD Powder X-ray Diffraction

SEM Scanning Electron Microscopy

SIRT Selective Internal Radiation Therapy

$\mathbf{T}_{cc}$ Cold crystallization temperature

$\mathbf{T}_{emu}$ Emulsification temperature

$\mathbf{T}_{g}$ Glass transition temperature

TGA Thermogravimetric Analysis

$\mathbf{T}_{m}$ Melting temperature

XRF X-ray Fluorescence

Part I

State-of-the-art

OVERVIEW

Biomedical science and materials engineering fields are rapidly evolving, primarily due to the need for advanced solutions to various medical challenges. Tumor diagnosis and therapy, along with the development of biocompatible materials, are the core research areas with great impact on human life and health. This thesis explores the emerging developments in these fields, focusing on the state of the art in diagnostic and therapeutic interventions and the use of new biomaterials for medical applications.

In the field of oncology, improvements in diagnostic and therapeutic modalities have increased the accuracy of detecting and treating tumors. Advances in imaging, molecular diagnostics, and targeted therapies have enhanced life expectancy and contributed to the shift toward more personalized medical treatments. These innovations are crucial for the progress of oncology and for solving the world's cancer problem.

Concurrently shedding light on the expansion of biocompatible polymers, notably polylactic acid (PLA), brings new perspectives on drug delivery and regenerative medicine. PLA, known for its biodegradability and safety, has emerged as one of the key materials in making microspheres for controlled drug delivery, enabling precise targeting and release of therapeutics. Its application also extends to tissue engineering, where it is a scaffold for cell growth and tissue regeneration.

In this regard, Chapter 1 will focus on recent innovations in tumor diagnosis and therapy. It highlights advances in imaging technologies, such as MRI, CT, and PET scan techniques, which have greatly improved the accuracy of tumor localization and characterization. The chapter also covers minimally invasive surgical techniques and radiation therapy developments regarding their increased efficacy and reduced side effects. Nanotechnology-based drug delivery systems and theranostics techniques — a combination of diagnostic and therapeutic — will be examined as innovative tools for improving treatment results.

In chapter 2, the area of polylactic acid (PLA), a biodegradable and biocompatible polymer derived from renewable resources like corn starch and sugarcane, is hereto analyzed. The chapter explores the physicochemical properties of PLA, such as its thermal stability and degradation kinetics, which make it suitable for numerous medical applications. Special emphasis is given to how PLA microspheres are employed in drug delivery systems to achieve a sustained drug release through controlled administration of the drug. The chapter describes various processes, such as spray drying, emulsion methods and solvent evaporation, which are used in fabricating PLA microspheres and their relative effects on the size of the particles, drug encapsulation and release profiles. Finally, an outline of the future perspectives in PLA research, particularly strategies to enhance its functionality and broaden its medical applications, will also be reported.

CHAPTER
ONE

ADVANCES IN TUMOR DIAGNOSIS AND THERAPY

A tumor is an abnormal growth of cells that proliferate uncontrolled, forming a tissue mass. These cells typically originate from a single mutated cell that evades the normal mechanisms of cell growth regulation and continues to divide uncontrollably. Tumors can be benign, meaning they do not invade nearby tissues or spread to other parts of the body, or malignant – also known as cancer – in which case they can invade surrounding tissues and metastasize to distant sites, potentially causing severe health complications. According to the International Agency for Research on Cancer (IARC), there were an estimated 20.0 million new cancer cases worldwide and 9.7 million cancer-related deaths in 2022. Globally, lung cancer tops the list of most diagnosed cancers (12.4% of total cases), followed by female breast (11.6%), colorectal (9.6%), prostate (7.3%), and stomach (4.9%) cancers. Lung cancer also ranks as the leading cause of cancer-related deaths (18.7% of total deaths), followed by colorectal (9.3%), liver (7.8%), female breast (6.9%), and stomach (6.8%) cancers [1].

This thesis will exclusively address primary liver cancer, a condition characterized by the formation of malignant cells within the liver tissue. Hepatocellular carcinoma (HCC) stands as the most prevalent liver tumor, originating from hepatocytes, the liver's primary cell type (Figure 1.1). Its development is attributed to fibrosis and cirrhosis occurring in the setting of chronic liver injury and inflammation. Variations in the racial and geographic distribution of HCC primarily stem from specific risk factors. For instance, regions like Asia and Africa exhibit high prevalence due to hepatitis C and B virus infections. In contrast, the incidence has risen in the US and Western Europe over the past decade, driven by the maturity of hepatitis C and the emergence of non-alcoholic fatty liver disease as a significant risk factor. Notably, HCC's prognosis hinges on both tumor stage and the severity of the underlying liver disease. Curative options, such as liver transplantation and surgical resection, are viable only in the early stages, underscoring the importance of reliable tumor identification methods [2].

1.1 Diagnosis and Imaging tests

Diagnosing cancer involves accurately identifying the malignancy's anatomical origin and the specific type of cells involved. Like other medical conditions, cancer manifests through various signs and symptoms that can be observed directly, via imaging technologies, or confirmed through laboratory tests. The likelihood of successfully treating cancer heavily relies on diagnosing it at an early stage before it grows too large or spreads.

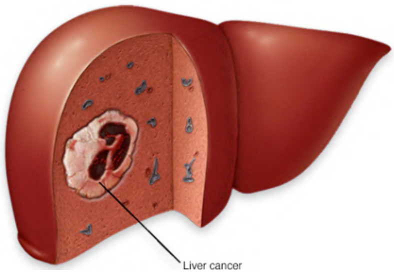

Figure 1.1: Illustration of the section of a liver with HCC.

Early detection depends on several factors: screening high-risk populations, recognizing warning signs by both patients and healthcare providers, and employing diagnostic methods to differentiate cancer from other conditions while also determining the precise location and extent of the tumor.

Modern diagnostic imaging technologies, such as magnetic resonance imaging (MRI) and X-ray computed tomography (CT), can distinguish tissues at a sub-millimeter level, while positron emission tomography (PET) can pinpoint abnormalities within a few millimeters.

Magnetic Resonance Imaging (MRI)

Magnetic resonance imaging (MRI) is a noninvasive medical imaging procedure that generates highly detailed images of nearly all internal structures in the human body, including organs, bones, muscles and blood vessels. By utilizing strong magnets and low-energy radiofrequency signals, MRI scanners gather information from specific atomic nuclei within the body to produce these images. Consequently, MRI does not rely on ionizing radiations for image acquisition [3].

For clinical application ^{1}H, ^{13}C, ^{19}F, ^{23}Na, and ^{31}P, are the most frequently used nuclei. When the patient is submitted to a strong external magnetic field, these spinning nuclei align parallel or antiparallel to it, resulting in a net magnetization vector parallel to the external magnetic field. Radiofrequency pulses at the resonance frequency (Larmor frequency) alter the direction of this net magnetization, allowing the obtainment of information. Switching off the radiofrequency pulses will seek the equilibrium state, and the magnetization decays over time through two different relaxation times, T_1 and T_2, describing decay along the longitudinal and transverse directions, respectively. A magnetic gradient is applied along the main magnetic field in the caudal to cranial direction to select an imaging slice through the body. The local magnetic field strength influences the excitation frequency of spins, allowing only a narrow band of frequencies to excite a thin slice (3-8 mm) of spins. Information for individual points within a slice is obtained using a combination of frequency and phase encoding, forming a grid where each pixel is characterized by specific phase and frequency codes, with intensity represented by frequency amplitude.

MRI has the potential to highlight variations in T_1 and T_2 of human tissues through contrast agents, enhancing the specificity of this technique. As a class of compounds, chelate complexes of paramagnetic metals – Gd^{3+}, Fe^{3+}, Mn^{2+} – serve as effective MRI contrast media by altering the relaxation times of hydrogen nuclei near the metal ions [4]. Although MRI does not emit ionizing radiation, it employs a strong magnetic field that extends beyond the machine and exerts mighty forces on magnetizable objects such as medical implants in the body.

Computed Tomography (CT)

Computed Tomography (CT) is a computerized X-ray imaging procedure that involves rotating a narrow beam of X-rays around the body to produce cross-sectional images known as tomographic images. Once the machine's computer collects several successive slices, they can be digitally stacked together to create a three-dimensional image of the patient, aiding in the identification of basic structures as well as possible tumors or abnormalities [5].

Unlike a conventional X-ray, which uses a fixed X-ray tube, a CT scanner employs a motorized X-ray source that rotates around the circular opening of a toroidal structure called gantry. During a CT scan, the patient lies on a bed that slowly moves through the circular opening in the machine while narrow beams of X-rays are directed through the body. Detectors capture the X-rays as they exit the patient, transmitting the data to a computer for processing. The thickness of each image slice can vary, typically 1-10 mm, depending on the CT machine used.

Contrast agents enhance visibility in X-ray or CT scans, especially for soft tissues that may be faint or challenging to visualize [6]. For instance, an iodine-based intravenous contrast agent is injected into the bloodstream to study the circulatory system and highlight blood vessels. This method is commonly employed to detect potential obstructions in blood vessels, including those near the heart. While CT scans involve ionizing radiation, which poses potential biological risks increasing with cumulative exposure, the overall risk of developing cancer from X-ray radiation exposure is generally low.

Positron Emission Tomography (PET)

Positron emission tomography (PET) is a technique that measures physiological function by observing blood flow, metabolism, neurotransmitters, and radiolabelled drugs. The technique is based on the detection of radioactivity emitted after the injection of a small amount of a radioactive tracer, typically labelled with ^{11}C, ^{13}N, ^{15}O, or ^{18}F, into a peripheral vein. PET can detect biochemical changes in organs or tissues, potentially identifying the onset of a disease process before anatomical changes are visible with other imaging techniques [7].

PET utilizes a scanning device to detect photons emitted by a radionuclide within the organ or tissue under examination. As the scanner moves slowly over the body, positrons are emitted during the breakdown of the radionuclide. When the radiopharmaceutical undergoes beta decay, a positron is emitted, which annihilates with an ordinary electron, emitting two gamma rays in opposite directions. Gamma rays emitted during positron annihilation are captured by two gamma cameras, forming a three-dimensional image. A computer processes this data to create an image map of the studied organ or tissue. The brightness of the tissue in the image correlates with the amount of collected radionuclide, reflecting organ or tissue function levels. PET imaging has been shown to be sensitive enough to detect various cancers, including lung, breast, colorectal, pancreatic, head, and neck cancer, and malignant lymphoma and melanoma [8, 9].

1.2 Liver Cancer Treatments

Presently, cancer treatments include surgical intervention, radiotherapy, chemotherapy, and immunotherapy. Early detection of tumors aids in administering surgical and/or radiotherapeutic interventions. However, for patients with unresectable or irradiation-resistant tumors or those with metastatic conditions, chemotherapy and immunotherapy remain the primary treatment options [10, 11]. Surgical resection is considered the only curative option for HCC or liver-confined metastases. However, only a minority of patients are eligible for this treatment due to factors like lesion size, number, or location. Consequently, hepatic resection is not feasible for most patients. As a result, various palliative local treatment methods such as cryotherapy, radiofrequency, or laser ablation have become increasingly significant. Nonetheless, these methods are only viable for patients with a limited number of small lesions. Unfortunately, by the time of diagnosis, many patients already exhibit advanced liver disease [12]. Moreover, the 5-year survival rate for patients that have undergone liver metastases surgical resection is only around 35%; this already low survival rate worsens due to the majority of tumors being deemed inoperable at the time of diagnosis [13].

Chemotherapy

Chemotherapy for cancer involves cytotoxic chemicals, which possess cell-killing properties, to either eradicate or decrease the tumor burden, thereby alleviating tumor-related symptoms and potentially prolonging life [14]. Typically, cytotoxic drugs are administered intravenously as specified combinations of two or more drugs to increase the possibility of overcoming tumor cell resistance, procuring the activity of the regimen against different tumor cell clones, and avoiding pronounced toxicity from normal tissues.

Unfortunately, only a minority of patients with advanced disease may benefit from cytotoxic drugs that offer a cure for metastatic disease. For some types of tumor, such as prostate cancer, melanoma, or thyroid cancer, the proportion of patients that benefit may be as low as 20%, even when choosing the best established therapeutic regimen. In the case of liver malignancies, patients may not only endure severe side effects impacting their quality of life before experiencing therapeutic benefits but also face challenges related to chemoresistance mechanisms, limiting drug penetration into tumors and leading to resistance development during treatment [15]. Moreover, assessing an individual patient's response to treatment is only possible after several cycles of chemotherapy have been administered.

Immunotherapy

Immunotherapy is the treatment of disease by activating or suppressing the immune system. In the case of cancer treatment, its primary goal is to hinder the metastatic progression of the disease and enhance the quality of life for those affected [16]. Strategies employed in immunotherapy involve either complementing or stimulating the immune system using various compounds, such as bacterial lipopolysaccharides, tumor associated antigens, cytokines, antibodies, and *in vitro*-stimulated effector cells.

Nucleic acid therapeutics, including DNA- or RNA-based vaccines, have emerged as promising alternatives to traditional vaccines and rely on the intracellular delivery of exogenous nucleic acids into target cells [17]. While cell immunotherapy has proven effective in hematologic tumors, its efficacy in solid tumors falls short of expectations due to the heterogeneity within these tumors and their external microenvironment [18].

Radiation Therapy and Selective Internal Radiation Therapy (SIRT)

Radiation therapy, also known as radiotherapy, involves the use of ionizing radiation as a treatment, typically administered as part of cancer therapy to eliminate or manage the proliferation of malignant cells. Radiation therapy can achieve curative outcomes for various types of cancer that are confined to a specific area of the body and have not metastasized. It may also be used as part of adjuvant therapy, employed post-surgery to minimize the risk of tumor recurrence following the removal of a primary malignant tumor. Ionizing radiation disrupts the DNA of cancerous tissue, leading to cellular death. To safeguard normal tissues – such as skin or organs traversed by radiation to reach the tumor site – directed radiation beams are strategically aimed from multiple angles to converge at the tumor, delivering a higher absorbed dose compared to the surrounding healthy tissue [19, 20].

The effectiveness of radiation on cancer is determined by its radiosensitivity. Highly radiosensitive cancer cells are rapidly eliminated with modest radiation doses. However, certain cancers, like renal cell cancer and melanoma, are notably radioresistant, requiring much higher doses for a radical cure, which may not be feasible in clinical practice [21].

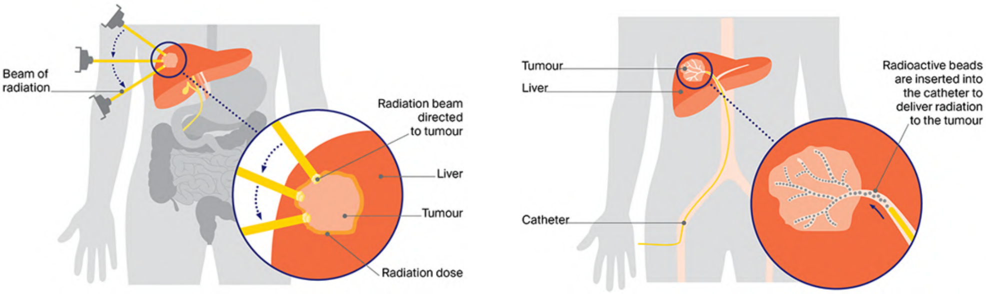

(a) (b)

Figure 1.2: Schematic representation of the application of (a) SBRT and (b) SIRT during treatment on a human patient.

Radiation therapy can be administrated in three different ways:

- *External beam radiation therapy*: also referred to as Stereotactic Body Radiation Therapy (SBRT), it is applied externally via targeted beams of radiation to treat cancer deep within the body (Figure 1.2a). Radiation beams can be produced by several approaches, such as radioactive sources (usually ^{60}Co), high-energy X-rays (4-25 MV), or accelerated particle beams (electrons, protons, or heavy ions).
- *Brachytherapy*: it is applied through the insertion of radiation-emitting sources directly within the tumor or adjacent body cavities. The radiation sources employed can be either permanent, characterized by rapid decay and remaining inside the body, or temporary, involving high-activity sources guided electromechanically to tumors via preplaced catheters and subsequently removed after the complete delivery of the prescribed dose.
- *Radioisotope therapy*: it is applied through the systemic injection of a radioisotope designed to target disease. The most commonly used radioactive elements are ^{131}I, ^{89}Sr, and ^{177}Lu.

Selective Internal Radiation Therapy (SIRT) is a type of microbrachytherapy used to treat liver cancer, whether it originates in the liver or has spread there from other parts of the body (Figure 1.2b). SIRT combines embolization, which involves blocking the tumor's blood supply, with internal radiation therapy delivered via radioactive beads placed directly in the body. These tiny beads, typically made of resin or glass, contain a rare earth radioisotope that becomes radioactive when activated in a neutron flux (typical values of neutron fluence are in the order of $10^{13} cm^{-2} s^{-1}$). Once injected through a catheter into the blood vessels leading to the tumor, these beads deliver targeted radiation to the cancer cells. The radioisotopes in SIRT are both β and γ emitters. The β emissions are highly energetic and used for therapeutic purposes, while γ emissions can be used for imaging techniques such as CT or PET scans to localize the tumor. The application procedure is described in Figure 1.3. This combination of radiation therapy and radionuclide diagnostics is known as *theranostics*. SIRT is often considered for cases of primary liver cancer where surgical removal is not possible or to shrink the tumor before liver resection or transplantation [22].

The following section will be dedicated to a more detailed description of the use of radioactive microspheres in SIRT.

1.3 Radiolabeled microspheres

The term microspheres (MS) describes a general class of particulates with diameters in the high nanometer to micron range and assume a spherical shape, which can be used for various purposes in different fields, especially for diagnostic and therapeutic medical applications. Ideally, MS would be perfectly spherical and uniform in size. However, in practice, their size distribution deviates from this ideal due to variations in the preparation method and the material employed.

The primary application of microspheres in medicine is drug delivery, enabling the administration of therapeutic substances – typically drugs and proteins – into the body and their controlled release. These drug-loaded microspheres can be applied locally or delivered to the target area after intravenous injection. Once the target site is reached, the encapsulated drug is gradually released over the desired period, determined mainly by its biological half-life and release kinetics from the microsphere matrix. This type of

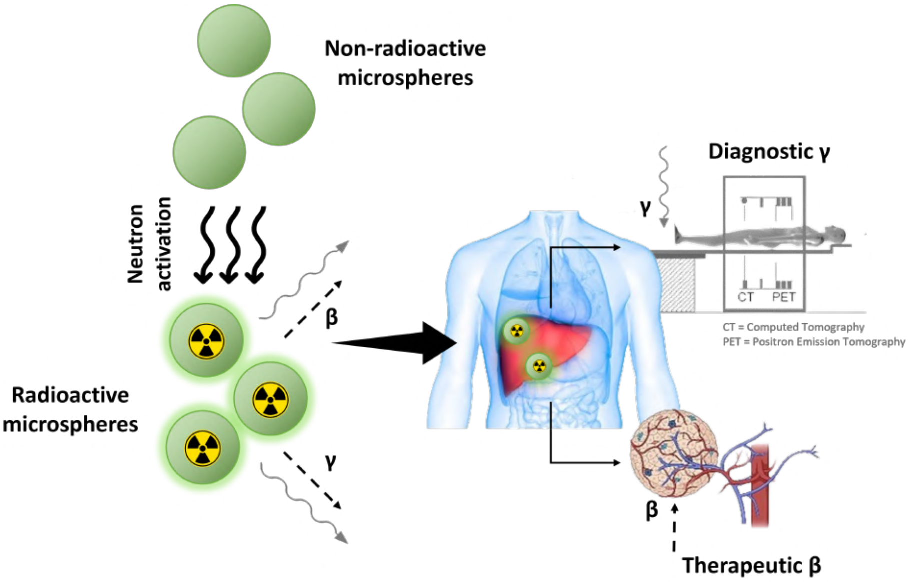

Figure 1.3: Illustration of targeted radioactive tracer delivery using glass microspheres: Initially non-radioactive, the microspheres are activated in a neutron flux to become radioactive. Once injected, they target and bind to specific tumor cells, emitting radiation that can be detected using PET and CT imaging (adapted from [23]).

encapsulated drug delivery system offers the advantage of protecting the enclosed drug from the *in vivo* environment until the time of release, even for very unstable substances such as growth hormones, vaccines, or neuroactive peptides [24, 25]. Microspheres find application in other various fields, including specific cell labeling (especially stem cells) [26], affinity chromatography for antibody isolation in immunology [27], adsorption of toxins in blood [28], diagnostic tests for flow cytometry [29], and tissue engineering [30].

When combined with a radioactive substance, microspheres become *radiolabeled*. Even at low concentrations, these radioactive microspheres are capable of delivering high radiation doses to a target area without damaging the healthy surrounding tissue.

Unlike drugs, the radioactivity remains confined within the microspheres but acts from there over a radioisotope-typical distance, for example, more than tens of millimeters for β-emitters and up to several centimeters for γ-emitters [31]. Nowadays, three types of microspheres are commercially available: yttrium-90 resin microspheres (Sir-Spheres®, Sirtex Medical Ltd., Sydney, Australia), yttrium-90 glass microspheres (Therasphere®, Boston Scientific, Boston, MA, USA) and holmium-166 poly(L-lactic acid) (PLLA) microspheres (QuiremSpheres®, Quirem Medical B.V., Deventer, The Netherlands). Other microspheres have been used but did not reach the level of marketing authorization in Europe, such as rhenium-188 microspheres [32, 33].

Materials and preparation of radiolabeled microspheres

The process of radiolabeling microspheres for intra-arterial therapy can occur either during or after their preparation, depending on when the radioactive material is introduced in the matrix [31]. In the former, commonly employed in medicine, the radioisotope is first activated and then incorporated into the microspheres during the synthesis. Conversely, in the latter approach, the non-radioactive precursor of the radioisotope is initially present and is subsequently activated once encapsulated. This method is preferred, especially for shorter-lived radioisotopes. In such cases, the microspheres can be stored for extended periods of time as part of a sterile, non-radioactive kit and then radiolabeled in a nuclear reactor by bombardment with thermal neutrons shortly before use.

Radiolabeled microspheres should ideally exhibit several important characteristics. These include high mechanical stability to endure passage through the capillary network without breakdown and high chemical stability to resist the elution of the radioactive label, removal by macrophages, or radiolysis. Uniform size is also crucial for consistent delivery and distribution within the target area, while unit density helps prevent settling or streaming, ensuring even distribution. Additionally, relative ease of labeling is desirable for efficient production and application [34].

Choice of the radioisotope

The choice of the radionuclide to be inserted into the microspheres should satisfy very crucial conditions. Firstly, it requires an appropriate radiation spectrum capable of effectively treating tumors of various sizes. Secondly, a high dose rate is advantageous for effective radiobiological effects, making a short half-life preferable. Thirdly, a γ-emitter is necessary for external biodistribution imaging, but with low energy to prevent unnecessary radiation burden to the patient and environment. Additionally, the labeling of particles should be simple without any isotope leakage. Lastly, a large thermal neutron cross-section enables high specific activities within short activation times [35, 36].

Only a few radioisotopes have these characteristics, which make them potentially suitable for the treatment of tumors (see Table 1.1) [31]. Yttrium-90 (^{90}Y) is a clinically acceptable β-emitting radionuclide, useful for therapy due to its energetic emissions (E_{max} = 2.28 MeV). Its half-life of 2.7 days is a reasonable match to the uptake and residence time of many antibodies in tumor. Other valuable characteristics are the maximum travel distance in the soft tissue of 12 mm, and the average radiation penetration range of 2.8 mm, thus presenting little radiation danger to neighboring healthy tissues. Clinical trials of radionuclide therapy using ^{90}Y have been encouraging, resulting in clinically measurable responses even in patients with advanced chemotherapy-resistant breast cancer. However, ^{90}Y presents drawbacks as a radioisotope for therapy, including prolonged activation times (more than two weeks) and inability to produce detectable γ-rays, since it is a pure β-emitter [37].

Rhenium-186 (^{186}Re) and rhenium-188 (^{188}Re) are two other β-emitting radioisotopes with E_{max} = 1.08 and 2.11 MeV, and half-lives of 3.7 days and 16.9 hours, respectively. These rhenium isotopes have similar nuclear and dosimetric properties to ^{90}Y, but the β-decay of the ^{186}Re and ^{188}Re radioisotopes is accompanied by γ emissions with an energy of 137 keV and 155 keV, respectively, making them suitable for *in situ* monitoring of tumor uptake and dosimetry.

Similarly, holmium-166 (^{166}Ho) emits both β-particles (E_{max} = 1.85 MeV) and photons, with a short physical half-life of 26.8 hours, resulting in a high dose rate. It shares comparable cross-section characteristics with rhenium, but its natural abundance of

Table 1.1: Characteristics of radionuclides suitable for therapeutical application from [31].

Radionuclide	Half-life (h)	β_{max} (MeV)	γ (MeV)	Cross-section (barn)
^{32}P	343.2	1.71	-	0.19
^{90}Y	64.1	2.27	-	1.3
^{109}Pd	13.4	1.03	0.088	8.8
^{140}La	40	1.31	0.487	8.9
^{153}Sm	46.8	0.80	0.070	220
^{165}Dy	2.4	1.29	0.095	800
^{166}Ho	26.8	1.84	0.081	64
^{169}Er	230.4	0.34	0.008	2
^{186}Re	90.6	1.07	0.137	110
^{188}Re	17	2.11	0.155	70
^{198}Au	64.8	0.96	0.412	99

100% ensures the formation of only one radioisotope, ^{166}Ho, upon neutron bombardment. Another theranostic radionuclide emitting both β and γ energies is samarium-153 (^{153}Sm) since it has a half-life of 46.3 hours. It can emit β particles with energies of 0.81 MeV (20%), 0.71 MeV (30%), and 0.64 MeV (50%), as well as γ photons with energies of 103 keV [23].

Albumin

Human serum albumin (HSA), commonly referred to as albumin, is a long-circulating and highly abundant protein in the blood and behaves as a natural ligand carrier with multiple cellular receptor binding sites, thus being able to promote the delivery of anti-cancer agents in cells [38]. The colloidal forms of HSA in the particle size range of 100 μm have the potential to be carriers of drugs for targeting specific localization within the body or local application. The bioactive species' release rate from the microspheres can be modified by the particle size, extent of cross-linking, and the position and concentration of drug incorporated in the microspheres. As an example, ^{99m}Tc and ^{188}Re microspheres of HSA have been widely used for clinical nuclear medicine, particularly for lung perfusion imaging, a treatment technique based on the trapping of large particles in the capillary bed of the lung [39]. As well as rhenium and technetium, yttrium can be bounded to HSA for internal radiotherapy, creating ^{90}Y macroaggregates (MAA) of HSA, with dimensions generally in the range 10-30 µm [40].

Different functional groups such as -OH, -NH_2, -SH and -COOH bind specific drugs, radiolabeled chemicals, and chelators to microspheres and introduce other functional groups for further derivatization. These chemical modifications are possible before microsphere preparation but are more commonly performed afterwards. For example, pentetic acid, or diethylenetriaminepentaacetic acid (DTPA), whose conjugate base has a high affinity for metal cations, is frequently used as a chelating molecule for HSA microspheres [41]. DTPA is bounded via an amide bond to albumin using one of the molecule's carboxyl groups, which is able to chelate not only ^{111}In, but also ^{90}Y, ^{99m}Tc, ^{166}Ho, and many other lanthanides.

Resins

Spherical anion and cation exchange resins of different sizes serve as examples of microspheres that can be radiolabeled with ionic radionuclides. These resins are insoluble matrices generally in the form of small (0.25–1.43 µm radius) microbeads fabricated from an organic polymer substrate. The beads are typically porous, providing a large surface area where the trapping of ions occurs along with the accompanying release of other ions, and thus the process is called ion exchange. They achieve labeling efficiencies typically exceeding 95% through simple incubation in saline or aqueous buffer solutions containing the radioisotope, such as chloride salts of holmium and yttrium [42]. However, their stability must be rigorously assessed, as not all resins possess the necessary capacity or binding affinity for radioisotopes like $(^{90}Y)^{3+}$. For instance, the already mentioned SIR-Spheres® are cation exchange resin microspheres labeled with ^{90}Y phosphate, made of sulphuric acid groups attached to a styrene-divinylbenzene copolymer resin (Aminex 50W-X4).

As well as for HSA microspheres, their surface can be modified with chelating agents capable of binding diagnostic and therapeutic radioisotopes. Currently, the most stable and widely used agents are DOTA, also known as tetraxetan, and MAG3. DOTA (1,4,7,10-tetra-azacyclododecane N,N',N",N"'-tetraacetic acid) is a macrocyclic chelator with a 12-membered tetraaza macrocycle ring that is widely used for binding trivalent metals and can complex ^{212}Bi, ^{90}Y, and ^{111}In with over 99% stability for two weeks. MAG3 (mercapto-acetyl-triglycine) is a renal radiopharmaceutical that was introduced as a replacement for ^{131}I o-iodohippurate (OIH), and can complex group VIIB radioisotopes, such as ^{186}Re, ^{188}Re, and ^{99m}Tc with nearly 100% stability in serum over 24 hours [37].

Glass

A practical method to prevent the leakage of radioactive isotopes from microspheres is to encapsulate the radioisotope within the microsphere matrix itself. The process involves enclosing a non-radioactive isotope precursor within pre-fabricated microspheres, which are then activated by thermal neutron bombardment in a nuclear reactor shortly before use. Glass is the most stable matrix for this application. It is highly resistant to radiation damage, insoluble, non-toxic, and can be easily formed into uniform spheres with minimal radionuclidic impurities.

The first attempt to develop such therapeutic radioactive microspheres was the synthesis of aluminosilicate glass containing 17-23 mol% Y_2O_3 (YAS) [43, 44]. These 20-32 μm diameter microspheres produced by spheroidizing YAS glass frit in an acetylene/oxygen flame are characterized by a completely amorphous structure with high shape isometry (particle asphericity below 5%), high chemical stability, and no crystalline inclusions. During neutron activation in the reactor, the non-radioactive ^{89}Y becomes the radioactive β-emitter ^{90}Y. The aluminum and silicon oxides present in the glass base do not form long-lived isotopes when irradiated and impart high chemical stability to the preparation in the internal medium of the body (blood plasma pH 7.4). The leakage rate of the ^{90}Y enclosed in the glass matrix was extremely low (not more than 92 Bq were released from 50 mg of microspheres when activated). These microspheres, registered as TheraSphere®, are already used clinically for treating liver cancer in Canada, the USA., and China. They are being subjected to clinical trials in treating diseased kidneys and spleens, and in the radiation synovectomy of arthritic joints [32, 45].

To reduce the risk of release of ^{90}Y into the organism, YAS microspheres with a core-shell structure were also investigated [46]. This approach focuses on confining the radioisotope within the microsphere's interior by employing controlled ion implantation of the active species, such as phosphorus ions. Alternatively, a hollow porous interior morphology can be engineered to reduce the microsystem's overall weight and mitigate potential side effects, as demonstrated with high-density ceramic Y_2O_3 microspheres [47]. Similarly, glass microspheres have been produced with rhenium, resulting in $^{186/188}$Re microspheres after neutron activation [48].

YAS glass microspheres have shown effectiveness in treating liver cancer, but they come with certain drawbacks. As already mentioned, one key issue is the prolonged neutron activation time required for ^{90}Y, coupled with the inability to use it for imaging, since this radioisotope does not emit γ-rays. Additionally, the relatively high density of these microspheres (3.29 g/mL) and their non-biodegradability present significant disadvantages. The high density increases the risk of intravascular settling in tissues, making complete injection through syringes and intravenous lines more complex. At the same time, the lack of biodegradability may lead to unwanted immunologic reactions in the patient's body [49].

Polymers

The use of polymers for synthesizing microspheres enables the production of uniformly shaped and well-defined spheres in a wide range of sizes. Polymer microspheres are typically made from materials such as poly(lactic-co-glycolic acid) (PLGA), poly(lactic acid) (PLA), or poly(ε-caprolactone) (PCL) [50]. Table 1.2 lists the most commonly used polymers for fabricating microspheres, particularly for medical applications. These materials are chosen for their biocompatibility, degradability, and ability to be processed into uniform spheres. Unlike glass microspheres, polymer microspheres can be designed to degrade over time, reducing the risk of long-term complications. Moreover, the lower density, similar to human plasma (1.025 g/mL), can improve their injectability

Table 1.2: Medical applications of polymeric microspheres from [31]

Mechanism	Matrix
Controlled drug delivery	PLA, PLGA[1], polycyanoacrylate, PMMA[2], PEG[3]
Oral drug delivery of easily degraded drugs	PLGA, styrene, PMMA
Vaccine delivery	PLGA, chitosan
Specific cell labeling	Polystyrene
Adsorption of harmful substances	Polymeric resins, PVA, polyacrylamide
Radioembolization	PVA[4], P(HEMA)[5], PLA
Structure for cell growth	Gelatin, dextran, cellulose, collagen

and reduce the risk of complications during administration. The degradation rate can be controlled by adjusting the polymer composition, which also influences the release profile of the radioactive material. The size of the microspheres is carefully controlled, usually ranging from 20 to 60 μm, to ensure they can selectively lodge in the small blood vessels feeding the tumor without causing a significant blockage in the surrounding vasculature. However, their major disadvantages include their inability to withstand high thermal neutron fluxes during activation; the polymers used should not break down too quickly or lose their structural integrity before delivering the intended dose. The introduction of additives and the adjustment of irradiation parameters can overcome this problem [51].

Polymer-based microspheres used for internal radionuclide therapy are produced using several synthesis methods, each offering distinct benefits and limitations. The solvent evaporation technique is one of the most commonly employed methods [52, 53]. It involves dissolving a polymer in a volatile solvent and dripping this solution into a nonmiscible liquid, i.e. the continuous phase. This phase contains a stabilizer to ensure the formation and maintenance of a spherical shape. As the solvent evaporates, solid mi-

---

[1] poly(lactic-co-glycolic acid)

[2] polymethylmethacrylate

[3] polyethylene glycol

[4] polyvinyl alcohol

[5] poly(2-hydroxyethyl methacrylate)

crospheres form, which are subsequently washed to remove stabilizer residues. The significant advantages of solvent evaporation synthesis of microspheres are its simplicity, compatibility with a wide range of polymers, and high yields. However, it has notable drawbacks, including difficulties in achieving consistent sphere sizes across batches, potentially toxic solvents and stabilizers requiring time-consuming washing, and potential drug loss during the washing process, generating significant waste. The disadvantage is that control over sphere size between different batches is complicated. More details about this synthesis procedure will be given in 2.3.

Spray drying provides another approach, atomizing a polymer solution into a heated chamber, allowing the solvent to evaporate rapidly and form loose microspheres [54]. This single-step process is straightforward and scalable, and results in low residual solvent levels, making it suitable for creating injectable microspheres. However, the method can produce particles with high polydispersity and relies on high drying temperatures, which may compromise the integrity of heat-sensitive bioactive compounds [55]. Nanoprecipitation is a versatile method particularly suited for encapsulating hydrophobic drugs [56]. It involves dissolving both the polymer and drug in a semi-polar organic solvent, such as acetone or ethanol, and then gradually introducing this solution into an aqueous stabilizer. The polymer precipitates at the interface, forming microspheres or nanoparticles. This technique excels at producing particles with a narrow size distribution and minimizes the need for large amounts of toxic solvents or external energy inputs. However, it is not ideal for hydrophilic drugs, as their solubility in the required organic phase is limited, and removing residual solvents remains challenging.

Each method is tailored to specific applications, balancing ease of synthesis, compatibility with various drugs and polymers, and control over particle size and uniformity. While solvent evaporation is a well-established and versatile technique, spray drying and nanoprecipitation offer alternatives better suited to specific requirements, such as scalability or precision in particle size.

The loading of polymer microspheres can be approached using two primary strategies: incorporating the drug during microspheres synthesis or soaking it into the microspheres after their production. The encapsulation efficiency is influenced by several factors, with drug solubility and the viscosity of the polymer solution being the most significant [57, 58]. High polymer solution viscosity affects both the size of the microspheres and the rate of drug diffusion from them. Factors such as the temperature at which microspheres are formed and the solvent evaporation rate can enhance encapsulation efficiency by promoting the rapid formation of a hard surface layer, thereby minimizing drug loss to the aqueous stabilizer phase. For highly soluble drugs in water, synthesis conditions must be carefully optimized to prevent drug loss during the synthesis and washing steps. The microsphere size (surface-to-volume ratio), polymer molecular weight, porosity, and duration of the soaking process also affect the loading efficiency. A limitation of the soaking method is that the drug tends to localize primarily in the outer shell of the microspheres, resulting in relatively fast drug release. In all drug-loaded microspheres, additional factors influence drug release kinetics, including the intended application and the injection site (sub-dermal or intravascular), which can dictate the optimal microsphere size. Additionally, the stability and solubility of the drug must be considered, as *in vitro* experiments are typically conducted in large liquid volumes under sterile conditions without the presence of cells, proteins, or enzymes that could affect stability and degradation.

Several design parameters play a crucial role in achieving the desired drug release profile. One such parameter is the molecular weight of the polymer chains used. Studies have shown that molecular weight significantly affects the rate and pattern of drug release [59, 60]. For instance, using PLGA with a higher molecular weight results in a slower drug release, whereas a lower molecular weight PLGA leads to a faster release primarily driven by diffusion. With higher molecular weight PLGA, the drug release depends not only on diffusion rates but also on the degradation rate of the polymer chains, resulting in a more complex release profile that varies depending on the experimental conditions. Another important factor influencing drug release kinetics is the size of the microspheres used [61]. Smaller microspheres have a higher surface-to-volume ratio, which generally leads to a faster initial release due to the increased surface area. However, for microspheres larger than approximately 30 μm, the release profile changes, as the release is no longer solely diffusion-driven. In larger spheres, the diffusion paths are longer, slowing the drug's movement to the surface [62]. Additionally, the degradation of polymer chains within the microsphere can lead to increased diffusion rates, thereby accelerating drug release over time.

In Chapter 2 the use of poly(lactic acid) in microspheres for radioembolization will be explored in depth.

CHAPTER
TWO

POLY(LACTIC ACID) : CHARACTERISTICS AND INNOVATION IN MEDICINE

Poly(lactic acid) (PLA) is widely regarded as one of the most well-known and commercially successful biopolymer thanks to its excellent processability and mechanical properties. The term ”biopolymer” refers to a broad range of polymeric materials either sourced directly from biological origins, such as microorganisms, plants, or trees, or synthesized chemically from biological sources like vegetable oils, sugars, fats, resins, proteins, and amino acids [63]. What sets biopolymers apart from fossil-fuel-derived polymers is their sustainability, mainly when they are biodegradable. Bio-based plastics, such as PLA, are developed as environmentally friendly alternatives to petroleum-based plastics, with the added benefit that the raw materials used in their production capture CO_2 from the atmosphere, contributing to lower carbon emissions. Additionally, PLA's degradation products are non-toxic to humans and the environment [64]. The increasing cost of petroleum feedstocks, along with growing consumer demand for ”green” or renewable products, have further accelerated the adoption of biopolymers. PLA is also energy-efficient, requiring 25-55% less energy to produce than petroleum-based polymers [65]. Its ease of production is attributed to the availability and affordability of lactic acid, making it the first bio-based polyester to be mass-produced on a commercial scale.

PLA-based polymers are widely employed in the biomedical field due to their advantageous properties, including biocompatibility (their degradation products are non-toxic and easily metabolized by the body), hydrolytic degradation *in situ*, tailorable properties, and well-established processing methods. The innate characteristics of PLA lend themselves to rapid prototyping and efficient manufacturing in 3D-printed constructs. These characteristics have enabled the development of various applications, such as bone fixation screws, bioresorbable suture threads, and stent coating, to name a few. PLA-based materials have also gained attention in nanomedicine, particularly for the synthesis of nanocarriers designed for the targeted delivery of hydrophobic drugs and radiotherapy, representing a promising new application [56, 65].

This chapter explores the properties and characteristics that make poly(lactic acid) so versatile and widely used in multiple application fields, with a particular focus on its use in radiotherapy. It will also discuss degradation and how it is affected by the material's characteristics and environmental conditions.

2.1 Synthesis processes of PLA

PLA belongs to the poly-α-hydroxy acid family, a group of linear aliphatic thermoplastic polyesters, whose constitutional monomer is lactic acid (LA; 2-hydroxypropanoic acid) (CH_3-CHOH-COOH), an optically active molecule that exists in two chiral forms: L-lactic acid and D-lactic acid. These stereoisomers allow for variations in the types of PLA, as it is a chiral polymer featuring asymmetric carbon atoms arranged in a helical conformation, influencing its properties and applications [66].

The enantiomeric forms of PLA are classified into three types: levorotatory (L-), dextrorotatory (D-), and meso (a mixture of L- and D- isomers). The type of PLA synthesized depends on the source material used: poly(L-lactic acid) (PLLA) from L-lactide, poly(D-lactic acid) (PDLA) from D-lactide, poly(D,L-lactic acid) (PDLLA)

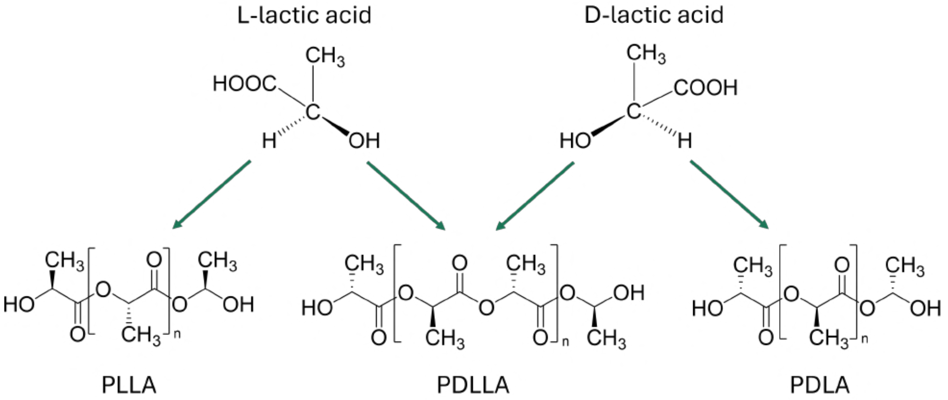

Figure 2.1: Chemical structure of PLA stereoisomers.

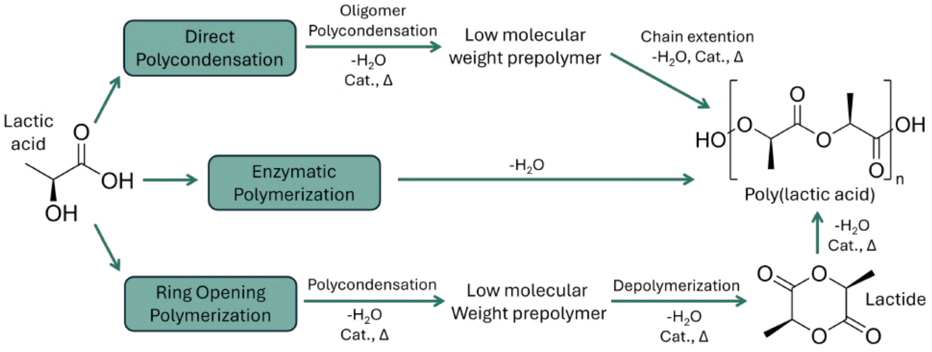

Figure 2.2: Possible synthesis methods for PLA: direct polycondensation, enzymatic polymerization, and ring-opening polymerization (adapted from [67]).

from the mesolactide (Figure 2.1).

Starting from LA, PLA can be manufactured by two main polymerization routes, which are direct polycondensation (DPC) and ring-opening polymerization (ROP), as shown in Figure 2.2. Each method has advantages and challenges, influencing the molecular weight, purity, and overall properties of the PLA produced [67].

In direct polycondensation (DPC), the lactic acid monomers are polymerized directly through a condensation reaction, where water molecules are removed as a byproduct. In this process, lactic acid molecules undergo dehydration condensation for 96 hours at temperatures of 150-250°C, forming ester bonds between the monomers and creating low-molecular-weight oligomers. Further polymerization through the chain extension step results in the formation of higher molecular weight PLA chains, although the presence of residual water can shift the reaction equilibrium and limit chain growth. While the formation of byproducts is unavoidable, it can be limited by employing a variety of catalysts, such as Sn(II) octanoate, and by altering the influencing parameters during the polymerization process to enhance the reaction rate and achieve higher molecular weight [68, 69]. However, PLA produced through DPC generally has poor mechanical properties and, therefore, is not suitable for many applications. The need for cost-effective methods to produce high-molecular-weight lactic acid-based polymers has generated significant commercial interest. Solvent-assisted polycondensation is one potential solution, as is melt polycondensation followed by solid-state polycondensation [70].

Most commercial processes for producing PLA favor the ring-opening polymerization (ROP) of lactide—the cyclic dimer of lactic acid—over polycondensation, as it is more efficient. Initially, lactic acid undergoes oligomerization to form short chains, which are then depolymerized at temperatures around 150-200°C in the presence of water to yield lactide (3,6-dimethyl-1,4-dioxane-2,5- dione). During ROP, the cyclic structure of lactide opens, allowing monomers to link into long chains and obtain high molecular weight PLA [71]. Although this route effectively produces high-quality PLA, it is a two-step process requiring additional purification, which increases costs. Additionally, it generally involves metal-based catalysts, such as Sn(II) octanoate or zinc lactate, to facilitate the reaction. The ROP of lactide is preferred because it allows for precise control over polymerization, which is critical for obtaining desired PLA properties. Since a lactide molecule contains two chiral carbon atoms, it is possible to create three stereoisomers of lactides: L, D, and meso-lactide. This chirality is advantageous for the synthesis of PLA with varied stereoregularities, which influences the material's thermal, mechanical, and degradation characteristics [72].

The chemical synthesis previously discussed relies on petroleum-based compounds that could be affected by crude oil shortages and price fluctuations. Lactic acid (LA) can be synthesized chemically as a racemic (50:50) mixture of D- and L-LA, though this process is unsuitable for applications in food, beverage, and pharmaceutical industries [73]. Since D-LA could lead to metabolic issues, it is not appropriate for producing PLA, which demands optically pure L-LA (99%) and minimal D-LA (1%) content. Moreover, the polycondensation method yields oligomers with average molecular weights in tens of thousands; however, side reactions such as transesterification can also occur, leading to the formation of ring structures like lactide. These side reactions negatively impact the properties of the final polymer [74]. While producing such byproducts cannot be eliminated entirely, it can be managed by using various catalysts, functionalization agents, and adjustments to polymerization conditions. Enzymatic polymerization has emerged as a promising alternative to overcome these challenges. This method is environmentally friendly, operates under mild conditions, and offers precise control over the polymerization process.

Several studies have reported the use of genetically engineered microbes to enhance PLA production through fermentation processes [75]. For example, the yeast *Saccharomyces cerevisiae* and the *Lactobacillus* carry the lactate dehydrogenase gene. They can produce high levels of LA by converting simple sugars (derived from plant biomass like corn, sugarcane, beets, and other crops) into lactic acid. Genetically modified strains of *Escherichia coli* have also been developed to produce optically pure LA at high yield and conversion rates on specialized media, helping reduce production costs further [76, 77]. Alkalis like lime (calcium hydroxide) are added throughout the process to neutralize the LA produced by microorganisms and maintain the pH of the fermentation broth. The resulting calcium lactate can then be acidified with strong acids, such as sulfuric acid, to release LA. However, this process generates gypsum (calcium sulfate) as a byproduct, which requires disposal as solid waste and limits the method's utility. After fermentation, LA must be separated and purified from the broth to meet final product standards. The yield of LA from the broth varies based on the raw materials used and the recovery techniques employed. A typical downstream purification process includes (1) biomass removal, (2) sulfuric acid treatment, (3) gypsum removal to obtain crude LA, and (4) final purification through ion-exchange chromatography to achieve optically pure LA, which is then condensed with a catalyst to produce PLA [78].

2.2 Properties of PLA

Crystalline and amorphous structures

Depending on its stereochemical structure and thermal history, PLA can exist in an amorphous or semicrystalline state. The crystallization behavior, degree of crystallinity, and thermal properties of PLA are influenced by factors such as molecular weight, polymerization conditions, thermal history, and purity. The crystalline regions in PLA are characterized by a highly ordered arrangement of polymer chains, resulting in enhanced rigidity, thermal stability, and strength. These regions form primarily during controlled cooling or annealing processes, particularly in PLA with a high proportion of the L-lactide isomer (PLLA). In contrast, the amorphous regions are disordered and lack long-range molecular alignment, contributing to flexibility, transparency, and lower thermal resistance. The balance between these two phases is determined by factors such as the stereochemistry of the polymer (e.g., D- and L-isomer ratio), processing conditions, and the presence of nucleating agents. By tailoring the crystalline to amorphous regions ratio, PLA can be optimized for applications ranging from heat-resistant packaging to flexible films and biomedical devices.

Like many crystalline polymers, PLA exhibits polymorphism, which is the occurrence of multiple crystalline forms. Polymorphism in polymers can be classified into two categories: crystals with different chain conformations and crystals with the same chain conformation but distinct spatial arrangements. In any given condition, only one crystalline form is thermodynamically stable, while others are metastable and may eventually transform into the stable form over time.

The earliest identified crystalline form of PLA is the α-form, which was believed to be the predominant crystallization form during standard solution casting or melt processing. Early studies on PLLA identified its primary helical structure as a 10_3 helix, with two chains packed within a triclinic unit cell [79, 80]. This 10_3 conformation represents a stable and ordered arrangement, with each chain completing ten monomer units per three turns of the helix. However, recent investigations have highlighted significant deviations from this idealized structure, primarily due to intermolecular interactions within the crystalline lattice [81, 82]. Analyses of PLLA single crystals using electron diffraction revealed that the orthorhombic space group $P2_12_12_1$ provides the most plausible packing mode for the 10_3 helices. This orthorhombic structure naturally distorts the helices into chains with 2_1 helical symmetry, reflecting subtle shifts in molecular packing induced by neighboring chain interactions. Such distortions are critical for understanding PLLA's mechanical and thermal properties, as they affect both crystallinity and material strength. Further insights were obtained through infrared (IR) and Raman spectroscopy, which suggested that the α-phase of PLLA may not be uniform but instead comprises a coexistence of 10_3 and 3_1 helical conformations [83, 84]. This hypothesis arises from the observation of spectral signatures indicative of both structures, pointing to a more complex molecular arrangement than previously assumed. Deviations in symmetry were incorporated into structural analyses to further refine the crystallographic model. These refinements led to the identification of the space group $P12_11$ as a more accurate representation of PLLA's crystalline structure, as represented in Figure 2.3. This revision accounts for a slight loss of symmetry along the chain axis, consistent with experimental observations [85].

A notable characteristic of PLLA is the discontinuity observed in its crystallization kinetics within the temperature range of 100 to 120°C, regardless of molecular weight. To explain this behavior, a novel crystalline form termed α' or δ, described as a "disordered crystal", was proposed [86, 87]. This α'-form shares the same 10_3 helical conformation and similar chain packing as the α-form but features slightly larger lattice dimensions (Figure 2.4). The α'-modification is conformationally disordered and metastable below 150°C, transitioning irreversibly into the α-form upon heating. This phase transition is thought to involve the reorganization of chain conformations, particularly the side groups, resulting in a reduced unit cell size. The formation of the α'-

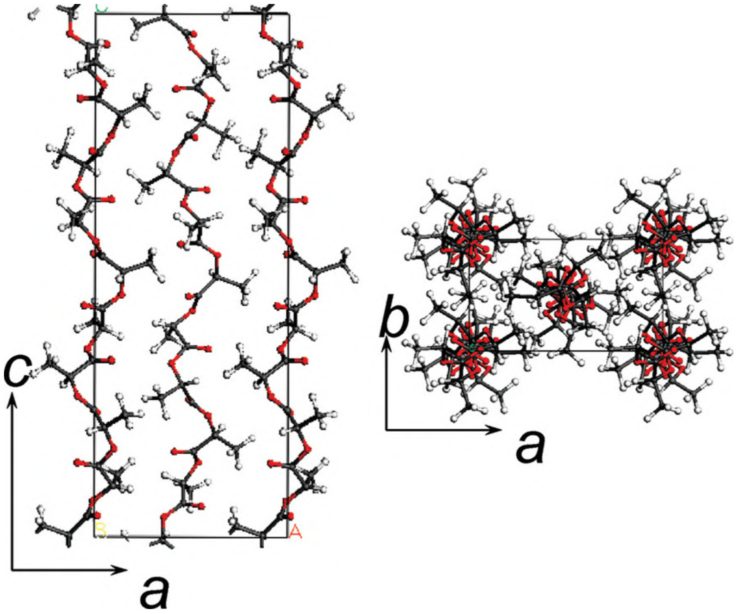

Figure 2.3: Side and top view of crystal structure of PLLA α form proposed by [85].

and α-phases is highly dependent on the crystallization temperature (T_c) [88]. At low temperatures ($T_c < 100^\circ$C), the disordered α'-phase predominates, while at higher temperatures ($T_c > 120^\circ$C), the ordered α-phase is primarily formed. Both crystalline forms can coexist and grow in the intermediate range of 100–120°C. This crystallization behavior underscores the significance of thermal history during processing, as variations in T_c can determine which crystalline structure develops.

The β crystal form can be produced at higher temperatures and stretching rates. This form exhibits improved impact resistance and heat stability, making it suitable for specific high-performance applications. The β-form has a melting temperature approximately 10°C lower than the α-form, indicating its lower thermal stability. The α-to-β crystal transition proceeded efficiently at temperatures between 130 and 140°C. It was proposed that the β-form is a frustrated structure containing three 3_1 helices randomly oriented up and down within a trigonal unit cell with a space group $P3_2$ [89]. The γ-

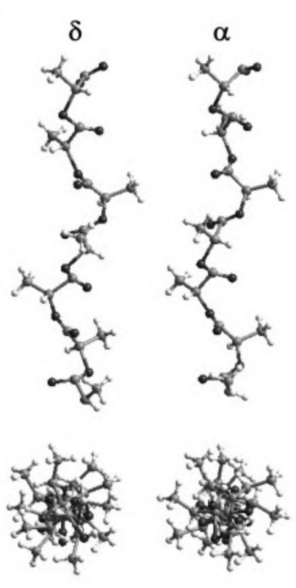

Figure 2.4: Comparison of molecular chain conformation between the crystalline forms δ (or α') and α (from [85]).

Table 2.1: Properties of different PLA crystal types from [92].

Crystal type	Crystal system	Chain conformation	Cell parameters					
			a (nm)	b (nm)	c (nm)	α (°)	β (°)	γ (°)
α	Pseudo-orthorhombic	10_3 helical	1.07	0.645	2.78	90	90	90
α'	Orthorhombic	10_3 helical	1.08	0.62	2.88	90	90	90
β	Trigonal	3_1 helical	1.052	1.052	0.88	90	90	120
γ	Orthorhombic	3_1 helical	0.995	0.625	0.88	90	90	90

form, identified through epitaxial crystallization of PLA on hexamethylbenzene, consists of two 3_1 helices packed antiparallel in an orthorhombic unit cell, distinct from the parallel helix arrangement of the β-phase [90, 91]. Table 2.1 summarizes the parameters for the reported PLLA forms.

In semicrystalline PLLA, crystalline and amorphous phases coexist, with tie molecules linking the two. As polymer crystallization progresses, the volume of the amorphous region decreases, and the decoupling between the crystalline and amorphous phases is typically incomplete, resulting in reduced mobility of the amorphous chains. This observation implies that most semicrystalline polymers should be described using a three-phase model, as illustrated in Figure 2.5: the crystalline phase, the mobile amorphous phase (MAP), and the rigid amorphous fraction (RAF) [93, 94]. The MAP represents the disordered regions of the polymer where molecular chains have significant mobility, contributing to the polymer's flexibility and the glass transition process. In contrast, the RAF arises due to the strong hindrance of amorphous segment mobility caused by the fixation of polymer chains to the crystalline lamellae. It can be characterized using thermal analysis, as it does not participate in the glass transition of the MAP and exhibits distinct thermal behaviour. It has been suggested that the crystalline phase and RAF do not significantly influence the fragility of PLLA, maintaining the polymer's nature. From extensive research on determining the exact positioning of the RAF and MAP within the semicrystalline structure, it was concluded that in the conventional homogeneous stack model, the MAP is located within the amorphous regions between crystalline lamellae or stacks. At the same time, the RAF forms interfacial layers between the crystalline lamellae and the MAP [95, 96]. The introduction of the RAF in the model offers a comprehensive understanding of semicrystalline polymer structures and their relationship with macroscopic properties, as it influences thermal and mechanical behavior by bridging the crystalline and amorphous regions, providing a gradient of mobility between the two phases.

The MA weight fraction (w_{MA}) from the specific heat capacity increment at T$_g$:

$$w_{MA} = \frac{\Delta c_p}{\Delta c_{p,a}} \tag{2.1}$$

Δc$_p$ the specific heat capacity increment at T$_g$, and Δc$_{p,a}$ the specific heat capacity increment at T$_g$ of the fully amorphous material. The RA weight fraction (w_{RA}) by difference:

$$w_{RA} = 1 - -w_c - -w_{MA} \tag{2.2}$$

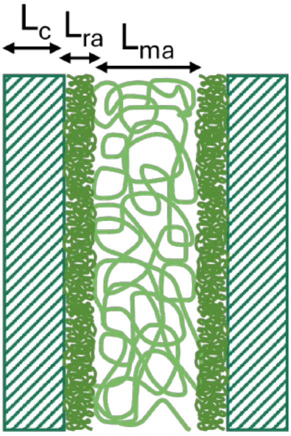

Figure 2.5: Scheme of the lamellar morphology of PLLA using the three-phase model: the crystalline layer (L_c), the rigid amorphous fraction (RAF) (L_{ra}), and the mobile amorphous phase (L_{ma}) [97].

Sometimes, the crystalline weight fraction (w_c) is determined by employing XRD measurements instead of through the previous equation. The calculation of the RA weight fraction is generally obtained from the calorimetric measurement of (w_{WA}) at T_g , which for semicrystalline PLLA is in the range of 60–70°C.

Thermal properties

Crystal polymorphism significantly impacts the thermal properties of semicrystalline polymers. The variation in melting behavior influenced by the thermal stability of various crystal modifications and the potential interconversion between these forms, as reported for PLLA, is the most commonly studied phenomena [98]. The degree of disorder in the crystal packing of PLLA influences the thermal behavior of both the crystalline regions and the coupled amorphous segments.

Pure PLLA and PDLA exhibit similar properties, including a glass transition temperature (T_g) ranging from 50 to 70°C, a melting temperature (T_m) between 170 and

190°C, and a crystallinity of approximately 35% [99]. The degree of crystallinity (X) is calculated from DSC data using the following equation:

$$X\% = 100(\Delta H_m - \Delta H_c)/\Delta H_m^0 \tag{2.3}$$

Here, ΔH_m and ΔH_c represent the melting and crystallization enthalpies, respectively, while ΔH_m^0 is the reference enthalpy for PLLA crystals of infinite size (93.6 J/g) [100].

Isotactic PLLA, composed entirely of L-lactide, is a semicrystalline polymer with the highest melting temperature among PLA variants. In contrast, syndiotactic polylactide containing higher proportions of the D-isomer, due to its different stereotactic configuration, demonstrates a lower T_g of 34°C and a T_m of 155°C [101]. The material transitions to an amorphous state as the D-isomer content exceeds 12–15%. The blending of PLLA and PDLA leads to the formation of a stereocomplex with a unique crystalline structure, distinct from those of the individual homopolymers, and a T_m reaching 230°C [102]. The peculiar characteristic of PLA is that it can crystallize not only from the melt state but also from the glassy state, so-called melt and cold crystallization. When PLA is rapidly quenched from the melt phase to a temperature below T_g, the resulting polymer becomes highly amorphous. It leads to an exothermic cold crystallization peak (T_{cc}) during subsequent reheating, typically around 100–120°C. In contrast, slow cooling results in a polymer with higher crystallinity and reduced crystallization enthalpy during reheating [92, 103].

The glass transition temperature plays a crucial role in determining the crystallization window of PLA, as the mobility of polymer chains is related to the temperature difference ($T - T_g$). Above T_g , PLA becomes soft and loses its structural rigidity, limiting its use in high-temperature applications. In contrast, below T_g , PLA retains its rigidity and strength, making it suitable for packaging and disposable products. The behavior of T_g is affected by multiple factors, including physical aging, crystallinity, morphology, and impurities. For instance, the calorimetrically determined T_g of PLLA generally decreased as crystallization temperature (T_c) increased, regardless of whether the samples were cold- or melt-crystallized. On the other hand, during the early stages of crystallization, an increase in the glass transition temperature is found, attributed to molecular motions in the interlamellar amorphous phase. These findings support the applicability of the three-phase model in explaining the structural and thermal behavior of semicrystalline PLLA [104, 105].

The glass transition of the rigid amorphous phase (RAF) was identified through changes in apparent heat capacity occurring between the mobile amorphous phase (MAP) glass transition temperature (T_g) and the melting temperature (T_m). Since the heat capacity change of the MAP at T_g depends on the enthalpy of fusion in semicrystalline PLA, which varies with thermal history, the RAF was analyzed to assess the non-linear changes in heat capacity. The thickness of the RAF – calculated using the already presented three-phase model – could affect the glass transition. Specifically, an increase in the thickness, which correlates with higher crystallization temperatures, led to a decrease in T_g [97]. It was also proposed that the RAF may not remain rigid up to the melting temperature (T_m) and could gradually decrease or disappear above the glass transition temperature (T_g) of the MAP [106].

Optical properties

Studying the optical properties of materials, including polymers like PLA, is crucial for understanding their behavior, functionality, and potential applications. Optical properties reveal valuable information about the interaction between materials and electromagnetic radiation, particularly in the visible, infrared (IR), and ultraviolet (UV) regions. Optical properties such as absorption, reflectance, and transmittance provide insight into the chemical structure, bonding, and molecular interactions within the material, while techniques like IR and Raman spectroscopy can distinguish between crystalline and amorphous regions, shedding light on the material's microstructure and its impact on physical properties.

Several factors, including constitution, configuration, conformation, stereoregularity, and crystallinity, influence the degree of order in a macromolecular system. Vibrational spectroscopy techniques, such as infrared (IR) and Raman, provide insights into these aspects by analyzing spectral bands associated with stereoregularity, chain conformations, and crystalline structures. Conformational regularity arises from intramolecular interactions between neighboring chemical groups within the same polymer chain, while crystallinity depends on intermolecular forces between adjacent chains [107].

Vibrational spectroscopy is particularly sensitive to local molecular environments, enabling differentiation between these two types of interactions. The high sensitivity of IR spectroscopy to changes in the dipole moment of vibrating groups makes it ideal for detecting polar functional groups and even structural changes during melting and crystallization [108]. For example, time-resolved IR spectral analysis was employed to study the intermolecular interactions involving both the CH_3 and C=O groups, as well as the C-O-C backbone, during both the induction and growth phases of melt crystallization. These observations highlight the significant role of weak interchain interactions in governing the nucleation and growth mechanisms of polymer crystallization. In contrast, Raman spectroscopy is better suited for analyzing the homonuclear polymer backbone due to its sensitivity to changes in polarizability.

In the PLA α-form, the 10_3 helical chains consist of $N = 90$ atoms within the translational repeat unit. The factor group of the line group is isomorphic to the cyclic group C_{10}, which includes ten symmetry elements: the identity element (E) and nine screw axes (C_{10}^k). Based on group theory, the nine atoms in the chemical unit contribute to 270 normal vibrations ($3N$). Among these, four are non-genuine modes arising from pure translations of the chain and rotations about the chain axis:

$$\Gamma_{vib} = 25A + 27B + 26E_1 + 27(E_2 + E_3 + E_4) \tag{2.4}$$

$$\Gamma_{rot-trans} = 2A + E_1 \tag{2.5}$$

In vibrational modes with A symmetry, all physical repeating units vibrate in phase, as dictated by the screw operation. For B symmetry modes, alternating units vibrate out of phase. The E_n species represent doubly degenerate modes, with pairs of vibrations occurring at the same frequency. Selection rules dictate that E_3 and E_4 modes are inactive in both IR and Raman spectroscopy. However, A, B, E_1, and E_2 modes are Raman active, while only A and E_1 modes are IR active [109].

(a) *C=O stretching region at 1850–1650 cm*$^{-1}$. In semicrystalline PLA, the C=O stretching mode exhibits four active modes in the Raman region, labeled A, B, E_1, and E_2, which appear approximately at 1749, 1763, 1769, and 1773 cm^{-1}, respectively (Figure 2.6a). In the IR spectrum, the A and E_1 active modes are overlapped, producing a broad asymmetric band around 1760 cm^{-1}. In amorphous PLA, the Raman lines are broad and asymmetric, with deconvolution analysis revealing two components at 1768 and 1749 cm^{-1}, likely due to pair addition mechanisms. The spectral splitting of the νC=O band arises from the intramolecular coupling or correlation field splitting, which is caused by interchain interactions such as C–H···O hydrogen bonding or dipole-dipole interactions [87, 108]. Since intramolecular coupling is sensitive to morphological and conformational changes, perturbations incorporating (D,D) or (D,L) units can lead to the emergence or disappearance of specific bands. In semicrystalline PLLA, the four components of the C=O stretching band correspond to the four possible conformers: *gt*, *gg*, *tt*, and *tg*. In contrast, amorphous PLLA only exhibits bands associated with the *gt*, *gg*, and *tt* conformers. The correlation field splitting, also known as factor group splitting or Davydov splitting, occurs due to lateral interactions between chains in the unit cell, dividing the absorption into multiple components. Specifically, in the orthorhombic unit cell of PLLA, the transition moments of adjacent PLLA chains can couple either in or out of phase, leading to splitting in the IR absorption spectrum [110].

(b) *CH_3 and CH bending region at 1500–1250 cm*$^{-1}$. The CH_3 asymmetric deformation modes are observed around 1456 cm^{-1} as prominent Raman and IR bands, reflecting the structural organization of the CH_3 group. Time-resolved correlation analysis suggests that CH_3 groups establish close interchain contacts during the induction period, which distorts the 10_3 helix conformation in PLLA α-crystals. Deconvolution of the Raman spectra in this region reveals three groups of split bands at approximately 1390, 1360, and 1300 cm^{-1}, corresponding to the A, B, and E modes of the CH_3 and CH bending region, respectively (Figure 2.6b) [109]. As with the C=O stretching region, the semicrystalline PLLA is characterized by sharp, split peaks, while the amorphous state displays broad, asymmetric bands [111]. In PDLA, the bands at 1390 cm^{-1}, associated with $\delta_s CH_3$ symmetric deformation, and at 1300 cm^{-1}, associated with δCH bending, are broad, have comparable intensity, and show no significant frequency shifts.

(c) *Skeletal stretching and CH_3 rocking region at 1250-800 cm^{-1}*. The doublet observed in the IR spectrum at 1185 and 1215 cm^{-1} in semicrystalline PLA is attributed to the symmetric C-O-C stretching modes (A and E_1 types) of ester groups. The band at 1109 cm^{-1} corresponds to the C–O–C trans-conformation present in the crystalline phase of PLLA, while the 1193 cm^{-1} band reflect sensitivity to both the structural arrangement of the C–O–C backbone and the ordering of the CH_3 group in the crystalline phase. Unlike the IR spectrum, the symmetric and asymmetric C–O–C modes appear as low-intensity bands in the Raman spectrum (Figure 2.6c). Additional bands at approximately 1130 and 1045 cm^{-1} are observed in both Raman and IR spectra, corresponding to CH_3 asymmetric rocking and C–CH_3 stretching, respectively. The strong band at 873 cm^{-1}, attributed to C–COO stretching, is sensitive to the 10_3 helix conformation and is present in both spectra. In IR spectra, the bands at 955 and 860 cm^{-1} are proportional to the concentration of α-form crystals [112]. Notably, a band at 921 cm^{-1}, attributed to the coupling of C-C backbone stretching with CH_3 rocking, is characteristic of the α-phase in semicrystalline PLLA. This band also observed in materials like polypropylene and poly(α-L-alanine) [113, 114], is absent in amorphous polymers.

(d) *Low-frequencies region*. Below 800 cm^{-1}, two distinct bands are observed for PLA: one in the range of 736–760 cm^{-1} and another in the range of 650–677–711 cm^{-1}, corresponding to δC=O and γC=O, respectively (Figure 2.6d). Below 600 cm^{-1}, the Raman lines become susceptible to changes in chain morphology. In semicrystalline PLA, splittings of deformation vibrations, including bending and torsion modes, appear between 398 and 411 cm^{-1} and are attributed to the δCCO mode. Additionally, the skeletal chain deformation bands (δCOC) and the backbone torsions (τCC) are found at 230, 210, and 160 cm^{-1}.

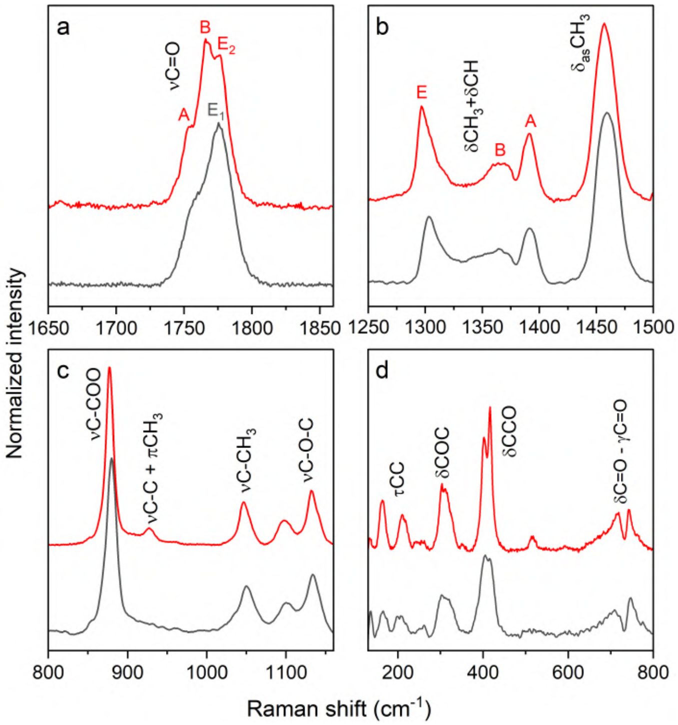

Figure 2.6: Raman spectra of semicrystalline (red curves) and amorphous (gray curves) PLA in four different spectral regions: (a) 1650–1850 cm^{-1},(b) 1250–1500 cm^{-1}, (c) 800–1160 cm^{-1}, (d) 160–800 cm^{-1}.

Degradation mechanisms

Hydrolytic degradation

As an aliphatic polyester, PLA is prone to hydrolytic degradation, unlike aromatic polyesters such as poly(ethylene terephthalate) (PET). The biodegradation process occurs naturally through the hydrolysis of ester bonds (Figure 2.7). Water molecules from the surrounding environment diffuse into the polymer matrix (stage I), although PLA's hydrophobic nature prevents polymer dissolution and results in negligible volumetric swelling. As water infiltrates, it cleaves ester bonds, constituting the polymer's backbone, leading to a chain scission mechanism (stage II). The lactic acid monomers and oligomers produced gradually diffuse out of the matrix (stage III), and their high concentration, along with the newly formed terminal carboxylic groups, accelerates the hydrolytic degradation process [56]. Moreover, water penetration into the bulk of the polymer disrupts its microstructure by creating internal cavities (stage IV). *In vivo*, enzymes further contribute to degradation by eroding the device's surface.

The behavior, rate, and mechanism of PLA's hydrolytic degradation are influenced by material factors, including molecular and higher-order structures, as well as medium factors, such as temperature, pH, and the presence of catalytic species (e.g., alkali or enzymes). These factors can be adjusted to control the degradation behavior and rate, which is particularly important for PLA-based materials used in biomedical and pharmaceutical applications [115]. Interestingly, the *in vivo* hydrolytic degradation rate of PLA is closely aligned with its *in vitro* rate [116], allowing *in vitro* studies to predict *in vivo* degradation behavior and rates to a significant extent.

The molecular weight of PLA significantly influences its hydrolytic degradation behavior, affecting both the rate and the mechanisms involved. High molecular weight PLA tends to resist hydrolysis during the initial stages of degradation due to its dense, entangled polymer chains, which impede water penetration into the matrix. Addition-

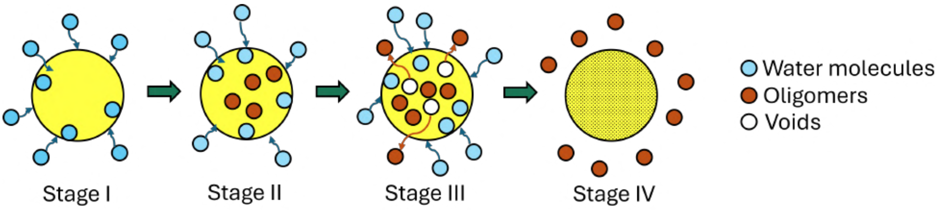

Figure 2.7: Stages of hydrolytic degradation mechanism in polymers: water diffusion (stage I), polymer hydrolysis and autocatalysis (stage II), oligomers diffusion and mass loss (stage III), and formation of a porous structure due to homogeneous degradation (stage IV).

ally, it contains fewer chain ends per unit volume, resulting in a lower concentration of catalytic sites such as terminal carboxylic and hydroxyl groups. This lower availability of reactive sites delays the onset of autocatalytic effects, where the formation of carboxylic groups lowers the local pH and accelerates degradation. However, once degradation begins, high molecular weight PLA can degrade rapidly as molecular weight decreases. In contrast, low molecular weight PLA, with its higher concentration of chain ends, is more prone to hydrolysis. The increased number of terminal groups facilitates chain scission, while shorter chains improve chain mobility, enhancing water diffusion and accelerating the degradation process [117]. This sensitivity to molecular weight enables tailoring PLA degradation rates for specific applications. For instance, high molecular weight PLA is suitable for long-term applications like medical implants, whereas low molecular weight PLA is ideal for short-term uses, such as drug delivery systems or biodegradable packaging.

The pH of the medium influences the hydrolytic degradation process. In alkaline environments, the high concentration of hydroxide ions significantly accelerates the degradation of PLA-based materials. In acidic conditions, degradation primarily follows a chain-end scission mechanism, breaking lactyl monomer units into lactic acid. Conversely, degradation occurs through a backbiting mechanism in alkaline conditions, producing lactyl dimers (lactide), which are subsequently hydrolyzed into lactoyl lactic acid [118]. This degradation is characterized by surface erosion, where the hydrolytic degradation rate at the material's surface—exposed to water with catalytic agents—far exceeds the diffusion rate of water or catalytic agents into the material. As a result, degradation appears confined to the surface. Under neutral pH conditions, referred to as neutral hydrolytic degradation (NHD), hydroxy-terminated L-lactic acid oligomers degrade via backbiting cleavage to form dimers, whereas acetylated L-lactic acid oligomers undergo random chain scission.

Temperature is another critical factor influencing the hydrolytic degradation of PLA. Elevated temperatures enhance the mobility of water molecules and their diffusion into the polymer matrix, facilitating the cleavage of ester bonds and accelerating the hydrolytic reaction. Additionally, higher temperatures promote chain scission by activating terminal carboxylic and hydroxyl groups formed during degradation, which act as catalysts for breaking down the polymer's backbone. Temperature also influences the degradation mechanism. For example, at higher temperatures, backbiting reactions become more pronounced, leading to the formation of cyclic lactide as a byproduct. When the temperature approaches or surpasses PLA's glass transition temperature (approximately 55–65°C), the polymer transitions from a rigid state to a rubbery or semi-molten state, increasing the accessibility of water to ester bonds and further accelerating hydrolysis. At temperatures near PLA's melting point (170-180°C), degradation shifts from a hydrolytic to a predominantly thermal process. When the temperature exceeds T_m , crystalline regions melt, resulting in a uniform amorphous phase. In this state, hydrolytic degradation proceeds homogeneously, resembling the behavior of non-crystallizable PDLLA [119].

The degradation kinetics are heavily influenced by PLA crystallinity. The interaction between RAF and MAP plays a role in biodegradation rates, as the RAF is less accessible to enzymatic or hydrolytic attack [99]. Chains within crystalline regions are more resistant to hydrolysis compared to those in amorphous regions due to limited water penetration into the rigid crystalline structure. Consequently, hydrolysis predominantly occurs in the amorphous regions, where water-soluble oligomers and monomers are removed, leaving behind ”crystalline residues”. Thus, hydrolytic degradation rates under alkaline or enzymatic conditions typically decrease as crystallinity increases. However, in NHD, degradation rates often increase with higher crystallinity [120]. This counter-intuitive effect arises because crystallization concentrates hydrophilic terminal groups (–OH and –COOH) and catalytic carboxylic acid groups (–COOH) within the amorphous regions. These groups loosen chain packing, facilitating water diffusion and increasing water content in the polymer. The combination of abundant water and the catalytic effect of carboxyl groups accelerates hydrolysis in crystallized PLLA.

Radiation degradation

Some polymer materials like PLA are utilized for medical applications; they must be sterilized by high energy radiations such as X-ray and γ-ray before use. The radiation resistance of these polymeric materials is also important when used in atomic furnace facilities or radiation equipment [121]. Since X-ray and γ-ray energies are so much more intense than visible light and UV radiation, they can unselectively ionize molecules through strong interactions with the molecules' nuclear or electron clouds. The secondary electrons produced by such interactions have enough kinetic energy to trigger succeeding ionizations and energy excitation of surrounding molecules.

When PLA is exposed to radiation, it can undergo physical and chemical transformations, primarily driven by molecular-level phenomena, including chain scission, cross-linking, and changes in crystallinity, which in turn influence thermal stability, structural integrity, and biodegradability (Figure 2.8). The dominant molecular mechanism observed across most studies is chain scission, wherein the polymer's molecular chains break down into smaller fragments, reducing its molecular weight. This phenomenon has been extensively documented for γ and electron-beam irradiation, with several studies identifying a linear correspondence between dose and molecular weight reduction [122, 123]. Scission of PLA's backbone ester bonds produces free radicals that may persist after irradiation, leading to post-irradiation aging effects and further degradation in oxygen-rich environments [124]. These intermediates are then inactivated through neutralization, hydrogen abstraction, or recombination with excess energy loss by chemical reactions and thermal diffusion. On the other hand, cross-linking, which involves the formation of chemical bonds between chains, can also occur but to a lesser extent, particularly at high irradiation doses (>200 Gy).

Ionizing radiation also influences PLA's crystallinity, an essential factor in determining its thermal stability and biodegradation behavior. At low-to-moderate radiation doses (e.g., 30–60 kGy), chain scission increases chain mobility, promoting reorganization into crystalline regions, as observed in both γ and electron-beam studies [125]. However, at higher doses, accumulated damage disrupts molecular packing, reducing crystallinity and impairing ordered structures [126]. The interplay between scission-induced crystallization and radiation-induced disruption is context-dependent, and the inclusion of additives or post-irradiation heat treatments can further modify crystallinity trends.

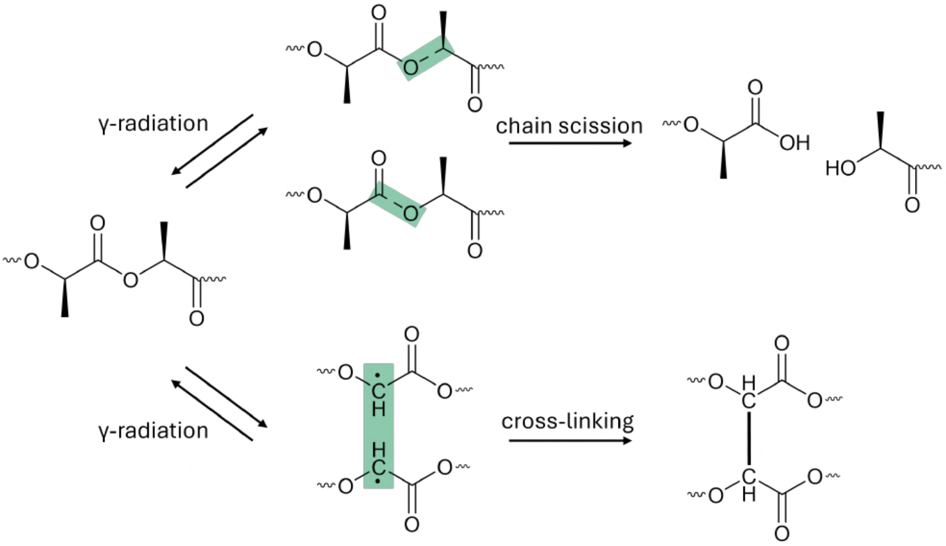

Figure 2.8: Hypothetical degradation mechanisms of PLLA upon γ-irradiation as proposed by [123].

Thermal property changes under irradiation are closely tied to molecular weight reduction and crystallinity shifts. Consistent trends across multiple studies show that T_g and T_m decrease with increasing radiation dose due to reduced chain length and amorphization [127]. Crystallinity increases observed at moderate doses may enhance the localized thermal stability of some regions but are typically outweighed by thermal degradation at ultra-high doses (>100 kGy) [128]. Practical studies on medical sterilization have established that sterilization-relevant doses (25–50 kGy) induce tolerable thermal property changes and maintain material integrity for many applications.

Aspects of X-ray-induced molecular modifications in PLA will be discussed in depth in Chapter 3.

2.3 Applications of PLA in medicine

Materials intended for internal use within the body must receive approval from regulatory agencies. The basic requirements for biomaterials in medical applications include nontoxicity, effectiveness, and the ability to be sterilized. While many existing biomaterials meet these criteria, most still lack proper biocompatibility. This term refers to a material's capacity to function as intended without adverse effects in a specific application. It depends on the material's inherent properties and interaction with the intended biological environment. Various materials have been explored for medical devices, including polymers, metals, ceramics, and composites [65].

Medical devices are typically divided into two categories: biodegradable and non-biodegradable. Currently, no non-biodegradable material can completely avoid provoking a significant foreign body response when implanted. The body's natural defenses often lead to immune rejection or encapsulation of permanent implants, resulting in complications such as bacterial infections and implant failure. As a result, biodegradable polymers have attracted considerable interest since they eliminate the need for long-term biocompatibility. These materials degrade and disappear after fulfilling their purpose, removing the need for secondary surgeries to extract the implant once the defect has healed. Despite their benefits, biodegradable polymers are not yet extensively used in clinical practice due to two major challenges. First, their degradation rate must precisely match the rate of tissue regeneration. Second, the degradation process can release byproducts that may be toxic to the body [129, 130]. Toxicity often stems from low molecular weight compounds leaching the material, such as unpolymerized monomers, additives, or residues from polymerization initiators and catalysts. While such compounds are regulated, the continuous release of degradation byproducts demands a thorough evaluation of their safety and metabolic pathways. For hydrolyzable polymers, manufacturing and storage require careful control to prevent premature degradation caused by moisture exposure. Sterilization poses a significant challenge, as certain polymers, like poly(α-hydroxy acids), are sensitive to radiation. As a result, ethylene oxide gas is commonly used for sterilization, although this method requires meticulous degassing to ensure no residual gas remains [131].

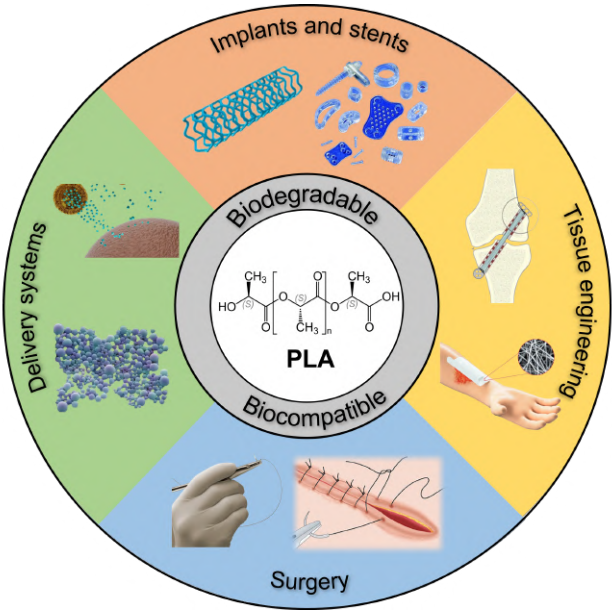

Figure 2.9: Examples of medical applications of PLA: drug delivery systems, surgical sutures, tissue engineering scaffolds, and bioresorbable implants and stents.

PLA has become a cornerstone material in a wide range of biomedical applications, as illustrated in Figure 2.9, due to its versatile properties, including tunable degradation rates, ease of processing, and capacity for bioresorption. Its significance spans orthopedics, tissue engineering, drug delivery, and surgical interventions, where its unique characteristics offer tailored solutions for specific medical challenges.

(a) **Orthopedic Applications**. In orthopedics, PLA is extensively utilized to fabricate bioresorbable screws, plates, pins, and anchors for fracture fixation and ligament repair. These devices provide temporary mechanical support during the healing process and degrade into lactic acid, a naturally metabolized compound, eliminating the need for a secondary surgical procedure to remove the hardware [132]. PLA-based implants are particularly advantageous in cases where high mechanical stiffness or long-term strength is not required, such as knee, shoulder, wrist, and zygomatic fractures. These materials also promote stress transfer to the damaged area, fostering natural tissue regeneration.

(b) **Tissue Engineering**. PLA plays a pivotal role in tissue engineering by serving as scaffolds that provide a temporary structure for cell attachment, proliferation, and differentiation. These scaffolds gradually degrade, allowing new tissue to replace the material over time. The degradation rate of PLA can be tailored through molecular weight adjustment, crystallinity, and copolymerization, making it suitable for various tissues, including skin, cartilage, and bone [133]. Advanced PLA-based scaffolds are being developed for applications such as vasculature repair, where their bioresorption properties support the formation of new blood vessels, and cardiac patches for myocardial infarction recovery, which mimic the electrophysiological functions of native tissue.

(c) **Surgical Applications**. PLA's degradable nature makes it highly effective for surgical sutures, staples, and soft-tissue fixation devices. PLA sutures dissolve naturally after tissue healing, preventing complications associated with non-biodegradable materials. In vascular surgery, PLA is employed in bioresorbable stents (BRSs) temporary support blood vessels, particularly beneficial in pediatric cases or recurrent vascular conditions, as they degrade after fulfilling their purpose [134].

(d) **Dental and Craniofacial Uses**. In dentistry, PLA is used for guided tissue regeneration as resorbable membranes and temporary implants [135]. It is also utilized in craniofacial surgeries, aiding in augmenting bone structures or repairing defects. PLA-based pins and screws have proven effective in securing craniofacial fractures due to their biodegradability and biocompatibility.

(e) **Drug Delivery Systems**. In drug delivery, PLA is widely used to manufacture microspheres, nanoparticles, and implantable devices that enable the controlled release of therapeutic agents over specified time frames. These systems are employed for the prolonged administration of medications such as vaccines, contraceptives, local anesthetics, and anticancer drugs. Drug release from PLA-based devices occurs through mechanisms such as erosion, diffusion, and swelling, which can be finely tuned by modifying the polymer's composition and structure. This precision reduces the dosing frequency and minimizes side effects, making PLA an ideal material for advanced drug delivery technologies [136]. Besides the drugs, PLA microspheres can be prepared to incorporate histological markers like fluorescein for intra-pulmonary histopathological investigations [137].

PLA Microspheres for radioembolization

PLA microspheres are emerging as a versatile and promising platform for radioembolization, a localized cancer treatment designed to target liver tumors, including hepatocellular carcinoma and metastatic liver cancers, as already discussed in Section 1.3. This approach involves delivering radioactive microspheres directly into the tumor's blood supply through transarterial catheterization. The microspheres lodge in the tumor vasculature, delivering high-dose radiation locally and minimizing exposure to healthy tissues. The unique attributes of PLA, such as its biocompatibility, biodegradability, and capacity for property modification, make it an ideal material for crafting microspheres tailored to these needs. For example, QuiremSpheres®, a type of PLLA-based microsphere containing ^{166}Ho, received CE mark approval in 2017 for selective internal radiation therapy (SIRT), marking an important step toward the broader clinical application of PLA in this domain [138].

A key advantage of PLA microspheres in radioembolization is their biodegradability. Unlike conventional glass or resin microspheres, which remain permanently in the body, PLA microspheres naturally degrade into lactic acid, a compound metabolized by the body. This property reduces the risk of long-term complications and negates the need for secondary surgeries to remove residual materials. These polymeric microspheres can be customized to achieve precise sizes, ensuring effective embolization of tumor vasculature while minimizing unintended deposition in healthy tissues [32, 139]. PLA's degradation rate can be fine-tuned by altering its molecular structure, such as adjusting molecular weight or crystallinity, allowing it to align with the therapeutic timeframes required for effective radiation delivery. Furthermore, the material's adaptability facilitates its use for carrying radioactive isotopes and co-delivering chemotherapeutic agents or other bioactive substances, enabling combination therapy that enhances tumor destruction.

The emulsion solvent evaporation method

The production of PLA microspheres for radioembolization commonly utilizes techniques such as solvent evaporation, spray drying, and nanoprecipitation, each offering unique benefits and challenges. The oil-in-water (O/W) emulsion solvent evaporation process is the most prevalent method, as it offers significant control over particle size, distribution, and morphology.

The method, described in Figure 2.10, involves dissolving the polymer in a volatile, water-immiscible solvent – defined as the *organic phase* – and incorporating a radionuclide or its precursor. Chloroform ($CHCl_3$) and dichloromethane (CH_2Cl_2) are common organic solvents, both notable for their relatively low boiling points of 61.5°C and 39.6°C, respectively. This mixture is emulsified under constant stirring into an *aqueous phase* stabilized by surfactants like polyvinyl alcohol (PVA) to create discrete droplets. These droplets then undergo solvent diffusion into the aqueous phase, followed by evaporation at the water-air interface. As the solvent evaporates, the droplets harden into solid microspheres, which are subsequently filtered and dried [140, 141].

Droplet formation during emulsification is crucial for controlling microsphere size, which impacts encapsulation efficiency, drug release rates, and *in vivo* behavior. For instance, smaller particles have higher surface areas, enhancing drug release rates, while larger particles are beneficial for extended-release formulations. The size of microspheres can be controlled by adjusting the stirring speed, stabilizer concentration, and viscosity of the organic phase. Higher stirring speeds generate smaller droplets due to increased shear forces, while greater viscosity results in larger droplets, requiring more energy for droplet disruption. Stabilizers such as PVA enhance droplet stability, with higher concentrations yielding smaller microspheres by preventing droplet coalescence [142, 143].

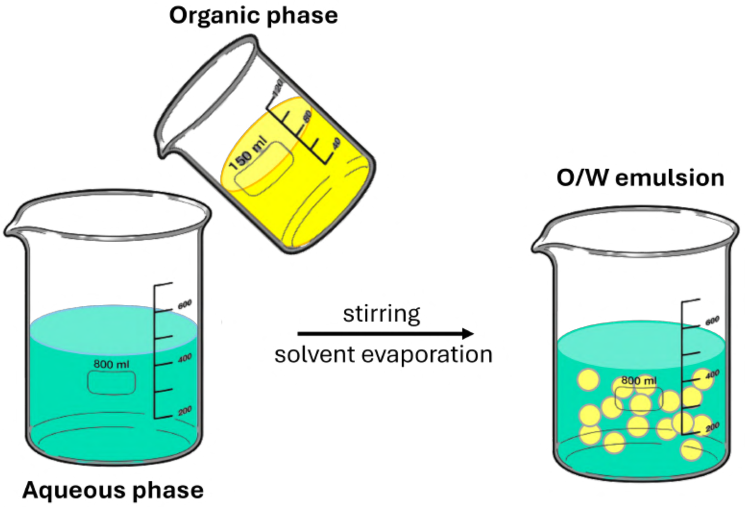

Figure 2.10: Schematic illustration of the synthesis procedure for radiolabeled PLA microspheres. The organic solution containing PLA and the radioisotope precursor dissolved in an organic solvent is added to the aqueous phase containing the surfactant. The resulting O/W emulsion, after constant stirring and the evaporation of the organic solvent, is composed of microspheres.

The organic solvent must be slightly soluble in the continuous phase to ensure effective partitioning and subsequent precipitation of the polymer matrix. Nonetheless, challenges such as removing residual solvent and achieving consistent microsphere size across batches demand careful optimization during production. Another critical consideration in microsphere production is the solubility of the compounds involved, as it determines the selection of the emulsion phases. Achieving high yield and effective encapsulation requires the compounds to exhibit low solubility in the continuous phase, ensuring minimal radionuclide loss during preparation. Temperature is another critical factor in microsphere production, influencing both solvent removal and particle solidification. Elevated temperatures accelerate solvent evaporation, promoting rapid solidification, but may lead to larger, less uniform microspheres due to insufficient mixing time. Lower temperatures, in contrast, offer better control over size distribution and result in denser particles [144]. Additionally, operating at temperatures near the boiling point of the dispersed phase solvent has been shown to improve surface porosity. In fact, increasing porosity accelerates both degradation and drug release, making this feature highly desirable for controlled-release systems [145].

The use of acetylacetonates as radioisotope precursors

Acetylacetonate (acac) complexes are versatile coordination compounds widely utilized in catalysis due to their stability and efficiency in facilitating diverse chemical transformations. They are derived from acetylacetone (Hacac, 2,4-pentanedione), and aliphatic β-diketone. At ambient conditions, it is generally accepted that Hacac mainly exists in its enolic form in the gas and liquid phases (Figure 2.11a). The pKa of Hacac in water amounts to 8.9; thus, it can be easily deprotonated, and the resulting acac$^-$ moiety can act as an anionic bidentate ligand, which can bind to metal ions in different coordination modes. Usually, metals react with Hacac to form bonds with the two oxygen atoms [146, 147].

In the synthesis of PLA, metal acetylacetonates [M^{n+}(acac)$_n$] play a pivotal role, particularly in the ring-opening polymerization (ROP) of lactide and in post-polymerization modifications. For instance, tin acetylacetonate can serve as a catalyst for ROP as an alternative to $SnOct_2$ [148], while samarium acetylacetonate has been employed in transesterification reactions to compatibilize and enhance the performance of PLA/polycarbonate (PLA/PC) blends [149, 150]. The latter also acts as a plasticizer, reducing thermal properties such as the glass transition, melting, and crystallization temperatures [151].

Due to their favorable nuclear properties, rare earth metals like samarium (Sm) and holmium (Ho) have attracted attention as radioisotopes for therapeutic and imaging applications. When coordinated with acetylacetonate ligands, these metals form highly hydrophobic and thermally stable complexes, suitable for integration into biodegradable delivery systems like PLA microspheres. These microspheres offer targeted radiation delivery while maintaining therapeutic efficacy. However, challenges persist in

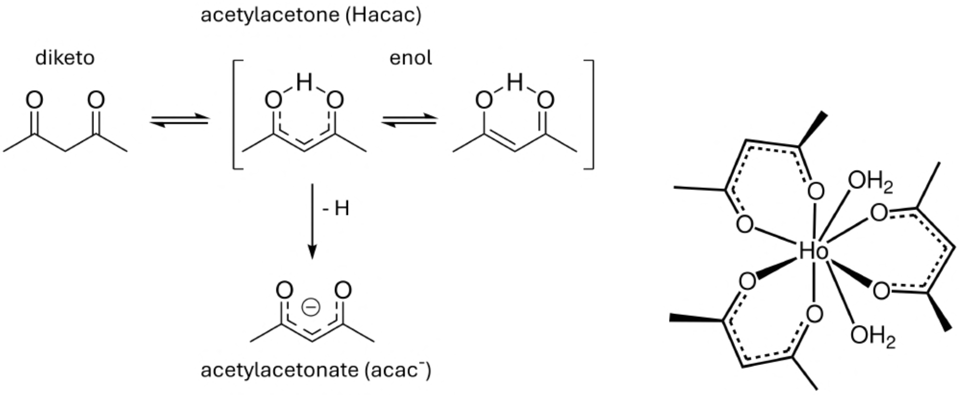

(a) (b)

Figure 2.11: (a) Tautomerism of acetylacetone (Hacac) in its diketo and enol forms, and the transformation into the acetylacetonate form (acac$^-$) through deprotonation. (b) Structure of holmium acetylacetonate (Ho(acac)$_3$), as an example for rare earth acetylacetonates.

ensuring the chemical stability of the metal-acetylacetonate complexes during encapsulation, especially in emulsion-based fabrication methods, and in preserving their compatibility with the PLA matrix during neutron activation to produce radioisotopes.

Recent research has demonstrated the successful incorporation of rare earth acetylacetonate complexes into PLA microspheres, focusing on isotopes such as Sm-153 and Ho-166 [152–154], in the form of Sm(acac)$_3$ and Ho(acac)$_3$ (whose structure is depicted in Figure 2.11b), respectively. The solvent evaporation technique has emerged as a reliable method, achieving encapsulation efficiencies exceeding 90% and significant hydrolysis resistance during processing. Post-synthesis, neutron activation converts stable isotopes (e.g., Sm-152 to Sm-153 and Ho-165 to Ho-166). Studies have shown that this process maintains the structural integrity of the microspheres and chemical stability of the complexes, with isotope retention exceeding 90% under physiological conditions [155, 156].

Advances in the characterization of rare earth acetylacetonate-PLA systems have employed techniques like infrared ion spectroscopy (IRIS) and density functional theory (DFT) modeling to analyze coordination geometries and chelation motifs, particularly for Ho(acac)3 complexes [146]. These studies have highlighted asymmetric coordination patterns and potential secondary ligand interactions while partially addressing the hydrolytic stability of the complexes during synthesis. Gaps remain in understanding ligand exchange mechanisms at emulsion interfaces.

The radioisotope content is capped at 28 wt% in polymer microspheres, significantly restricting their applications. To address this limitation, researchers have recently explored the potential of using solely the acetylacetonate complex to achieve higher radioisotope concentrations. For instance, microspheres composed exclusively of Ho(acac)3 can attain a holmium content of 45 wt% [157, 158]. Beyond Sm and Ho, emerging research explores alternative isotopes such as Yb-175 for integration into PLA-based systems. For example, microspheres loaded with ytterbium acetylacetonate have shown promising radiochemical stability and biodistribution profiles in preclinical tumor models, expanding the scope of potential applications [159]. The existing body of work demonstrates substantial progress in developing rare earth acetylacetonate-PLA microsphere systems for medical applications. Established protocols encompass synthesis, encapsulation, neutron activation, and preliminary stability assessments. However, future research must address challenges such as incorporating lesser-studied isotopes (e.g., europium and ytterbium), understanding of stability mechanisms during synthesis, and evaluating alternative biodegradable polymers as potential substitutes for PLA in these systems.

Open questions

While PLA microspheres offer significant advantages in radioembolization, several challenges must be addressed to harness their potential fully. Ensuring consistent size and shape is critical for effective embolization, as irregularities can lead to off-target effects, particularly in the intricate vasculature of tumors. Maintaining radionuclide stability throughout synthesis and degradation is critical to ensure safety and therapeutic efficacy. The degradation rate of the microspheres must also be carefully balanced to provide sustained radiation exposure without compromising patient safety [35]. Additionally, the manufacturing process often involves the use of solvents and stabilizers that must be thoroughly removed to avoid toxicity, which can increase costs and complexity. These challenges highlight the need for innovative engineering solutions to optimize the clinical performance of PLA microspheres. The application of PLA microspheres in radioembolization marks a significant advancement in targeted cancer therapies. Their degradable, localized delivery system minimizes invasiveness while allowing for customization, making them a cornerstone material in this field. With their combination of safety, efficacy, and adaptability, PLA microspheres hold the potential to transform the treatment landscape for liver cancer and other conditions.

Studies have shown that PLA microspheres can persist in the body for extended periods, sometimes exceeding 14 months, although they may lose their spherical integrity over time [160]. This slow degradation poses potential risks, such as unintended embolization in non-target organs and interference with subsequent treatments. Researchers are exploring faster-degrading formulations to mitigate these issues while ensuring therapeutic stability. Simplifying production processes and reducing costs are priorities, particularly to increase accessibility in developing regions.

Efforts to advance PLA microsphere technology are introducing new possibilities. Hybrid materials that combine PLA with other biocompatible substances are being developed to enhance their mechanical strength and imaging capabilities. For instance, PLA microspheres with embedded CT or MRI contrast agents improve procedural precision by allowing real-time visualization, reducing the risk of unintended tissue damage [161]. Additionally, their potential for co-delivering therapeutic agents alongside radiation offers a more comprehensive approach to treating advanced or resistant cancers.

2.4 Environmental impact and sustainability of PLA

Due to its bio-based and compostable nature, PLA has emerged as a widely discussed alternative to petroleum-based plastics, such as polyethylene terephthalate (PET) and high-density polyethylene (HDPE). Its production relies on fermentation processes to generate lactic acid, which is then polymerized into PLA. This renewable sourcing significantly reduces reliance on finite fossil fuels, contributing to a smaller carbon footprint during production than conventional plastics.

However, to comprehensively assess the environmental sustainability of PLA, it is necessary to evaluate its performance across its entire lifecycle: feedstock acquisition, manufacturing processes, and end-of-life disposal. Numerous studies have employed life cycle assessment (LCA) methodologies to explore the environmental impact between PLA and conventional plastics [162]. These researches revealed that PLA production significantly reduces greenhouse gas (GHG) emissions relative to PET. However, these benefits are partially offset by energy-intensive steps in PLA's manufacturing, such as the polymerization of lactic acid into PLA [163]. Additionally, the cultivation of feedstocks like corn or sugarcane requires significant land, water, and energy inputs and may compete with food production, raising ethical and practical questions about resource allocation. Additionally, the agricultural practices used for these crops often rely on fertilizers and pesticides, which can contribute to soil degradation, water contamination, and greenhouse gas emissions, an impact category in which PLA may perform worse than fossil-based PET or HDPE [164].

Processing inefficiencies in PLA production—particularly in lactide ring-opening polymerization—contribute to substantial energy demands. Optimizations such as integrating renewable catalysts or using solvent-free systems have been suggested to mitigate these inefficiencies, though such practices remain emerging in large-scale industrial contexts [163].

PLA's end-of-life disposal also presents challenges. However, it is compostable, inadequate sorting, and limited access to industrial composting facilities mean that PLA often ends up in traditional waste streams. PLA is compostable under specific industrial conditions, requiring temperatures above 58°C and controlled humidity, but such infrastructure is not always widely available [165]. Consequently, PLA often ends up in landfills, where it may generate methane under anaerobic conditions without gas capture systems. Recycling infrastructure for PLA is also sparse compared to PET, which has a well-developed bottle-to-bottle circular recycling system [166].

From a sustainability perspective, PLA represents a step toward reducing the environmental impact of plastics but is not a perfect solution. Its benefits are maximized when paired with sustainable agricultural practices, efficient manufacturing processes, and comprehensive waste management systems that include proper sorting, composting, and recycling infrastructure. Research into alternative feedstocks, such as agricultural residues or algae, is also underway to reduce competition with food production and further improve the sustainability profile of PLA [167]. The environmental benefits of incorporating recycled PLA into new products further suggest that PLA's lifecycle impacts could be considerably reduced if such advanced recycling technologies were implemented at scale. Studies also underscore the importance of aligning PLA production and disposal systems with circular economy principles to maximize its sustainability potential.

Part II

Experimental section

OVERVIEW

Poly(lactic acid) (PLA) is one of the most researched polymers due to its biodegradability, biocompatibility, and adaptability, positioning it as an ideal candidate for various biomedical and industrial applications. However, some constraints associated with structural, mechanical, and other functional characteristics need to be resolved to exploit the potential of PLA fully. These include its susceptibility to ionizing radiations, its variability in performance due to the interplay between crystalline and amorphous domains, and the need for property tailoring to suit specific requirements. This thesis systematically explores these challenges through three interconnected areas: radiation-induced modifications, crystallinity control, and novel functionalization approaches, thus providing a thorough strategy for enhancing the effectiveness of PLA in modern technologies.

In these fields, the PLA's performance depends on surmounting several challenges. For example, its chemical stability under radiation requires optimization, particularly for PLA microspheres used in radiotherapy, where activation occurs in a high-energy neutron flux. Furthermore, the degree of crystallinity in PLA influences key functional attributes such as degradation rate, mechanical strength, and interactions with therapeutic agents like drugs or radioisotopes. More emphasis is needed on how these properties may be shaped to serve specific requirements while looking at how environmental and chemical conditions impact PLA, which this thesis aims to explore.

The summaries and characterizations presented in the following chapters were conducted in collaboration with Galatea Biotech s.r.l. (University of Milano - Bicocca, Milan, Italy), who was responsible for the provision of PLLA used in the research.

Chapter 3 discusses the effects of ionizing radiation on the bulk PLA material at the molecular level, with a focus on the low-dose regime, which was not thoroughly investigated prior to that. It is well known that high doses of radiation can cause the scission of PLA chains and subsequent degradation of the polymer. However, this study reveals that low-dose radiation can alter the molecular structure, forming hydroxyl groups, C=C bonds, and hydrogen-bonded carbonyl configurations without significant chain breakage. Advanced spectroscopic methods also pinpoint key mechanisms, including Norrish type-II reactions and water-mediated processes. The chapter also explains how the radiation behavior of PLA is influenced by its initial crystalline or amorphous structure, building up the basis for optimizing PLA microspheres in the context of personalized medical treatments.

The elemental analyses have been performed by Dr. Francesco Maspero, the NMR and PXRD measurements by Sergio Piva from the group of Angiolina Comotti, University of Milano Bicocca.

Chapter 4 shifts focus to PLA microspheres, specifically addressing the control of crystallinity—a critical factor in determining their physical and functional properties. The chapter explores in more detail how the emulsification temperature during microsphere synthesis influences the ratio of crystalline and amorphous phases. Techniques such as Powder X-ray Diffraction (PXRD), Differential Scanning Calorimetry (DSC), and Raman spectroscopy are employed to analyze how temperature variations affect microsphere size, dispersity, and structural integrity. The findings emphasize the importance of precise crystallinity control for applications such as controlled drug release systems, radiation-hardened materials for additive manufacturing, and radiotherapy.

The PXRD measurements have been performed by Sergio Piva for the group of Angiolina Comotti, the DSC measurements by Giulia Tarricone from the group of Roberto Simonutti.

Incorporating a lanthanide ion in PLA microspheres to simulate the presence of a radioisotope for radioembolization is a key area of focus in Chapter 5, expanding the insights from the previous chapter. The rare-earth ion selected for incorporation into the microspheres in this thesis is europium (Eu^{3+}). This choice is based on two primary considerations: firstly, europium is more readily available compared to other rare-earth ions, such as holmium, which is commonly employed as a radioisotope in PLA microspheres. Secondly, europium is widely utilized as a luminescent probe due to its hypersensitive $^5D_0 \rightarrow ^7F_2$ transition at approximately 613 nm, which is highly sensitive to changes in its local environment. In this context, this chapter investigates in detail how europium influences the morphology, crystallinity, and stability of the microspheres while providing a detailed focus on the reasons for such changes. Thus, a temperature-controlled emulsification process integrates europium ions into the PLA matrix, resulting in enhanced crystallinity and improved thermal properties. The findings obtained using SEM, XRD, DSC, and spectroscopy techniques demonstrate that europium ions serve as nucleation sites, stabilizing the microspheres' structure. The chapter also discusses the remarkable stability of europium within the microspheres, with minimal leaching during degradation, proving that europium-doped PLA microspheres are truly promising candidates for biomedical applications like radioembolization.

The investigation presented in this chapter has been carried out over 6 months as a visiting PhD student at the Graz University of Technology (TUG), Austria, under the supervision of professor Roland Resel. Dr. Eduardo Machado Charry performed the micro-CT measurements at the Graz micro-CT Consortium. The GIXD measurements have been carried out at the SAXS beamline of the Elettra synchrotron facility (Trieste, Italy) under the supervision of Professor Heinz Amenitsch, Dr. Sumea Klokic and Dr. Philipp Aldo Wieser.

Overall, the chapters in this thesis provide a comprehensive strategy for overcoming PLA's limitations and expanding its applicability through molecular-level insights, structural optimizations, and functional enhancements. This work integrates fundamental research and practical innovation, providing a compass to understand how PLA can be especially applied in advanced medical and industrial use, expanding the frontiers of its use.

CHAPTER
THREE

RADIATION-INDUCED MODIFICATIONS IN POLY(LACTIC ACID)

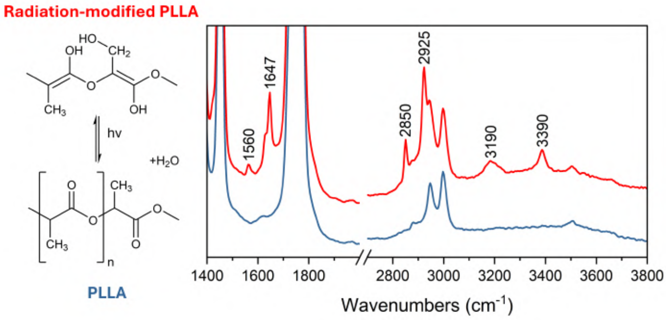

Part of this chapter has been published as:
G. Tamburini, S. Bertagnoli, G. Tarricone, S. Piva, A. Sassella, R. Lorenzi, A. Paleari,
Early stages of X-ray induced molecular unit modifications in poly(lactic acid),
Polymer Degradation and Stability **2023**, 216, 110485.

3.1 Introduction

Ionizing radiation plays a significant role in many applications involving polymeric materials. Over the past few decades, numerous studies have focused on analyzing the effects of radiation on the mechanical, chemical, and functional properties of polymers. These effects include changes in hardness, plasticity, dielectric response, color, and micromorphology, which can have substantial implications for material performance in various settings [168]. Understanding the underlying mechanisms that govern these changes, such as the polymer's crystalline or amorphous state's influence, provides valuable insights into how modifications can be promoted or inhibited. This knowledge is critical for optimizing materials and processes for specific applications, ensuring that the resulting products meet the required performance standards. This is especially relevant for polymers that have the potential to be used as biodegradable carriers of radioisotopes in internal radiotherapy, a rapidly advancing area in cancer treatment.

In the context of radioisotope delivery, inorganic glass microspheres have been widely used in clinical settings due to their excellent biocompatibility, chemical stability, and radiation hardness, which minimizes the leaching of incorporated radioisotopes [44, 46, 169, 170]. These properties make glass microspheres particularly effective in delivering high doses of radiation directly to tumors while limiting radiation exposure to surrounding healthy tissues. However, their high density relative to blood plasma and slow biodegradation – which leads to prolonged residence times in the body – pose challenges. These limitations hinder the prescription of treatment cycles and impede efficient treatment optimization via low-dose pilot microspheres in pre-therapeutic diagnostics. Biodegradable polymeric microspheres have emerged as a promising alternative to overcome these challenges, potentially providing a more versatile and sustainable solution for targeted radiation therapy and pre-therapeutic applications.

Although extensive research has been conducted on the medical applications of polymers – particularly as drug delivery carriers [52, 171, 172], theragnostic imaging nanoparticles [56], and medical device components [121] – critical issues must be resolved before their use as radioisotope microcarriers. One of the most pressing concerns is balancing biodegradability and radiation hardness. While biodegradability ensures that the microspheres are efficiently eliminated from the body after fulfilling their therapeutic role, radiation hardness is necessary to prevent premature leaching of the radioisotope before it has decayed sufficiently. This balance is essential for ensuring the microspheres are effective in delivering radiation and safe for the patient. Controlling these properties requires a comprehensive understanding of radiation damage mechanisms influenced by the polymer's initial structure, also affecting its biodegradability.

Poly(lactic acid) (PLA) emerges as a promising candidate for these applications due to its biocompatibility and high biodegradability within the human body. Early studies on PLA microspheres, particularly for internal radiotherapy, have provided preliminary data on radioisotope leaching through both *in vitro* and *in vivo* experiments, as well as clinical studies for the treatment of hepatic tumors [156, 173–175]. More recent research has continued to explore the potential of PLA for this purpose [159, 176], highlighting the promising applications of PLA microspheres as carriers for radioisotopes. These studies have provided important insights into how PLA can be utilized for targeted radiotherapy, although challenges related to radiation damage remain a key area of focus. Investigations into the effects of radiation on PLA have predominantly centered on applications where PLA tools and films are sterilized or functionalized using various forms of radiation, including using UV light, corona processes, X-rays, β, or γ radiation [177–179].

Research on radiation effects on PLA's structure and morphology primarily highlights changes in molecular weight, as already explained in Chapter 2, indicating the occurrence of cross-linking and chain scission processes as results of irradiation [124, 180, 181]. Spectroscopic analyses using Fourier-transform infrared (FTIR), attenuated total reflection (ATR) FTIR, and Raman scattering reveal that cross-linking and chain scission correlates with spectral changes, particularly in the C=O and CH_3 vibrational modes [82, 109]. These spectral alterations, induced by γ and β radiation [122, 125, 127, 128, 182–184], suggest disruptions in the carbonyl and methyl group environments due to radiation-induced conformational changes that degrade the polymer.

The underlying mechanisms of these radiation-induced modifications, including bond breaking and reactions between terminal groups, have been extensively studied.

In particular, Norrish I and II processes are often invoked to explain the chain scission and cross-linking events observed in irradiated PLA [185, 186]. These processes often involve radical formation, as indicated by electron paramagnetic resonance (EPR) studies [125, 128, 184]. Despite these advances, the initial stages of radiation-induced perturbation at the molecular level, particularly at low irradiation doses, remain poorly understood. Most research has focused on high-dose irradiation (greater than 10 kGy), with limited attention paid to the role of the crystalline or amorphous state during the early stages of radiation-induced damage. This gap in understanding presents a significant challenge for further optimizing PLA for use in radiotherapy applications.

This chapter aims to address these gaps by investigating the mechanisms occurring during the early stages of molecular perturbation in irradiated PLA, focusing on how polymer conformation influences modification events. By better understanding these mechanisms, this research tries to identify best practices for producing PLA with the appropriate radiation hardness required for effective use as a radioisotope carrier in radiotherapy applications.

3.2 Materials and methods

The present study investigates a matrix of unirradiated and irradiated PLA samples (Mw $\sim$ 84 kDa) with different initial conformational features. These were obtained by subjecting a batch of semicrystalline PLA pellets (mass 15–20 mg each) to thermal treatments. The pellets were fabricated via hot extrusion at 180°C from bio-produced L-isomer. Thermogravimetric analysis (TGA) and combustion-based organic elemental analysis confirmed the final material to be free from bioprocess residuals, such as solvents or nitrogen- and sulfur-containing contaminants, with concentrations below the instrumental detection limit of approximately 10^2 ppm. The complete degradation of the sample occurs around 350°C. Beyond this temperature, the sample demonstrates thermal stability. Traces of water, attributed to PLA hygroscopicity, were detected in a few samples via weak broad infrared absorption in the H–O–H bending region of water molecules. Surface contamination was ruled out by comparing measurements from external and freshly cut surfaces. Five distinct types of starting materials were identified among the sample sets: as-extruded (AE) and re-extruded (RE) PLA samples, and samples derived from AE that underwent specific thermal treatments: heating above the melting temperature of 220°C followed by quenching at 0°C (MQ), cold crystallization at 150°C after treatment at 220°C (CC), and remelting at 220°C after cooling at the same temperature (RM). Differential Scanning Calorimetry (DSC) experiments were used to perform the thermal treatments on samples and to determine the thermal properties. The materials' crystalline or amorphous states were assessed by powder X-ray diffraction (PXRD). Raman spectroscopy provided additional insights into the PLA conformation. Samples from each PLA material set were exposed to X-ray doses ranging from low doses (1–100 Gy) to higher doses (300–3000 Gy) to study the effects of irradiation. The low-dose range remains unexplored, while the higher-dose range overlaps with the lower limit (1 kGy) of previously investigated ranges. Given the absence of a known dose threshold for molecular perturbation, selected doses were chosen as 1×10^k Gy and 3×10^k Gy for $k = 0, 1, 2, 3$, sampling effects on a logarithmic scale. X-ray irradiation was performed using a tungsten (W) target, 20kV accelerating voltage, and 20mA current intensity. The effects of irradiation were analyzed via attenuated total reflection Fourier-transform infrared (ATR-FTIR) spectroscopy. Spectra were collected at five points on each PLA pellet and averaged across repeated measurements on different pellets, resulting in over 200 samples analyzed. Spectral intensities were normalized to the asymmetric bending mode of CH_3 at 1450 cm^{-1}, as this mode remains unaffected by irradiation [124]. Repeated measurements taken at intervals from minutes to weeks after irradiation confirmed the stability of observed spectral changes at room temperature. Isochronous and isothermal annealing experiments (1–10 min, 50–80°C) further assessed the stability of irradiation effects. Additional insights into irradiation effects were obtained via ^{1}H Nuclear Magnetic Resonance (NMR) and Gel Permeation Chromatography (GPC).

3.3 Results and discussion

Characterization of PLA initial conformation

The results of the DSC analysis provide an initial overview of the thermal history and expected conformation of the investigated PLA materials before irradiation. Representative DSC curves for the two types of starting materials are presented in Figure 3.1: PLA produced via single hot extrusion (AE sample, Figure 3.1a) and PLA produced via double hot extrusion (RE sample, Figure 3.1b). In Figure 3.1a, the absence of an exothermic crystallization peak during the first heating, which appears at approximately 100°C in Figure 3.1b, indicates that the AE material is predominantly crystalline. In contrast, the RE material begins in a primarily amorphous state. During cooling to 0°C, the AE sample does not exhibit exothermic peaks around 105°C, which are observed in the RE sample.

Both samples display a glass transition temperature (T_g) around 64°C and an endothermic melting peak at 175°C. Additionally, Figure 3.1a demonstrates that the AE material undergoes cold crystallization during a second heating cycle, following melting at 220°C for 1 min and cooling to 0°C. This is evidenced by a broad exothermic peak at approximately 115°C, signifying reduced crystallinity after heating above the melting temperature. Interestingly, during a third DSC cycle with heating above the melting temperature, as reported in Figure 3.2, the material becomes fully amorphous and exhibits an intense crystallization exothermic peak, similar to the one observed during the first cycle of Figure 3.1b. This behavior suggests that the combined thermal and mechanical conditions of re-extrusion, as applied to the parent semicrystalline AE material to produce the RE sample, are analogous to repeated melting, resulting in the amorphization of the structure.

Based on the DSC curves, AE and CC samples are expected to exhibit crystalline characteristics. RE, MQ, and RM samples derived from AE through treatments halted after melting are expected to display amorphous properties. Further confirmation of PLA conformation within the investigated material set is provided by powder X-ray diffraction (PXRD, Figure 3.3). The PXRD patterns reveal well-defined peaks in AE

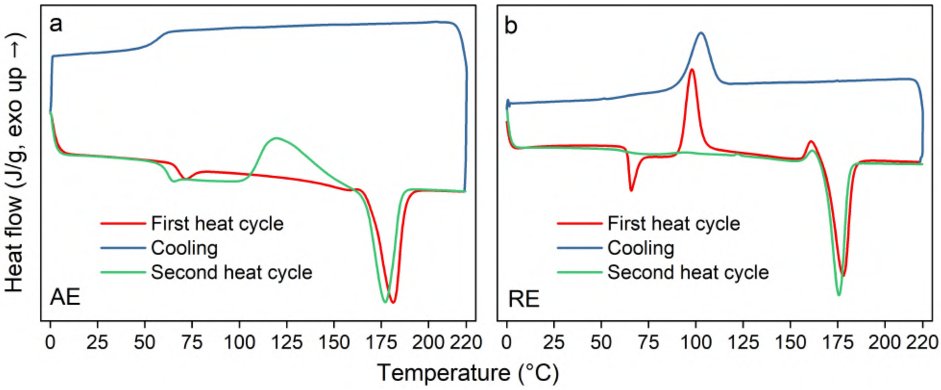

Figure 3.1: Differential Scanning Calorimetry (DSC) analysis of PLA materials. (a) PLA produced via hot extrusion at 180°C followed by slow cooling (AE sample). (b) PLA subjected to two successive hot extrusion processes at 180°C (RE sample).

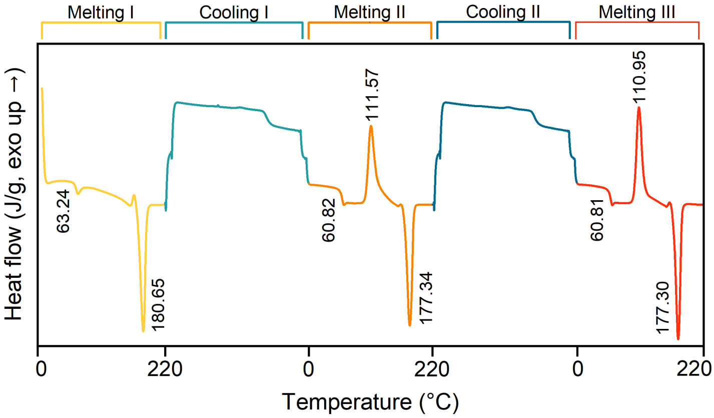

Figure 3.2: Thermal behavior of an as-extruded (AE) PLA sample during heating and cooling ramps from 0 to 220°C measured by DSC. The values of T_g , T_c , and T_m are indicated in the figure.

and CC samples, while MQ, RM, and RE samples display only a broad halo. The narrow reflections at $2\theta = 16^\circ$ and 18° are consistent with the presence of 10_3 helices of crystalline PLA in the α-form, whereas the broadband is characteristic of amorphous polymeric compounds [109, 187]. Thus, AE and CC samples exhibit crystalline features, while the other samples are amorphous, as further corroborated by Raman spectra (Figure 3.4). Indeed, the low-energy regions of the τ(CC) skeletal chain torsion and δ(COC) and δ(CCO) chain deformation modes (200–600 cm^{-1}) exhibit narrow and split peaks in AE and CC materials, consistent with their more crystalline structure. In contrast, MQ, RM, and RE samples display broad spectral features indicative of an amorphous state that disrupts chain morphology and broadens skeletal chain modes. Additional evidence of amorphous-state broadening is observed in the 700–750 cm^{-1} region of the δ(C=O) modes, and even more prominently at 920 cm^{-1}. Only AE and CC materials show a fully resolved mode at this latter frequency, attributed to the coupling of ν(C–C) backbone stretching with CH_3 rocking.

Effects of X-ray irradiation on PLA

The studied materials' ATR-FTIR spectra display all PLA's intrinsic vibrational characteristics (Figure 3.5a). The spectral region from 800 to 1500 cm^{-1} is dominated by skeletal stretching, and CH_3 rocking and bending modes. The prominent C=O stretching mode is observed near 1750 cm^{-1}, and the CH_3 stretching modes are centered around 2900 cm^{-1}[109]. Notably, no significant changes are observed in these intrinsic vibrational modes after irradiation within the investigated dose range, especially those sensitive to the crystallinity, e.g. the CH_3 rocking mode coupled with (C–COO) stretching at 870, 921 and 955 cm^{-1}, showing that the irradiation process does not alter the morphology of PLA. However, weak radiation-induced peaks are detected at 1560, 1610, 1627, 1647, 2850, 2925, 3180, and 3390 cm^{-1}, absent in the expected PLA phonon spectrum (Figure 3.5b, c). These peaks persist reproducibly for weeks after irradiation.

Figure 3.6 summarizes the statistical intensity-dose relationship for these peaks, based on hundreds of measurements across PLA samples subjected to low X-ray doses (0-100 Gy), a range previously unexplored. The data reveal clear dose-dependent spec-

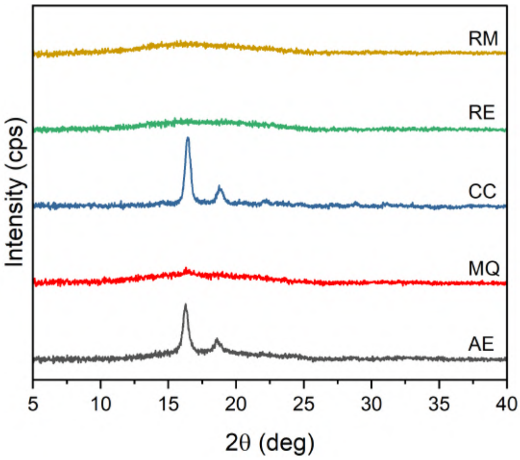

Figure 3.3: PXRD patterns in the 2θ range of 5deg–40deg for various PLA types: as-extruded (AE) at 180°C, melted at 220°C and quenched at 0°C (MQ), melted, cooled, and cold-crystallized by reheating at 150°C (CC), melted, cooled, and subsequently remelted (RM), and re-extruded (RE).

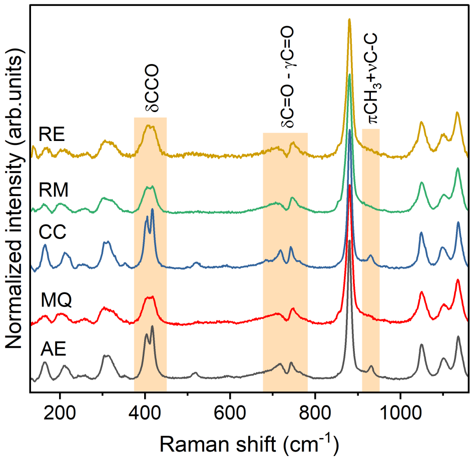

Figure 3.4: Raman spectra in the range 130-1100 cm^{-1} of different types of PLA: as-extruded (AE), extruded and remelted at 220°C, and quenched at 0°C (MQ), extruded after remelting, cooled, and subsequently cold crystallized by reheating at 150°C (CC), extruded after remelting and cooling, and subsequently remelted (RM), and re-extruded (RE). Attributions of the main spectral features are shown.

tral changes, exceeding uncertainties associated with polymeric inhomogeneity. Specifically, the peaks at 1560 cm^{-1}, 1627–1647 cm^{-1}, and 3180–3390 cm^{-1} are unequivocally radiation-induced, while the peak at 1610 cm^{-1} decreases with irradiation when present before exposure. Similarly, the peaks at 2850 and 2925 cm^{-1} are enhanced by irradiation but may also be observed in unirradiated samples. The intensity of these radiation-induced features can reach up to 1–10% of the reference intensity of the intrinsic CH_3 mode at 1450 cm^{-1}.

Further insights arise from correlations among intensities of the irradiation-dependent peaks, as shown in Figure 3.7. Strong correlations exist between specific peak pairs, such as 1627 and 1647 cm^{-1}, 2850 and 2925cm^{-1}, and 3180 and 3390 cm^{-1} (Figure 3.7a-c), while moderate correlations are observed between these pairs (Figure 3.7d-f). Conversely, the radiation-induced bleaching of the 1610 cm^{-1} peak does not correlate with the growth of peaks at 1627–1647 cm^{-1}, 2850–2925 cm^{-1}, or 3180–3390 cm^{-1} (Figure 3.7g-i). The 1560 cm^{-1} peak, which exhibits a non-monotonic dose dependence, shows no significant correlation with other spectral features, except for a moderate association with the 1627–1647 cm^{-1} peak pair (Figure 3.7j-l). These observations suggest distinct molecular mechanisms underlying the formation of these vibrational features, providing valuable insights into the radiation-induced modifications of PLA.

The peaks at approximately 2850 and 2925 cm^{-1} (Figure 3.5c) lie in the C–H stretching region[188]. Their positions differ from native CH_3 stretching modes of PLA at 2880, 2945, and 2997 cm^{-1} [109]. Their strong correlation (Figure 3.7b) suggests a common origin, consistent with the symmetric and asymmetric stretching of CH_2 groups in polyethylene [189] and photodegraded PLA [190].

The weak peaks at 3180 and 3390 cm^{-1} (Figure 3.5c) suggest the formation of hydroxyl (OH) groups upon irradiation. Although PLA's hygroscopic nature could lead to water incorporation and subsequent reaction during irradiation, the sharpness of these peaks cannot be ascribed to the broad OH stretching band of water molecules, which typically lacks narrow features [191, 192]. Instead, these narrow peaks suggest the formation of in-chain OH groups, distinct from the terminal OH of PLA chains, responsible for peaks at 3657 and 3510 cm^{-1} [185], which remain unaffected by irradiation

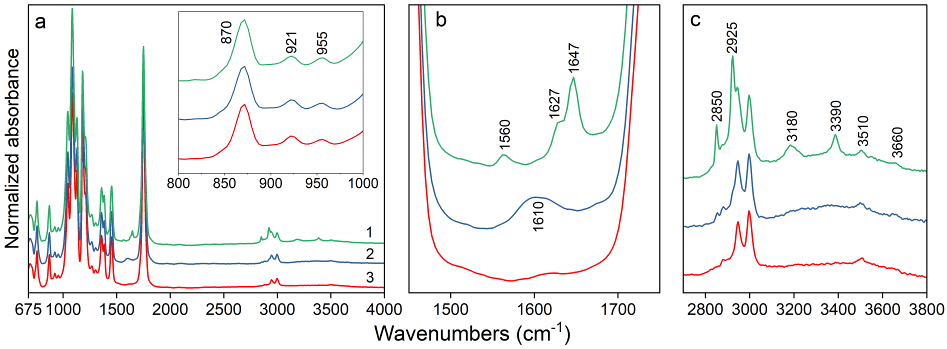

Figure 3.5: Effects of irradiation on the infrared spectra of PLA. (a) ATR-FTIR representative spectra for (1) unirradiated PLA, (2) unirradiated PLA with a native 1610 cm^{-1} band, and (3) X-ray irradiated PLA showing additional radiation-induced peaks. Inset: zoomed spectral region (800–1000 cm^{-1}) highlighting three vibrational modes associated with the CH_3 rocking mode coupled with (C–COO) stretching, sensitive to chain crystallinity. All spectra are normalized to the intensity of the 1450 cm^{-1} CH_3 bending mode. Enlarged views of (b) 1450–1750 cm^{-1} and (c) 2750–3800 cm^{-1} regions, with relevant peak positions marked.

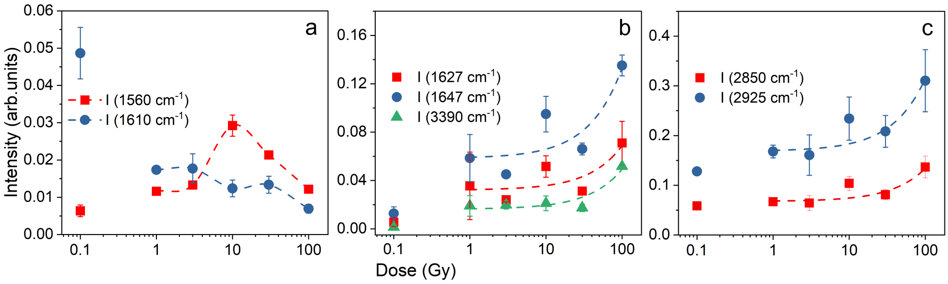

Figure 3.6: Radiation dependence of anomalous vibrational peaks. ATR-FTIR intensity vs. X-ray dose in semi-logarithmic scale for low doses (0-100Gy) of (a) peaks at 1560 and 1610 cm^{-1}, (b) peaks at 1627, 1647, and 3390 cm^{-1}, and (c) peaks at 2850 and 2925 cm^{-1}. Intensities are normalized to the CH_3 bending mode peak at 1450 cm^{-1} in the same spectrum and compared to unirradiated samples. Error bars represent standard deviations. Dashed curves in (a) are guides to the eye, while those in (b) and (c) are results of linear fitting.

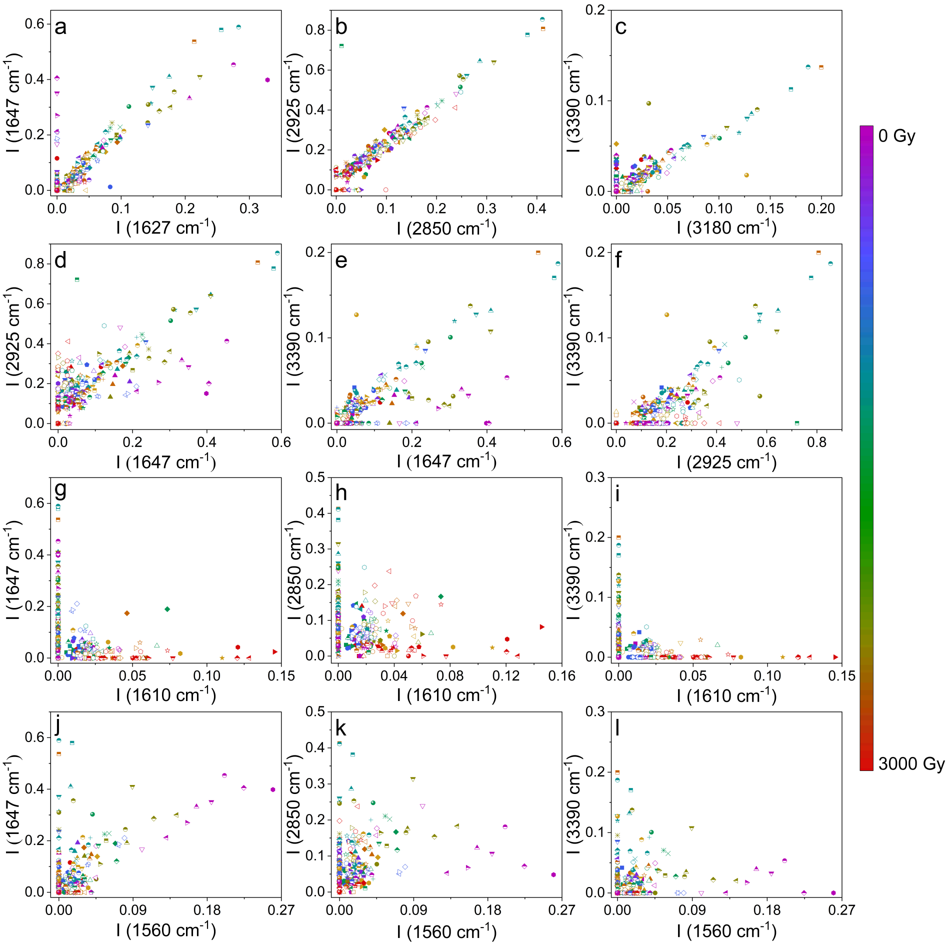

Figure 3.7: Correlation plots showing the intensity relationships of specified anomalous infrared absorption peaks in the FTIR spectra of irradiated and unirradiated PLA. Data were collected across 36 measurement sessions (represented by distinct symbols), each averaging six samples with repeated measurements per sample. Intensity values are normalized to the intrinsic CH_3 bending mode of PLA at 1450 cm^{-1}, used as an internal reference in each spectrum.

(Figure 3.5c).

The broad peak at 1610 cm^{-1} (Figure 3.5a, b) is attributed to the δ(HOH) bending modes of water molecules, as observed in various systems [193–195] and in other PLA-water interactions [196]. Alternative attributions to amide groups or aromatic C=C bonds are inconsistent with elemental analysis and spectral data [188, 197, 198].

The peaks at 1627 and 1647 cm^{-1} (Figure 3.5b) align with the C=C stretching region of non-conjugated alkenes [188, 198]. Evidence from prior studies suggests these peaks correspond to C=C bond formation in PLA [126, 185, 199–201]. The 1560 cm^{-1} peak likely arises from perturbed carbonyl configurations, potentially involving hydrogen bonding, as seen in other carbon-based systems post-oxidation [188, 201, 202]. Its appearance at low doses and disappearance at higher doses suggest it originates from transient molecular perturbations. This spectral analysis demonstrates the distinct vibrational modes induced by irradiation, providing unprecedented insights into the effects of low-dose radiation on PLA at the molecular level.

Mechanisms of radiation-induced perturbation of the molecular unit

The IR absorption data presented in the previous sections provide clear evidence of molecular perturbation in the PLA unit caused by X-ray irradiation in the investigated low-dose range. These perturbations involve the formation of chemical groups and bonds not originally present in the PLA molecular structure: (a) C=C bonds, (b) hydroxyl (OH) groups (distinct from chain-end OH groups), (c) methylene (-CH_2) groups, and (d) hydrogen-bonding carbonyl ($C{=}O\cdots H$) groups.

The observed data suggest that the initial events of radiation damage involve multiple molecular modification pathways. A Norrish type-II mechanism has been proposed to contribute to PLA photodegradation [185, 190, 203], yielding reaction products such as CH_2 and OH groups. However, this mechanism alone cannot fully account for the experimental results, including the current data set [190, 203]. Specifically, while this mechanism predicts the formation of alkene =CH_2 groups from the hydrogen transfer from the methyl to the carbonyl group (with characteristic modes in the 3000–3100 cm^{-1} range), such modes are not detected in the present spectra. Notably, the initial

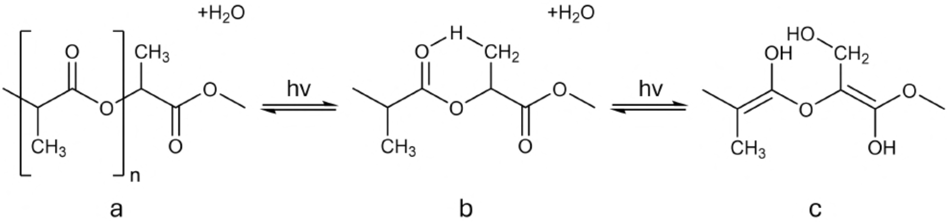

Figure 3.8: Mechanisms of modification: (a) PLA molecular unit interacting with adsorbed water. (b) Methyl-carbonyl hydrogen bonding facilitates a Norrish II-like reaction. (c) Resultant structure from the reaction with water, forming CH_2 alkene, intrachain OH, and C=C bonds.

step of the Norrish type-II mechanism involves hydrogen bonding between the carbonyl and methyl groups of the unperturbed PLA molecular unit (Figure 3.8a, b). This interaction results in a C=O stretching mode significantly lowered in frequency, appearing around 1560 cm^{-1}. The detection of this 1560 cm^{-1} peak after low-dose irradiation suggests the occurrence of the Norrish type-II reaction as an early, metastable stage of radiation-induced molecular changes in PLA (Figure 3.8b).

Subsequent molecular modifications likely involve the formation of C=C bonds via the carbonyl group's carbon atom, and the carbonyl's transformation into an intrachain C–OH group (Figure 3.8c). The alternative formation of a C=C bond with the methyl group carbon can be excluded, as it would lead to =CH_2 groups, which are not supported by the absence of alkene C–H stretching modes in the 3000–3100 cm^{-1} range [188]. Instead, the hydroxylation of the carbonyl group is corroborated by the appearance of peaks at 3180 and 3390 cm^{-1}. These peaks, attributable to OH groups within the molecular unit (distinct from chain-end OH groups), correspond to stretching modes in =COH–O structures involved in intramolecular hydrogen bonds, as observed in other systems [204, 205]. This process resembles radiation-driven keto-enol tautomerism [206], potentially facilitated by the presence of water molecules. The process is consistent with the rise of C=C modes at 1627–1647 cm^{-1} and intrachain OH stretching at 3200–3400 cm^{-1}.

Water molecules likely play a key role in these reactions, potentially substituting for the hydrogen bonding between carbonyl and methyl groups depicted in Figure 3.8b. This tautomerism differs from the Norrish type-II mechanism and accounts for the emergence of CH_2 stretching modes at 2850–2930 cm^{-1}. Specifically, the methyl group (-CH_3) is transformed into a -CH_2–OH group through water interaction, resulting in the pair of peaks at 2850 and 2925 cm^{-1} (Figure 3.8c). Importantly, this mechanism does not involve chain scission, which is consistent with the absence of any increase in end-chain OH signals. Gel Permeation Chromatography (GPC) measurements confirm no detectable changes in molecular weight (M_w) attributable to chain breaking. Additional confirmation comes from ^{1}H NMR analysis of unirradiated and irradiated samples. Following FTIR verification of sidechain OH removal via PLLA dissolution in $CHCl_3$ (Figure 3.9), the ^{1}H NMR spectra show no significant increase in OH resonance intensity at approximately 3.5 ppm after irradiation (Figure 3.10), ruling out chain breaking-induced end-chain OH formation.

Evolution at high doses and thermal stability of modified groups

The modified molecular unit shown in Figure 3.8b, featuring an intrachain hydrogen bond between methyl and carbonyl groups, exhibits instability, as evidenced by the decrease of the IR mode at 1560 cm^{-1} at doses exceeding 10 Gy (Figure 3.6a). This observation suggests that the intermediate state depicted in Figure 3.8b can either revert to the polymer's initial configuration or evolve into alternative conformational states. These pathways may include reactions with water molecules (Figure 3.8c) and subsequent interactions with other groups.

At higher irradiation doses, the metastability of radiation-induced IR modes becomes apparent. Specifically, these modes diminish to very low asymptotic values at doses beyond 100 Gy and up to 3 kGy (Figure 3.11). This trend indicates that energy dissipation from the radiation to the material facilitates the annealing of the groups formed during the early stages of PLA molecular unit modification.

Isochronous and isothermal annealing experiments on the radiation-induced IR modes further confirm the thermal instability of these groups and underscore the role of thermal energy dissipation during X-ray exposure. Figure 3.12 demonstrates that the

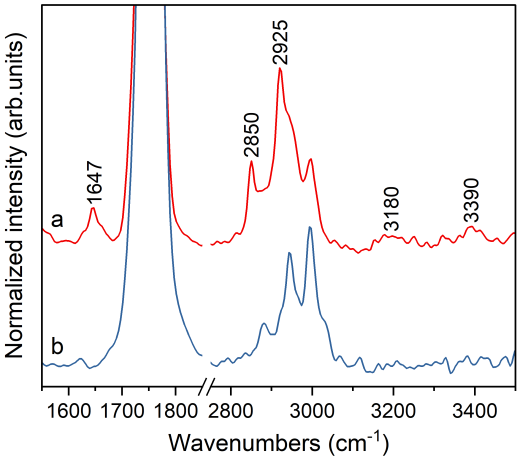

Figure 3.9: FTIR spectra of (a) irradiated bulk PLLA, and (b) the same sample after dissolution in $CHCl_3$ and subsequently dried, showing the full removal of irradiation-induced vibrational modes including sidechain and end-chain OH modes at 3180 and 3390 cm^{-1}.

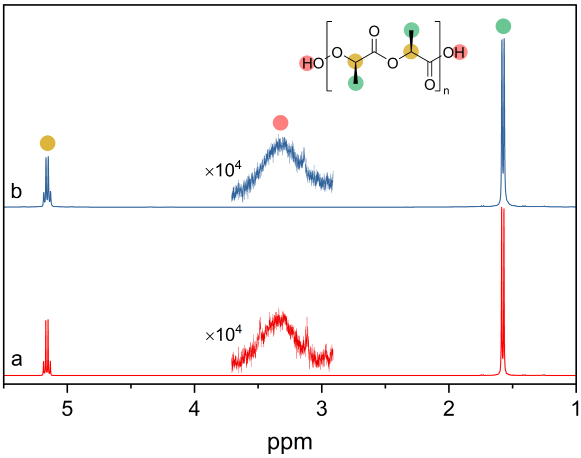

Figure 3.10: ^1H NMR spectra of (a) PLA samples unirradiated and (b) irradiated at 100 Gy dissolved in $CDCl_3$. The resonance signal at 1.4-1.6 ppm is assigned to methyl protons (-CH_3) and at 5.1–5.2 ppm to methine protons (-CH) of the PLA repeat unit. The spectral region at 3-4 ppm of OH groups is magnified, showing the lack of relevant changes ascribable to irradiation-induced end-chain OH groups. Concentration effects cause minor differences in the broadening of this resonance due to slightly different dilutions.

Table 3.1: Values of melting (T_m) and cold-crystallization (T_{cc}) temperatures from DSC curves of as-extruded (AE) PLA samples unirradiated and irradiated at 1 to 3000 Gy doses. Melting temperature values are related to the first and second heating (T_m^1 and T_m^2, respectively).

	Dose (Gy)								
	0	1	3	10	30	100	300	1000	3000
T_m^1	179.6	181.2	180.4	179.4	180.2	179.4	180.2	179.5	179.4
T_{cc}	117.1	119.9	117.9	119.7	119.2	115.2	119.0	115.6	114.1
T_m^2	176.1	177.2	177.7	176.2	177.0	175.8	176.5	176.6	175.1

peaks at 1627–1647 cm^{-1} are bleached upon thermal heating above 60°C, which is near the PLA glass transition temperature (T_g). Complete bleaching to negligible values occurs after annealing at 80°C, with similar results observed for other radiation-induced peaks. This behavior suggests that the bleaching of these radiation-induced vibrational modes arises from interchain interactions facilitated by heating above the T_g of the system.

Importantly, if the reduction in IR mode intensity at high doses results from interchain reactions, it implies a conformational change in the material. Such effects are supported by DSC measurements on irradiated samples at varying doses (Table 3.1), which reveal changes in the glass transition temperature. As shown in Figure 3.13, the T_g decreases at irradiation doses above 100 Gy. This finding supports the hypothesis of conformational readjustments in the material, particularly in the dose range where the anomalous vibrational modes from the initial modification events disappear. This rearrangement likely reflects a transition toward a less crystalline state, driven by interchain interactions mediated by reactions between radiation-induced molecular groups and localized energy release from the X-ray beam.

Role of PLA initial conformation

The comparison between samples with differing initial conformations reveals significant differences in the effects of irradiation, as illustrated in Figure 3.14 for the 1647

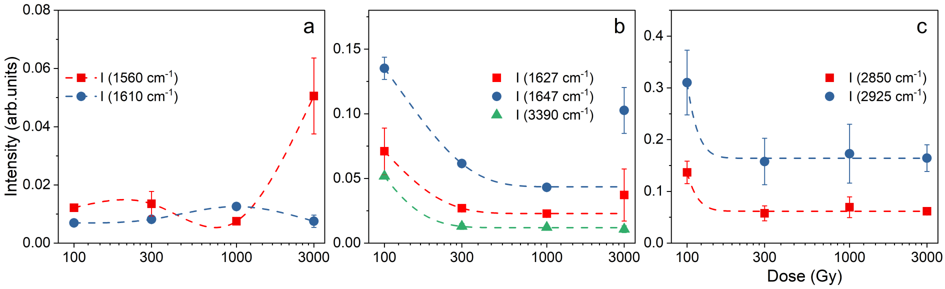

Figure 3.11: ATR-FTIR intensity vs. X-ray dose in semi-logarithmic scale for doses higher than 100 Gy of (a) peaks at 1560 and 1610 cm^{-1}, (b) peaks at 1627, 1647, and 3390 cm^{-1}, and (c) peaks at 2850 and 2925 cm^{-1}. Intensities are normalized to the CH_3 bending mode peak at 1450 cm^{-1} in the same spectrum and compared to unirradiated samples. Error bars represent standard deviations. Dashed curves are guides to the eye.

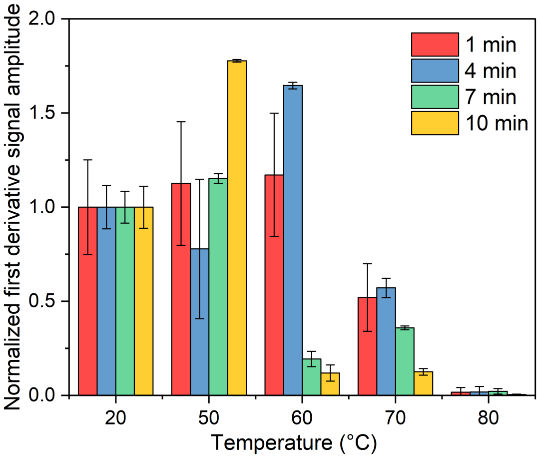

Figure 3.12: Thermal stability of anomalous peaks: First derivative ATR-FTIR intensity at 1647 cm^{-1} plotted against annealing temperature for various annealing times, normalized to the initial intensity (unity at 20°C). Error bars represent estimates based on the signal-to-noise ratio of the IR spectra.

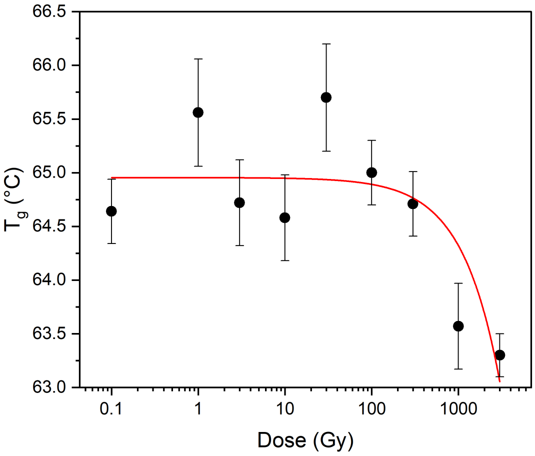

Figure 3.13: Dose dependence of the glass transition temperature: Glass transition temperature (T_g) plotted against X-ray dose on a semi-logarithmic scale, derived from DSC curves of irradiated PLA samples. The curve serves as a guide to the eye. Error bars reflect propagated uncertainties from the standard DSC curve analysis used to determine T_g.

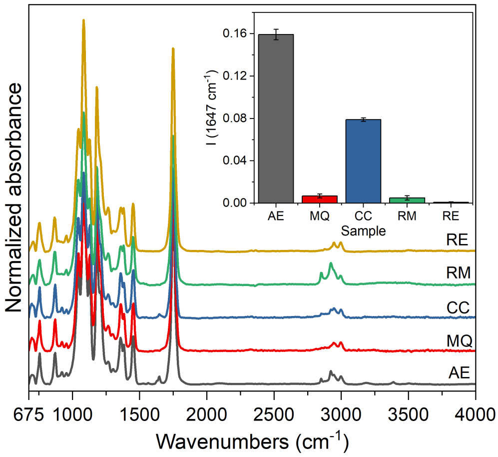

Figure 3.14: Conformation dependence: Representative ATR-FTIR spectra of various PLA samples (labels as in Figure 3.3) after 100 Gy X-ray exposure. Intensities are normalized to the intrinsic CH_3 bending mode at 1450 cm^{-1}. Inset: Intensity of the X-ray-induced 1647 cm^{-1} mode across the different samples.

cm^{-1} mode after 100Gy irradiation. Materials with more crystalline structures, such as AE and CC types, exhibit pronounced intensities, whereas amorphous variants (MQ, RM, and RE) display negligible intensities. Importantly, all other structural and compositional characteristics are consistent across the different variants, as they were derived from the same batch of material through controlled thermal treatments.

This indicates that an amorphous initial conformation strongly impedes the initial PLA molecular unit modification stages. Regarding the possible reasons for this hindrance, it is worth noting that amorphous and crystalline PLA exhibit almost identical water molecule diffusion coefficients and solubility[207], ruling out these factors as major contributors to the observed effect. Instead, since the primary distinction between amorphous and crystalline PLA lies in the packing of helical chains, the source of the effect likely relates to how chain interactions facilitate or inhibit the reaction depicted in Figure 3.8. In this context, the results in Figure 3.14 suggest that the initial methyl-carbonyl hydrogen bonding reaction (Figure 3.8b) is significantly promoted within the specific environment of the α crystalline phase.

Given the observed role of crystallinity, it is important to note that although the observed phenomena primarily involve intramolecular mechanisms, likely independent of molecular weight, an indirect influence of molecular weight cannot be excluded. This influence may arise from its impact on the material's crystallization propensity.

3.4 Conclusions

The present investigation provides the first experimental overview of PLA modification under very low doses of ionizing irradiation, identifying the initial events of molecular unit perturbation. The spectroscopic results offer new insights into the radiation-activated groups that prime the material for conformational and morphological evolution under higher irradiation doses. Specifically, evidence is presented for forming C=C groups in the polymer backbone, accompanied by the transformation of methyl groups into alkene CH_2 groups and the hydroxylation of carbonyl groups. These mechanisms occur without significant chain scission, which has been reported to dominate at much higher irradiation doses in the literature.

During prolonged irradiation, however, the radiation-activated groups diminish, driving the polymer chains toward conformational rearrangements, as reflected by a reduction in the glass transition temperature. Notably, the activation of these mechanisms at low doses is impeded by the reduction in the material's crystalline features, highlighting the role of conformation in determining PLA radiation hardness and its susceptibility to molecular unit damage.

These findings suggest potential strategies for optimizing PLA-based materials for specific applications by tailoring their radiation hardness and biodegradability through appropriate thermal treatments, such as crystallization or amorphization, or by controlled irradiation. Furthermore, this work opens new pathways for designing improved PLA production processes, enabling applications that require enhanced performance under radiation exposure.

CHAPTER
FOUR

TUNING THE CRYSTALLINITY OF POLY(LACTIC ACID) MICROSPHERES

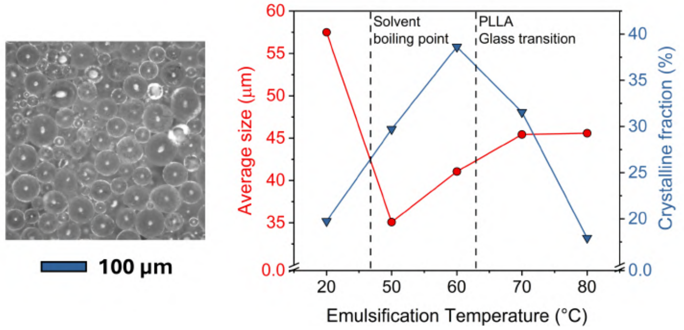

Part of this chapter has been published as:
G. Tamburini, G. Tarricone, S. Piva, A. Sassella, S. Bertagnoli, R. Lorenzi, A. Paleari,
Tuning crystallinity of poly(L-lactic acid) microspheres through emulsification temperature changes,
Macromolecules **2024**, 57 (18), 8826-8836.

4.1 Introduction

In various industrial and medical applications of poly(lactic acid) (PLA) microspheres, the polymer's crystallinity significantly influences their processes and functionalities [56, 131]. The degree of crystallinity in PLA microspheres significantly affects their mechanical properties, thermal stability, and biodegradability, which are vital in ensuring the material's effectiveness in its intended applications. For instance, in additive manufacturing, PLA crystallinity is crucial for the feasibility of laser sintering using microsphere powders. Here, the crystalline structure impacts the material's melting behavior, directly affecting its ability to fuse effectively during the sintering process [208]. In medical contexts, crystallinity impacts the biodegradability of the material, as more crystalline forms tend to degrade more slowly compared to their amorphous counterparts, as well as the release rate of encapsulated molecules. This factor is essential when PLA is used as a biocompatible and biodegradable drug carrier, as it governs how quickly or slowly therapeutic agents are released into the body [117, 209–213]. Moreover, crystallinity also affects the material's response to ionizing radiation [179, 214], with implications for applications such as sterilization, radiotherapy, and functionalization processes.

The crystalline phases in PLA materials arise from the organized packing of polymer helical chains, specifically the 10_3 (α form) and 3_1 (β form) helices [85, 89, 90, 109, 215, 216]. The extent and type of crystalline order depend on the polymerization of L and D enantiomers of lactic acid, whether in an ordered or random distribution [141, 217]. When the polymerization process produces a disordered arrangement, the resulting material tends to be more amorphous in nature, which may affect its mechanical and thermal properties. Additionally, including certain additives, such as poly(ethylene glycol), can further reduce the order level within the polymer matrix, leading to an amorphous structure that may be more suitable for specific applications [218].

Control over the crystallinity of PLA typically involves adjusting the ratio of L to D enantiomers or adding suitable additives, which can influence the overall structure and performance of the material [131, 141, 217, 218]. Confinement effects, such as those in ultrathin films, microfibers, or droplets, also play a role in influencing crystallinity, with smaller scales often promoting a higher degree of crystallization [219–223]. Additionally, internal surfaces within crystalline domains can affect the balance of crystalline and amorphous fractions in microsized polymer systems, further complicating the manipulation of crystallinity [95, 224, 225]. Besides synthesis techniques, thermal treatments are often employed to modify crystallinity, with the evidence available on the impacts of post-synthesis thermal treatments on PLA microspheres [131, 208]. However, using additives to regulate the properties of materials, especially in the medical field, presents certain risks. These include the unpredictable release of additives within the human body, which could potentially have adverse effects on patients, highlighting the need for careful consideration and regulation of materials used in medical applications.

In addition to the synthesis and additives involved in controlling crystallinity, the emulsification process used during microsphere production plays a key role. By adjusting the emulsification temperature, typically varying within a range of $10-20\,^{\circ}\mathrm{C}$, researchers have observed changes in the size distribution of the resulting microspheres [139, 144, 158, 226]. While this approach has been reported in the literature, there remains a lack of diffractometric or spectroscopic data to confirm whether emulsification temperature alone can reliably control the crystallinity of PLA microspheres. This gap in understanding necessitates further exploration to determine the most effective methods for controlling the crystalline structure of PLA.

This chapter aims to experimentally explore innovative strategies to manipulate the crystallinity of PLA microspheres, specifically by varying the emulsification temperature above the boiling point of the organic solvent and exceeding the polymer's glass transition temperature. Additionally, this chapter investigates the potential formation of crystalline and amorphous microstructures in pure poly(L-lactic acid) (PLLA) microspheres, and their responses to ionizing radiation. These experiments will provide valuable insights into the mechanisms of crystallinity modification and the potential implications of these modifications on the material's performance in medical applications.

4.2 Materials and methods

Batches of PLLA microspheres were synthesized using PLLA material ($M_w \sim 84\,\text{kDa}$) in the form of semicrystalline pellets weighing 15–20 mg each. The pellets were fabricated through hot extrusion at 180°C from bioproduced L-isomer and were thoroughly characterized using elemental analysis, thermogravimetric analysis, and spectroscopic methods. The PLLA pellets were then processed into a powder using an ultracentrifugal mill fitted with a 1 mm sieve. This powder was dissolved in dichloromethane (DCM, 99%) at a ratio of 10 mL DCM per 200 mg of PLLA powder, stirring the mixture at 20°C for 10 minutes until fully dissolved.

Microspheres were produced via an oil-in-water (O/W) emulsification process coupled with solvent evaporation, as depicted in Figure 4.1 and described in previous works [140, 227]. The organic PLLA solution was emulsified into a water-based solution of poly(vinyl alcohol) (PVA, $M_w \sim 31\,\text{kDa}$, hydrolyzation degree = 88%) under controlled temperature conditions. The aqueous phase was prepared by dissolving 375–3000 mg of PVA in 75 mL of water stirred at 40°C. Once fully dissolved, the PLLA/DCM solution was added to the aqueous phase under mechanical stirring at 500 rpm for two hours to ensure complete DCM evaporation. The emulsification temperatures (T_{emu}) were varied between 20 and 80°C. Care was taken to prevent foaming at $T_{\text{emu}} \geq 50\,^\circ\text{C}$, where the DCM exceeded its boiling point ($\sim 40\,^\circ\text{C}$). After synthesis, microspheres were cooled gradually to room temperature and washed to remove excess PVA. Some samples prepared at $T_{\text{emu}} \geq 50\,^\circ\text{C}$ were rapidly cooled in an ice bath at 0 °C for 20 minutes before washing. Residual PVA was confirmed to be absent using differential scanning calorimetry (DSC) analysis (Figure 4.2). The absence of a secondary melting peak near 250°C, alongside the primary peak at ~175°C attributed to PLA, confirms the absence of PVA residues in the microspheres.

Microspheres from each batch were drop-cast onto stainless steel discs (10 mm diameter) and allowed to dry for at least 8 hours to ensure complete solvent evaporation. To study microsphere formation kinetics, samples at varying T_{emu} were extracted at fixed intervals, with $t = 0$ defined as the time of organic phase addition and $t = 2\,\text{h}$ marking the end of synthesis. Optical microscopy images were captured for each aliquot,

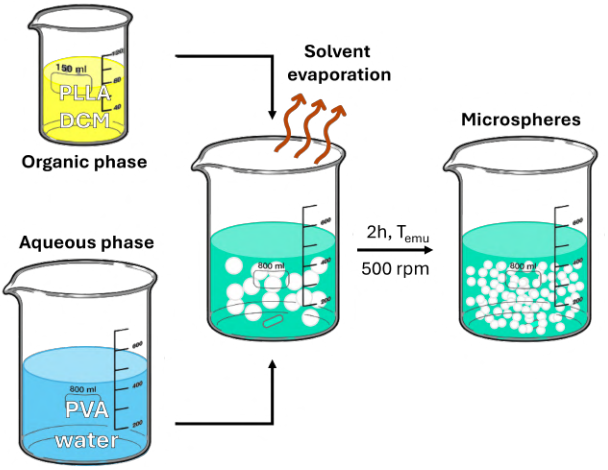

Figure 4.1: Schematic illustration showing the preparation of PLLA microspheres. The organic phase contains PLA dissolved in DCM, and the aqueous phase contains PVA. The emulsification (T_{emu}) ranges from 20 to 80°C.

and the average diameter of the microspheres was calculated. The crystalline and amorphous phases of the microspheres were characterized using powder X-ray diffraction (PXRD). The crystalline fraction was estimated by calculating the ratio of integrated narrow reflections to the total pattern, including the broad, amorphous halo. Thermal properties were determined using Differential Scanning Calorimetry (DSC), and Raman spectroscopy provided structural insights at the single-microsphere level. Spectral intensities were normalized to the skeletal C-COO stretching mode at 870 cm^{-1}, which served as an internal reference [109]. Surface and internal structures were examined by scanning electron microscopy (SEM). Microsphere sections were prepared by embedding the dried samples in epoxy resin and cutting them with a lapping machine. Each batch of microspheres was exposed to a 100 Gy dose of X-ray irradiation, applied using a tungsten target X-ray tube with a 20 kV accelerating voltage and 20 mA current. Post-irradiation analysis used attenuated total reflection Fourier-transform infrared (ATR-FTIR) spectroscopy. Intensities were normalized to the asymmetric CH_3

bending mode at 1450 cm^{-1}, which was unaffected by irradiation [124]. A reference sample from a DCM solution was prepared as a PLLA film and analyzed under identical conditions before and after X-ray exposure.

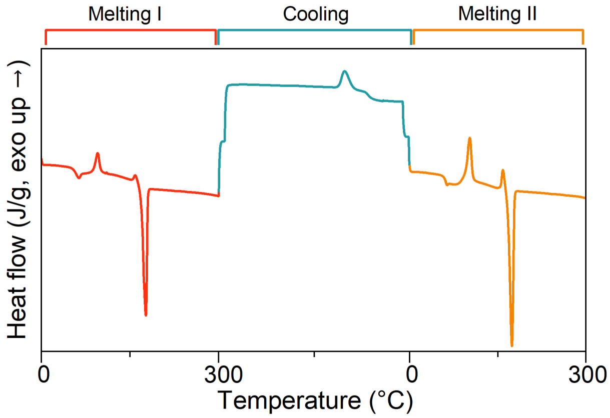

Figure 4.2: Thermal behavior of PLLA microspheres synthesized at room temperature, analyzed by differential scanning calorimetry (DSC) during heating-cooling cycles between 0 and 300°C to exclude the presence of residual PVA in the sample.

4.3 Results and discussions

Microsphere size and size dispersion

Figures 4.3a-e show representative optical microscope images of microsphere batches synthesized via emulsification at room temperature (Figure 4.3a) and at higher T_{emu} ranging from 50 to 80°C, with a fixed PVA concentration (1 w/v%) and natural cooling at room temperature. The size distributions are displayed as histograms in Figures 4.3f-j. Additionally, representative images of microspheres obtained through quenching are shown in Figure 4.4, where the effects are quite similar at $T_{\mathrm{emu}} < T_g$, while notable differences emerge at higher temperatures.

Figure 4.5 provides a comprehensive summary of the results from Figures 4.3 and 4.4, presenting data on the mean microsphere size, size standard deviation, and polydispersity index (PDI). The PDI is calculated as the square of the ratio of the standard deviation to the mean size. Regarding mean microsphere size (Figure 4.5a), a clear regime change is observed between microspheres synthesized at room temperature and those formed at elevated T_{emu}. Above the boiling point of the organic solvent, the mean size decreases significantly, with $T_{\text{emu}} \geq 50\,^{\circ}\mathrm{C}$ yielding much smaller microspheres.

The smallest mean size, 35 µm (29 µm for quenched samples), is observed at $T_{\text{emu}} = 50\,^{\circ}\mathrm{C}$, which is considerably smaller than the 58 µm size obtained at room temperature. As T_{emu} increases beyond 50°C, the mean size increases but remains smaller than at room temperature. Beyond $T_{\text{emu}} = T_g$, the mean size stabilizes but shows dependence on the cooling method, with quenched samples exhibiting larger sizes.

Figure 4.5b reveals three distinct regimes in size standard deviation. The first regime, from room temperature to $T_{\text{emu}} = 50\,^{\circ}\mathrm{C}$, shows a notable reduction in size standard deviation from 12 to approximately 7 µm, regardless of the cooling procedure. In the second regime, between $T_{\text{emu}} = 50$ and $60\,^{\circ}\mathrm{C}$, a slight increase in size standard deviation occurs, mirroring trends in mean size. The third regime, at $T_{\text{emu}} > T_g$, exhibits larger size distributions. In slowly cooled samples, no clear trend is observed between 70 and $80\,^{\circ}\mathrm{C}$, while quenched samples display an even greater size standard deviation, paralleling increases in mean size. Importantly, the calculated PDI values in Figure 4.5c remain below 0.1 across all conditions, indicating that emulsification produces highly monodisperse systems. Even at $T_{\text{emu}} = 50$ and $60\,^{\circ}\mathrm{C}$, where the highest PDI values are observed, the reduction in mean size is accompanied by a proportionally smaller reduction in size standard deviation.

These findings offer insights into the underlying mechanisms of emulsification. Changes in T_{emu} influence the physical properties of the solution, which, in turn, affect the emulsification process. Emulsification is governed by the interplay of two competing mechanisms: microsphere breaking and coalescence[228]. Microsphere breaking destabilizes the emulsion, fragmenting larger microspheres into smaller ones, while coalescence leads to the formation of larger microspheres by merging smaller ones. The

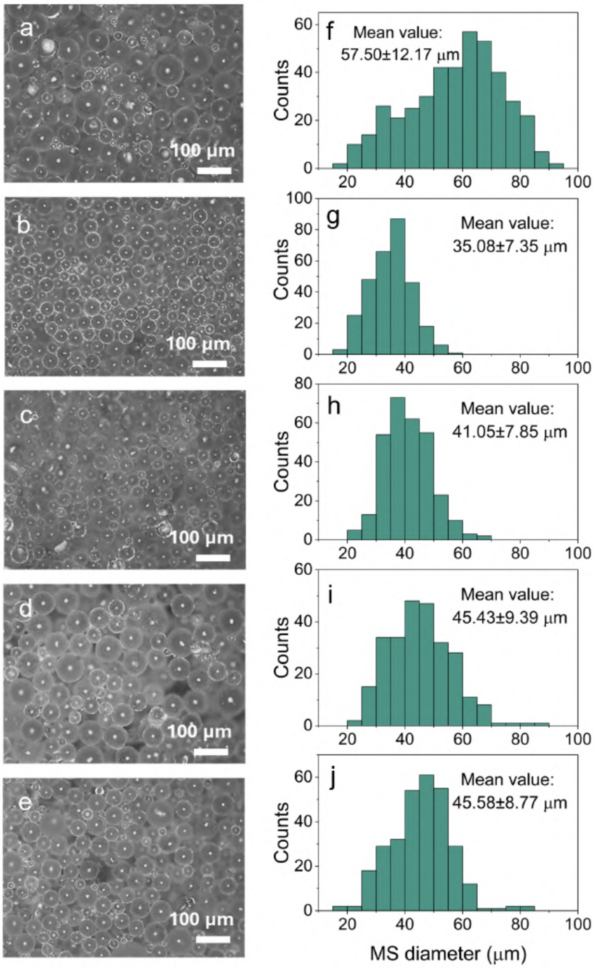

Figure 4.3: Microspheres vs. emulsification temperature: (a–e) Optical microscope images of microsphere batches prepared at emulsification temperatures of 20, 50, 60, 70, and 80°C, respectively. (f–j) Size dispersion histograms derived from analyzing the corresponding optical images (a–e). Values of the diameter mean value and relative standard deviation are also reported.

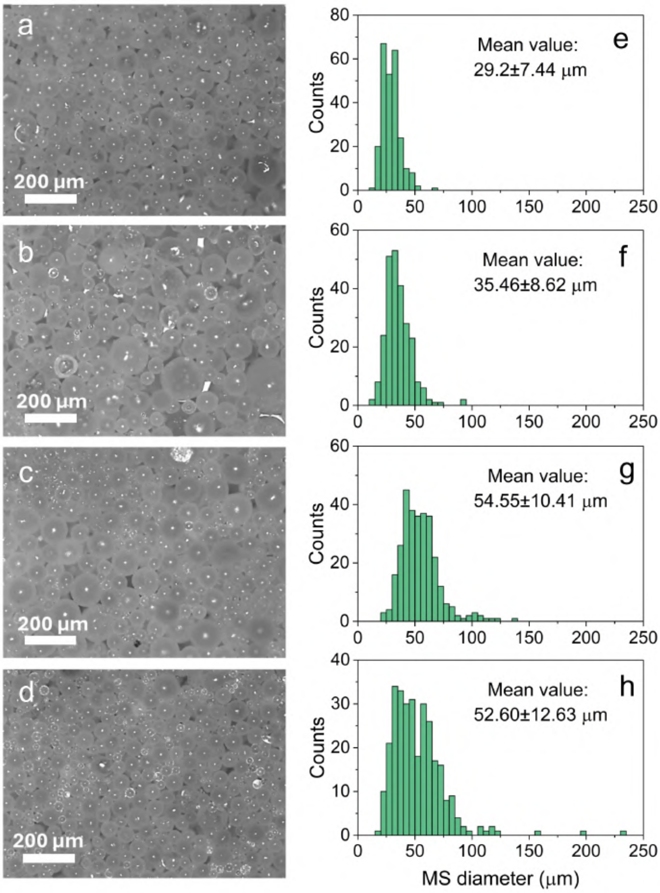

Figure 4.4: Microsphere size vs. emulsification temperature for quenched samples: (a–d) Optical microscope images of microsphere batches prepared at emulsification temperatures of 50, 60, 70, and 80°C, followed by quenching at 0°C, respectively. (e–h) Size dispersion histograms based on the analysis of the corresponding optical images (a–d). Values of the diameter mean value and relative standard deviation are also reported.

efficiencies of these mechanisms depend on various factors, including the ratio η_E/ρ_S (viscosity of emulsified species to solution density) for breaking, and $\sqrt{\rho_S/\eta_S}$ (solution density to viscosity ratio) for coalescence [228].

The observed changes in Figures 4.5a-b between T_{emu} = 20 and 50 °C coincide with exceeding the boiling point of DCM. At T_{emu} = 50 °C, rapid DCM removal results in a water-based emulsifying solution with lower density and higher viscosity compared to room temperature. These changes inhibit coalescence, maintaining smaller mean sizes, as seen in the second regime (50-60°C). At higher T_{emu}, the increased thermal energy promotes coalescence [229, 230], resulting in larger mean sizes at 70 and 80°C (Figure 4.5a) [231]. However, microsphere breaking is also enhanced at these temperatures, as the polymer viscosity (η_E) decreases significantly above T_g, resulting in a broader size distribution. The enhanced mobility of macromolecules within each microsphere makes breaking more probable, particularly as the size increases, increasing the number of smaller microspheres. This results in a mixed population of smaller and larger microspheres, further broadening the size distribution, as shown in Figure 4.5b.

Temporal size analysis of microsphere aliquots extracted at different times (30 s to 2 h) during synthesis at various T_{emu} (Figure 4.6) further highlights these competitive processes. Rapid size reduction occurs in the first 5 minutes, followed by slower kinetics. At T_{emu} = 70 and 80 °C, the negative slopes observed in the asymptotic behavior indicate a reversal in the size trend, suggesting a competitive balance between the breaking and coalescence mechanisms as time progresses [232].

Comparing slowly cooled and quenched samples (circles and triangles in Figures 2a-b, respectively) underscores the influence of cooling kinetics. Quenching at 0 °C rapidly freezes high-temperature size distributions immediately after stirring and heating stop, while slow cooling allows further microsphere breaking, modifying the size distribution. This effect is more pronounced at high T_{emu}, while differences are minimal at lower T_{emu}, below T_g.

Polymer morphology also influences microsphere stability. Factors such as chain viscosity, crystallinity, amorphous fractions, and porosity play significant roles in determining microsphere stability during emulsification and in the final product. Sub-

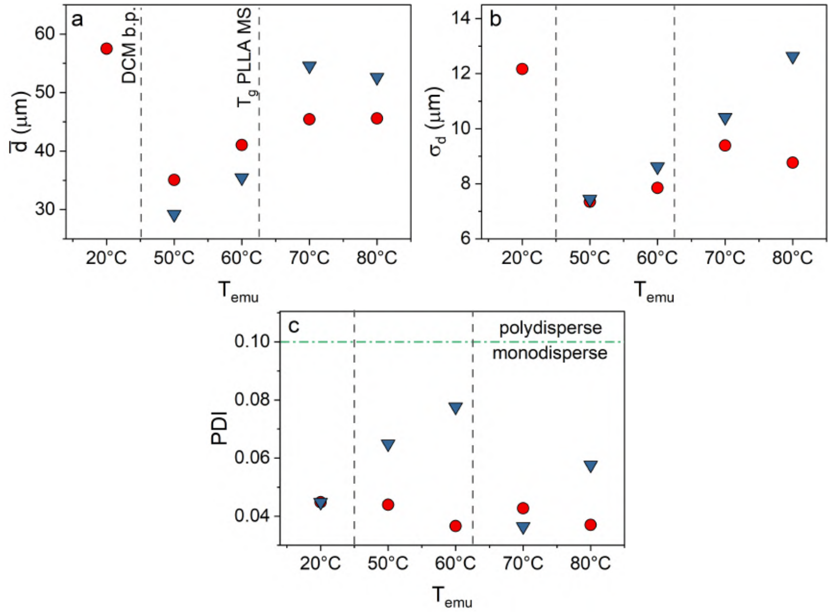

Figure 4.5: Microsphere size and dispersion analysis: (a) Mean size ($\bar{d}$), (b) size standard deviation (σ_d), and (c) polydispersity index (PDI) as a function of emulsification temperature, derived from histograms. Data are shown for batches cooled naturally after 2 hours of heating (red circles) and quenched at 0°C (blue triangles). Dashed lines indicate the boiling point of the organic solvent (DCM) and the glass transition temperature (T_g) of PLLA microspheres.

sequent sections provide data on crystallinity through PXRD and DSC, and detailed single-microsphere analyses via Raman spectroscopy and SEM.

Crystallinity vs emulsification temperature

The PXRD analysis of microspheres from various batches reveals the coexistence of amorphous and crystalline phases across all investigated samples, as depicted in Figure 4.7. Specifically, the PXRD patterns in Figure 4.7 display six distinct narrow reflections in the 10–25° region, characteristic of crystalline PLLA in the α-phase, alongside a broad halo centered at approximately 17°, attributed to the amorphous PLLA phase.[233, 234]

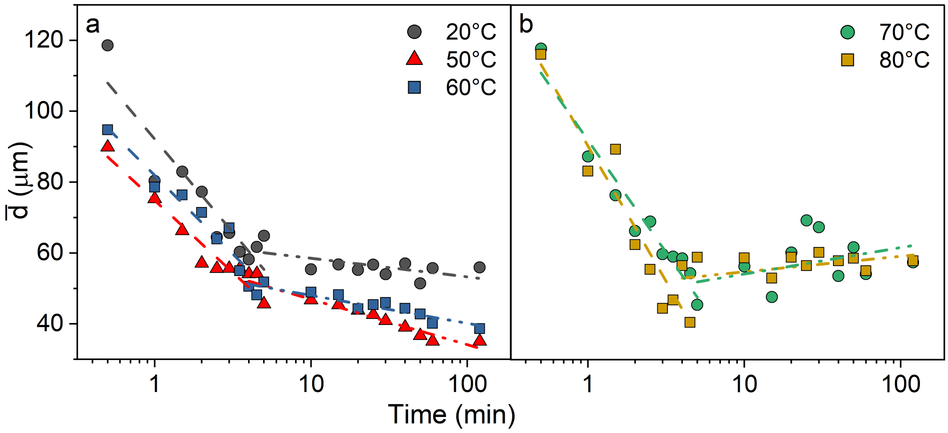

Figure 4.6: Kinetics of microsphere size evolution: Mean size calculated from aliquots taken at different time intervals after pouring the organic PLLA solution into the aqueous PVA solution at (a) 20, 50, and 60°C and (b) 70 and 80°C. Lines serve as visual guides, with dashed lines representing a linear fit for data between 30 seconds and 5 minutes, and dashed-dotted lines representing a linear fit for data between 5 minutes and 2 hours.

The narrow reflections also include weaker peaks of the α-phase (e.g., near 21°, which are absent in the parent bulk material), indicating a high degree of crystallinity.

Notably, the PXRD patterns demonstrate that the proportion of the crystalline phase varies with emulsification temperature and is further influenced by the cooling process. The volume fraction of crystalline phases, summarized in Figure 4.8, highlights several key observations. Below T_g, emulsification at temperatures above room temperature promotes cold crystallization, increasing the crystalline PLLA content from under 25% to 40–50%. Within this range, cold crystallization is facilitated as temperatures approach T_g, likely due to enhanced chain mobility that enables structural rearrangement.

Conversely, at $T_{\text{emu}} > T_g$, higher temperatures appear to hinder microsphere crystallization. In this regime, competing mechanisms of emulsion destabilization and coalescence, thermally activated at elevated T_{emu} (Figure 4.5), significantly impact the crystallinity. This effect is more pronounced in samples subjected to slow cooling from high temperatures compared to quenched samples.

Given that quenched samples exhibit broader size distributions, particularly skewed toward larger microspheres (Figure 4.5), this raises the question of whether a relationship exists between size and crystallinity, especially for microspheres formed above T_g. This question is further explored in subsequent sections, where DSC, micro-Raman data, and SEM analysis provide additional insights.

Microsphere crystallization propensity

In Figure 4.9, we present the results of the DSC analysis performed on the investigated microsphere batches. The DSC curves, consistent with the literature on PLLA thermal properties [131], exhibit three key features. The first feature observed just above 60°C corresponds to the material's glass transition temperature (T_g). At higher temperatures, certain samples display an exothermic cold crystallization peak at T_c, occurring just below 100°C. This peak indicates a solid-state rearrangement of macromolecules into a crystalline phase, facilitated by increased molecular mobility above T_g. At even higher temperatures, an intense endothermic peak is observed near the melting temperature (T_m) at around 175°C.

As shown in Figure 4.9a, the glass transition, cold crystallization, and melting temperatures remain largely independent of the emulsification temperature, with T_g = 61 ± 2°C, T_{cc} = 96.0 ± 0.5°C, and T_m = 175.5 ± 0.5°C. Exceptions include a lower T_g = 56 ± 1°C in the sample prepared at room temperature and a reduced T_{cc} = 86 ± 0.5°C in the sample emulsified at 50°C and quenched at 0°C. However, the cold crystallization enthalpy (ΔH_{cry}) varies significantly with T_{emu}, reaching its lowest value in microspheres prepared at 60°C, irrespective of the cooling method. This result aligns with the PXRD data in Figure 4.7, which reveals the largest crystalline fraction in the same batches and, consequently, the lowest amorphous fraction available for cold crystallization compared to other samples. Despite this agreement, the overall ΔH_{cry} values (Figure 4.9(b)) only partially reflect the dependence of crystalline fraction on T_{emu} seen in the PXRD analysis. Specifically, ΔH_{cry} appears qualitatively anticorrelated with the non-monotonic trend of the crystalline fraction (Figure 4.7) for microsphere batches

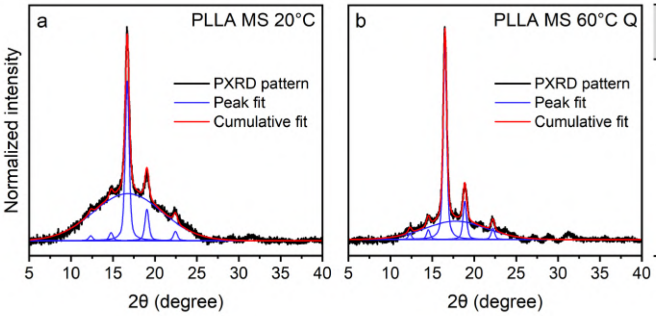

hkl	2θ (deg)	A_{rel} (60C Q)
103	12.37±0.01	0.030
010	14.65±0.04	0.051
200/110	16.61±0.02	1.000
203	18.97±0.02	0.198
210	22.35±0.03	0.058

Figure 4.7: Normalized powder X-ray diffraction patterns of two representative microsphere batches prepared at different T_{emu} – (a) room temperature, and (b) 60°C followed by a quenching at 0°C– showing a different amorphous halo. All the patterns were normalized to the most intense reflection at 16.6°. The cumulative fittings (red), obtained from the single peak fit (blue), show good agreement with the experimental data (black). The table presents the reflection angles obtained from the fitting of the reference pattern (60°C quenched sample), along with the normalized peak intensities and indices corresponding to the crystalline structure as reported in the literature [233, 234].

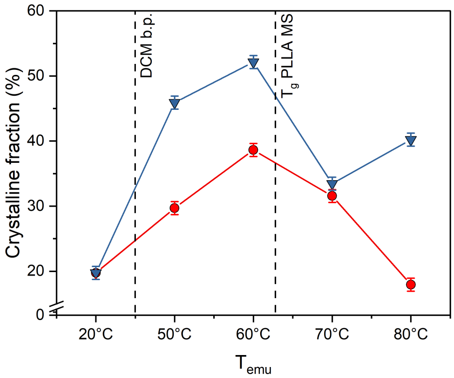

Figure 4.8: Crystalline fraction as a function of emulsification temperature for microsphere batches obtained via slow cooling (circles) and quenching to 0°C (triangles), estimated from the analysis of crystalline and amorphous phase contributions in the PXRD patterns. Dashed lines indicate the boiling point of the organic solvent (DCM) and the glass transition temperature (T_g) of PLLA microspheres. Solid curves serve as guides for the eye.

Table 4.1: Average crystallite size (D) – calculated from the Scherrer equation using the angle of the 200 reflections and its FWHM – for different microsphere samples synthesized at different T_{emu} from slow cooling and quenching to 0°.

	Slowly cooled MS			Quenched MS		
T_{emu} (°C)	Angle (2θ)	FWHM	D (nm)	Angle (2θ)	FWHM	D (nm)
20	16.70	0.5396	15.55	–	–	–
50	16.65	0.4848	17.30	16.59	0.4736	17.71
60	16.59	0.4816	17.42	16.64	0.4079	20.56
70	16.59	0.4636	18.09	16.62	0.5297	15.84
80	16.64	0.4391	19.11	16.61	0.4131	20.31

subjected to slow cooling. From the PXRD spectra using the most intense reflection at approximately 16.6°, it was possible to calculate the average crystallite size (D) using the Scherrer equation, $D = \frac{K\lambda}{\beta\cos(\theta)}$. The results presented in Table 4.1 validate the trend in crystalline fraction within the sample: as crystallinity increases, the crystallites become larger.

Additionally, several noteworthy observations emerge from the DSC data. The cold crystallization enthalpy, in many cases just a few J/g, is lower than expected for crystallization from an amorphous fraction exceeding 50–60%, as indicated by PXRD. Reported ΔH_{cry} values for largely amorphous PLLA typically exceed 20 J/g.[131, 217, 233] The ΔH_{cry} values span a wide range, differing by up to a factor of 5 (from 2.5 to 17 J/g), while the amorphous fraction varies by only a factor of 0.5 (from 50–60% to 75–80%). Furthermore, quenching samples from $T_{\text{emu}} > T_g$ results in a notable increase in crystallinity compared to slow cooling. These findings suggest that a portion of the amorphous phase in the microsphere system is constrained against cold crystallization and does not participate in the thermally activated process near 95°C as detected in DSC.

Quantitatively, the gap between the amorphous fraction derived from PXRD and the fraction available for cold crystallization can be estimated using the DSC curves as $(1 - -\chi_{\text{cry}}^{\text{DSC}})$, where $\chi_{\text{cry}}^{\text{DSC}} = (h_m - -h_c)/h_m^{\text{crys}}$. Here, h_c and h_m represent the cold crystallization and melting enthalpies, respectively, and $h_m^{\text{crys}} = 93$ J/g is the reference

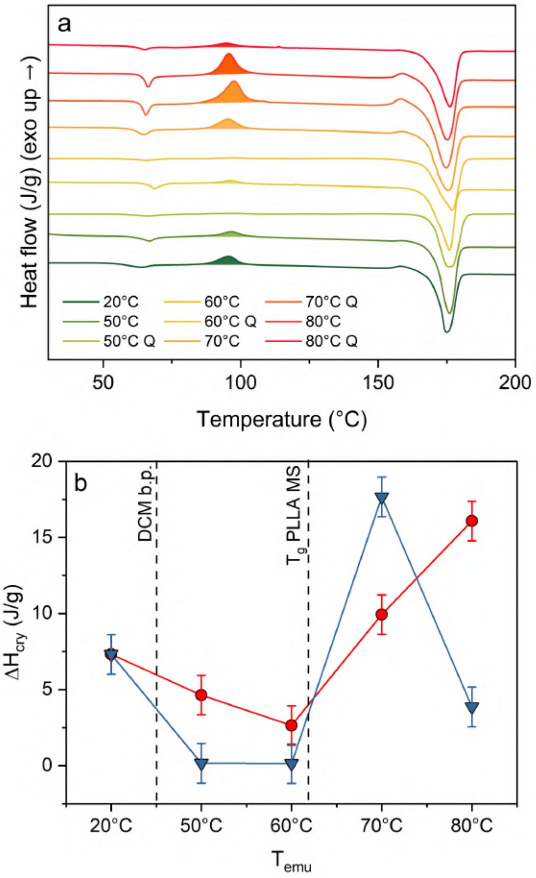

Figure 4.9: (a) Differential scanning calorimetry (DSC) curves of microsphere batches prepared by emulsification at the indicated temperatures, followed by either slow cooling or rapid quenching at 0°C (denoted as Q in the curves). (b) Cold crystallization enthalpy values, determined from the integrated area of the exothermic cold crystallization peaks around 95°C in (a), plotted as a function of emulsification temperature (T_{emu}) for slowly cooled (triangles) and quenched (circles) microsphere batches.

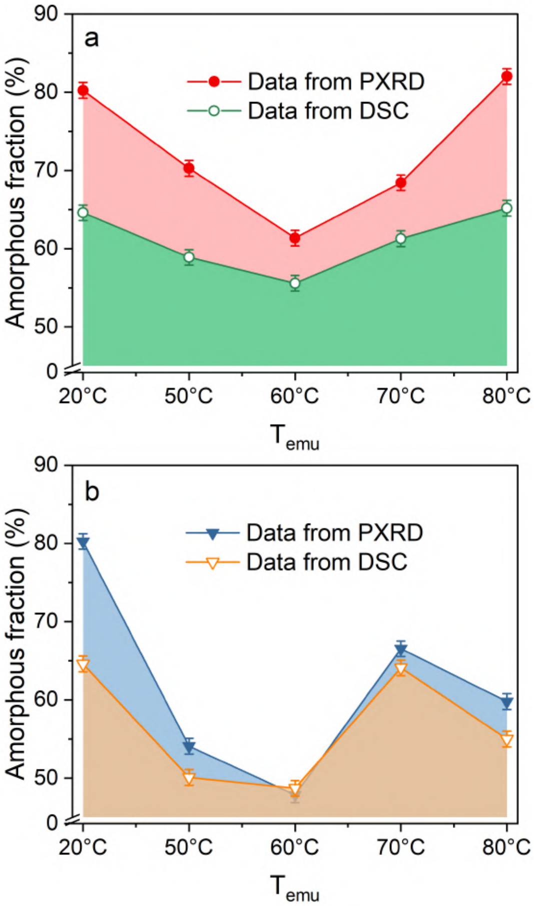

Figure 4.10: (a) Total amorphous fraction calculated from PXRD analysis (filled markers) and DSC curves (open markers) for microsphere batches emulsified at different temperatures followed by slow cooling. (b) The same analysis as in (a), but for microsphere batches rapidly cooled by quenching at 0°C.

melting enthalpy of 100% crystalline PLLA [131, 141, 208, 217]. Figure 4.10 illustrates the observed gap, which suggests the presence of a rigid amorphous phase within the microspheres, influenced by T_{emu}. As Figures 4.3 and 4.7 indicate, T_{emu} affects microsphere formation, size distribution, and polymer chain packing, particularly near or above T_g, impacting the crystallinity and amorphous fractions.

Two primary factors likely influence the size dependence of crystallinity and the residual amorphous fraction resistant to cold crystallization. First, the interaction of PLLA chains with microsphere interfaces, including potential surface and volume effects dependent on size distribution, plays a significant role. Second, thermally activated polymer chain mobility, driven by temperature changes across T_g, also affects crystallinity. Based on these considerations, two limiting scenarios can be proposed. In the first scenario, the microsphere ensemble consists of two subsets: primarily amorphous microspheres and predominantly crystalline microspheres, with size as the key parameter inhibiting cold crystallization above or below a threshold size. In the second scenario, each microsphere comprises both crystalline and amorphous regions, with a portion of the amorphous region forming a rigid phase resistant to cold crystallization. Here, the rigid fraction's size dependence influences the cold crystallization propensity.

As the surface-to-volume ratio increases with decreasing microsphere size, the data in Figure 4.10 suggest that the rigid amorphous fraction decreases with increasing total surface area. This observation aligns with prior studies showing enhanced interface chain packing propensity, leading to higher cold crystallization [221, 223, 224]. The next section, supported by micro-Raman and SEM analyses, favors a model aligning with the second scenario.

Single-microsphere crystallinity

Figure 4.11a presents representative micro-Raman spectra obtained from single microspheres of similar sizes (depicted in the inset images) within the spectral range of 130–1200 cm^{-1}. This range highlights intrinsic vibrational modes that offer insights into the crystallinity of the polymer [109, 214, 235]. In particular, the low-energy regions, including the τ(CC) skeletal chain torsion and δ(COC) and δ(CCO) chain deformation modes (from 200 to 600 cm^{-1}), show narrow and split features in semicrystalline materials, which gradually merge into a single unstructured spectral peak in amorphous materials. A broadening characteristic of the amorphous state is also evident in the 700–750 cm^{-1} range, associated with the δ(C–O) modes, and even more pronounced at 922 cm^{-1}, where only semicrystalline materials exhibit a resolved weak peak attributed to the coupling of ν(C–C) backbone stretching with the CH_3 rocking mode.

The crystallinity of the microspheres influences the ability to resolve twin peaks near 410 cm^{-1}. In Figure 4.11b, the intensity of the peak-to-saddle ratio, after normalization to the intensity at the saddle point, is presented as a measure of crystallinity. This intensity is selectively sampled for subsets of ”small” microspheres (smaller than 30–40 µm) and ”large” microspheres (larger than 40–50 µm). Similar results are obtained when normalizing the intensity of the 922 cm^{-1} mode to the strong 870 cm^{-1} mode, shown in Figure 4.11c. The size thresholds are based on the size distributions shown in Figure 4.3 to differentiate between small- and large-particle subsets.

The data in Figure 4.11 reveal two important observations. First, a notable increase in crystallinity occurs when the emulsification temperature (T_{emu}) exceeds room temperature, consistent with the PXRD and DSC results. Second, microspheres from batches quenched from T_{emu} (except for $T_{\mathrm{emu}} = 80^{\circ}$C) show slightly lower crystallinity compared to microspheres from slowly cooled batches, further confirming the consistency with other analyses. Importantly, no significant difference is observed between small and large microspheres within the same batch, except for the batch quenched from 80°C, which contains very large microspheres.

The absence of a significant difference in the Raman spectra of small and large microspheres within the same sample batch suggests that changes in the crystalline/amorphous phase ratio due to variations in T_{emu} are not driven by size-dependent effects that determine whether microspheres are crystalline or amorphous. Instead, these changes appear to be associated with T_{emu}-dependent mechanisms that influence the ordering and disordering of the internal microstructure, where each microsphere contains both crystalline and amorphous parts. Furthermore, mobile and rigid amorphous regions must be considered within the amorphous phase. This aligns with the observed discrep-

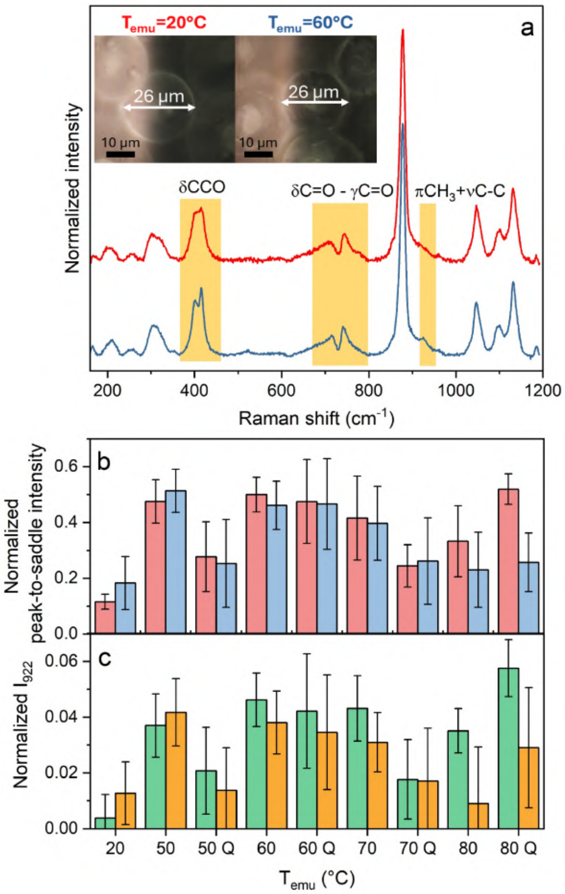

Figure 4.11: (a) Raman spectra of two similarly sized microspheres produced at 20°C (red curve) and 60°C (blue curve). Key spectral regions influenced by crystallinity are highlighted with corresponding vibrational mode assignments. Insets show optical images of the analyzed microspheres. (b) Crystallinity-dependent resolution of the Raman mode at 410 cm^{-1}, shown as peak-to-saddle mean intensity, and (c) the 922 cm^{-1} Raman mode. All the spectra were normalized to the 870 cm^{-1} mode. Data are categorized into ”small” microspheres (<30−40 µm, blue bars in (b), orange bars in (c)) and ”large” microspheres (>40−50 µm, red bars in (b), green bars in (c)) for various batches synthesized at the indicated T_{emu} (quenched samples are labeled Q). Error bars denote standard deviations from six microspheres per batch.

ancy between the amorphous fraction from PXRD and the cold crystallization propensity indicated by DSC cold crystallization enthalpy.

The lack of a direct relationship between crystallinity and microsphere size is further confirmed by expanding the Raman analysis of PLLA features across a matrix of samples, varying both T_{emu} and emulsion composition with different PVA concentrations. The plots in Figure 4.12 summarize the results, showing changes in mean size, polydispersity index (PDI), and crystallinity (as indicated by the narrowing of the 410 cm^{-1} Raman mode) as a function of T_{emu} and PVA concentration (w/v %). While the data for 1% PVA vs T_{emu} might suggest that crystallinity is associated with smaller microspheres (with the highest crystallinity in batches with the smallest mean size), the data at $T_{\text{emu}} = 60^{\circ}\text{C}$ (and 80°C) versus PVA concentration reveal a nonmonotonic trend in crystallinity, with two minima at 0.5 and 4 w/v % PVA. This pattern does not correspond to the monotonic decrease in mean size, further supporting the presence of both crystalline and amorphous phases in each microsphere, as suggested by the statistical analysis of single-microsphere Raman measurements.

Further details regarding the morphology of the microspheres are provided by SEM analysis. Figure 4.13 presents SEM images of microspheres from the batch prepared at 80°C with slow cooling, with similar features observed in samples from other batches (not shown). Panels (a) and (b) show the external appearance of the microspheres at two magnifications, while panels (c) and (d) reveal the internal structure of microsphere sections embedded in epoxy resin. Notable features include the very smooth surface of the microspheres, with no detectable porosity. The sectioned images confirm that the inner structure is compact, without significant porosity. SEM analysis also identifies a few microspheres with internal spherical cavities (several micrometers in diameter), likely formed from bubbles during DCM evaporation at the end of the synthesis (Figure 4.14).

Microsphere radiation hardness

PLLA crystallinity is a key factor that affects not only biodegradability [117, 131] but also the radiation resistance of the material, as demonstrated in bulk in the low-dose X-ray

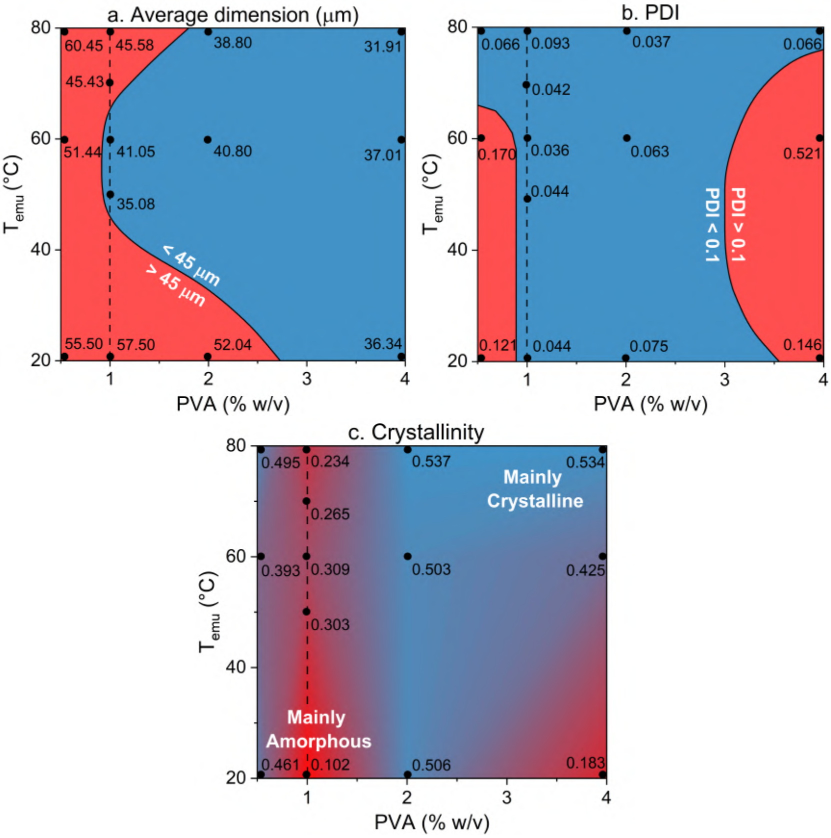

Figure 4.12: (a) 2D plots of microsphere mean size and (b) microsphere PDI index, based on optical microscopy analysis, alongside (c) mean microsphere crystallinity determined by the spectral narrowing of the 410 cm^{-1} Raman mode as shown in Figure 4.11. Black points and numbers represent experimental values. Dashed lines highlight the sections corresponding to samples with results detailed in Figures 4.3 – 4.11. In (a) and (b), contour lines serve as visual guides, distinguishing regions of high and low experimental values relative to the reference values marked in white (45 μm for average dimensions, 0.1 for PDI). In (c), no contour lines are displayed; instead, regions predominantly amorphous or crystalline, as inferred from Raman analysis, are arbitrarily indicated.

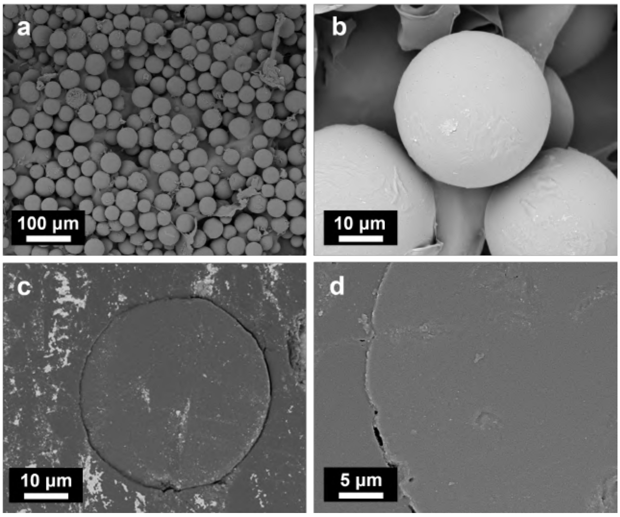

Figure 4.13: (a) SEM image of a microsphere ensemble produced via emulsification at 80°C. (b) Higher magnification image revealing the smooth surface morphology of microspheres from the same batch. (c) SEM image of a microsphere cross-section from the same batch, prepared by embedding the microspheres in epoxy resin, polishing the surface, and applying a thin gold metallization layer (visible straight lines are polishing marks). (d) Higher magnification image of the microsphere cross-section.

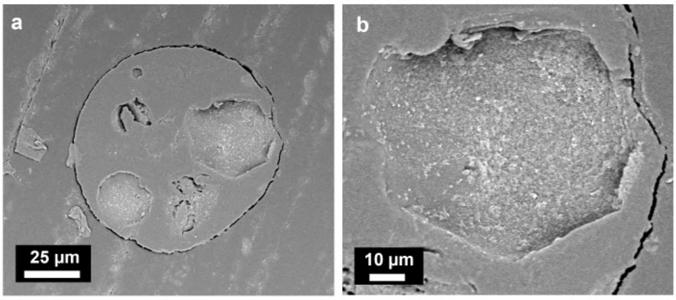

Figure 4.14: (a) SEM image of a microsphere cross-section synthesized at 80°C, showing internal hollow cavities formed by evaporated DCM. (b) Magnified view of a cavity, revealing details of the internal structure.

range in [214]. Given the importance of PLLA's radiation resistance in various applications involving PLLA microspheres, this study represents the first investigation into the effects of ionizing radiation on PLLA microspheres in the low X-ray dose range. Figure 4.15 shows the infrared spectra of irradiated (100 Gy) and unirradiated microspheres, alongside spectra from reference samples of bulk as-extruded PLLA and PLLA film obtained by solvent evaporation of the same material (dotted spectra). The spectral regions around 1600 and 3000 cm^{-1} are expected to provide evidence of potential radiation-induced modifications to the molecular structure. Specifically, C=C modes around 1650 cm^{-1}, -CH_2 alkane modes around 2900 cm^{-1}, and intrachain OH stretching modes near 3200 and 3400 cm^{-1} were identified as the primary radiation-induced changes in bulk PLA [214] and in the reference samples shown in Figure 4.15 (labeled as "Bulk PLA" and "Film"). The absence of these modes in the spectra of irradiated microspheres indicates a higher radiation resistance in the microspheres compared to the semicrystalline bulk. This result can be partially explained by the presence of a large amorphous fraction in PLLA microspheres (Figure 4.7), as weaker effects, if any, are expected in amorphous bulk samples [214]. However, it is noteworthy that no radiation-induced effects were observed in the irradiated microspheres, even though a non-negligible crystalline fraction was present, as evidenced by PXRD analysis. This suggests a relationship between the differing responses to ionizing radiation and the varying degrees of crystallinity in the two systems—specifically, the crystalline fraction in microspheres is higher than in the bulk material. No significant shifts typically associated with defects or disorder (such as in the α' phase) were detected [236]. Slightly different polymer chain packings in the crystalline fraction of bulk and microspheres might influence the likelihood of intrachain hydrogen bond formation due to irradiation. In other words, interchain interactions in the bulk and microspheres may be sufficiently distinct to either inhibit or promote modifications to the molecular structure.

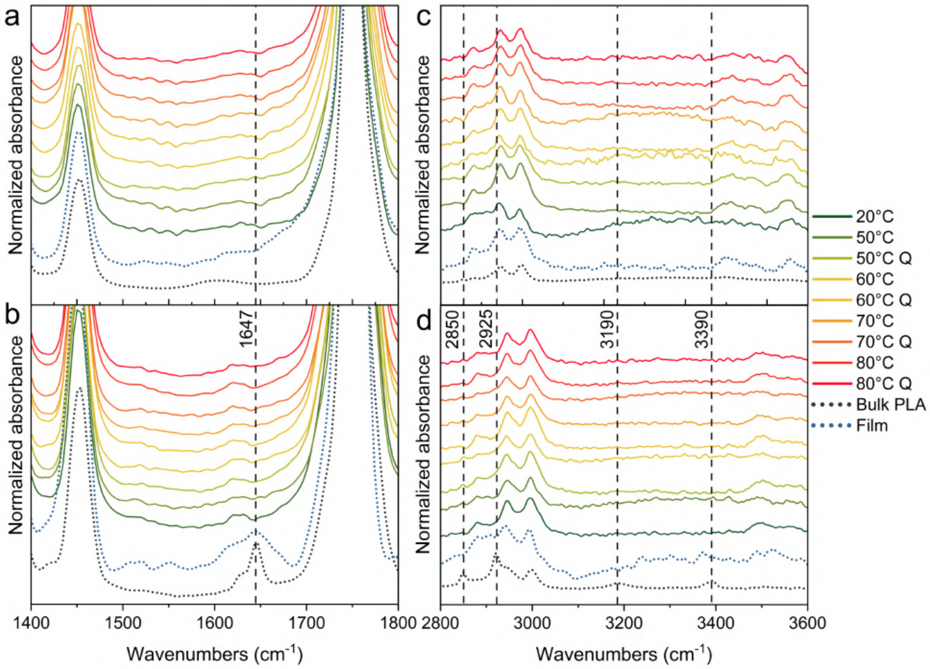

Figure 4.15: ATR-FTIR spectra of microsphere samples measured (a, c) before and (b, d) after exposure to 100 Gy X-ray irradiation in the ranges 1400–1800 cm^{-1} and 2800–3700 cm^{-1}. Samples were produced via emulsification at T_{emu} ranging from 20 to 80°C, with either slow cooling or quenching (labeled Q). Comparisons are made with bulk as-extruded PLLA (labeled "Bulk PLA") and a PLLA film prepared by solvent evaporation ("Film") using the same raw material. Dashed lines highlight vibrational modes associated with X-ray-induced modifications in the PLLA molecular unit of α-phase bulk PLLA.

4.4 Conclusions

A new framework has emerged for understanding the factors that govern the crystallinity of PLLA microspheres produced via emulsification. A comparison of PXRD analysis, DSC curves, and single-particle Raman scattering spectra reveals that microsphere batches produced at various temperatures (ranging from 20 to 80°C) and subsequently cooled either slowly or through rapid quenching exhibit different degrees of crystallinity, ranging from less than 20% to over 50%. Notably, the variation in crystallinity with emulsification temperature and cooling process reflects the internal structure of individual microspheres, specifically the relative crystalline and amorphous fractions within each particle. The nonmonotonic temperature dependence of crystallinity and the size distribution across a broad temperature range, including the glass transition region, underscores the need to consider both interparticle and intraparticle mechanisms. These include emulsion destabilization, particle coalescence, polymer chain mobility, crystal domain nucleation, and the stabilization of metastable structures. Moreover, FTIR analysis of X-ray-irradiated microspheres reveals aspects of radiation resistance that are potentially relevant for specific applications. The crystalline fraction within the microspheres contributes to a high degree of crystallinity, which exceeds that of the parent bulk material, thereby enhancing the structural stability of the material. In conclusion, the findings presented in this study provide a refined understanding that can guide the design of new synthesis strategies for PLLA microspheres with tailored structural and physical properties. Specifically, the results demonstrate that emulsification temperature can control the arrangement of crystalline and amorphous PLLA chains within the microspheres, thus paving the way for further fundamental studies of the internal microstructure in polymeric colloidal systems under novel conditions.

CHAPTER FIVE

EUROPIUM-MODIFIED POLY(LACTIC ACID) MICROSPHERES

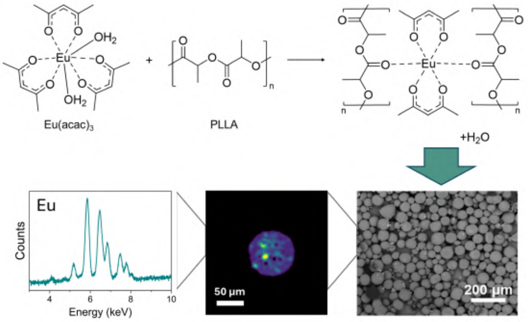

Part of this chapter will be submitted shortly as an article:
G. Tamburini, F. Gasser, E. Machado Charry, R. Resel, S. Bertagnoli, G. Tarricone, S. Piva, A. Sassella, R. Lorenzi, A. Paleari. *Eu-modified poly (L-lactic acid) microspheres with enhanced crystallinity and stability by incorporation of rare-earth ions interacting with polymer chains via temperature-tuned emulsification*,

In preparation, to be submitted.

5.1 Introduction

Polymers encapsulating lanthanide compounds are widely studied for their potential in diverse applications, from optoelectronics to medical therapies. These polymers are integral in devices including LED displays [237, 238], transparent films for luminescent solar concentrators [239], light-conversion coatings in solar cells [240], polymeric optical sensors for thermochemical parameters [241, 242], and polymer microspheres containing radioisotopes for internal radiotherapy [152–154]. The local environment of functional ions – serving as light emitters or activatable radioisotopes depending on the application – is significantly influenced by the choice of lanthanide compound used in the polymer functionalization process. Lanthanide compounds can, in turn, affect the crystallinity, density, and porosity of the polymer matrix, impacting both the system's functionality and the chemical and structural stability of the material. These interactions may lead to critical consequences, such as reduced light emission yields in luminescent systems, the release of radioactive lanthanides from microcarriers during medical protocols, and changes in the mechanical properties and stability of the polymer matrix in macro or micro-devices. Recent studies have explored the stability of functional and structural properties in lanthanide-containing polymers derived from various synthesis strategies and precursor compounds [241].

In the context of polymer microspheres for internal radiotherapy, research has primarily focused on medically significant factors, such as the retention of radioactive species, as well as the biocompatibility and biodegradability of the microsystems [154]. Poly(lactic acid) (PLA) has emerged as a preferred matrix material due to its excellent biocompatibility. In such systems, one of the key challenges in designing PLA-based microspheres for radiotherapy is achieving an effective balance between biodegradability and radiation hardness—two properties that are often competitive. Biodegradability ensures that the microspheres are safely eliminated from the body once they have served their therapeutic purpose. In contrast, radiation hardness is essential to prevent the premature release of radioisotopes before they have decayed sufficiently. This delicate balance has been the subject of several studies investigating the morphological evolution of microspheres over time and the release of encapsulated species under irradiation or in buffer solutions [209, 212]. Developing effective medical protocols using polymer-based microcarriers requires a thorough understanding of the role played by polymer structure in initiating radiation-induced damage and how this damage can be minimized or controlled. A few studies have explored the effects of different synthesis conditions and varying irradiation doses on PLA microspheres, even in the early stages (Chapter 3) [168, 214]. Furthermore, research on PLA microspheres has also addressed how factors such as crystallinity and the ratio of mobile to rigid amorphous fractions depend on emulsification processes, including the proportions of the compounds involved and the synthesis temperature, as already presented in Chapter 4 [226, 243].

In lanthanide-doped polymer systems, most investigations have focused on the light emission properties of polymer or blend films prepared with rare-earth ions, and the radiation hardness and retention of lanthanide ions in microspheres designed for radiotherapy. Typically, lanthanides are incorporated into these systems using organic molecules like acetylacetonate or other chelating agents, which facilitate their stable incorporation into the polymer matrix [241, 244]. However, the focus has been chiefly on optimizing the luminescent properties for applications in optoelectronics and sensors, with less attention given to the potential impact of lanthanide doping on the mechanical, chemical, and stability characteristics of polymeric materials used for radiotherapy.

This chapter aims to advance the understanding and control of the mechanisms driving the incorporation of a chosen rare-earth ion, e.g., europium, into PLA microspheres. Specifically, it investigates the effects of incorporating europium(III) acetylacetonate dihydrate ($Eu(acac)_3(H_2O)_2$) into PLA during a temperature-controlled emulsification process. The focus is on determining whether and how the inclusion of europium alters PLA properties such as crystallinity, degradability, and radiation hardness. The investigation employs diffractometric, calorimetric, and spectroscopic techniques to provide insights into the coordination environment of europium ions and their influence on the polymer structure. Initially, the structural and morphological characteristics of the synthesized material are presented, including microsphere size, PLA crystallinity, biodegradability, and radiation hardness, with attention to the effects of europium incorporation at various emulsification temperatures. Complementary results from photoluminescence and IR spectroscopy, as well as variable-temperature X-ray diffraction, are then discussed to elucidate how Eu^{3+} ions integrate into PLA and modify its structure and stability. These findings establish a new foundation for designing tailored synthesis methods for specific applications, providing critical insights into how rare-earth ion doping can be leveraged to enhance the functionality of PLA-based microspheres in radiotherapy and other biomedical applications.

5.2 Materials and methods

Eu-loaded PLLA microspheres were synthesized using an oil-in-water emulsification technique followed by solvent evaporation, based on previously reported protocols [140, 245]. The organic phase consisted of PLLA (Mw $\sim$ 84 kDa) prepared via hot extrusion (180°C) from bio-produced L-isomer (200 mg) and europium acetylacetonate dihydrate ($Eu(acac)_3(H_2O)_2$) (200 mg). These were dissolved in 10 mL of dichloromethane (DCM, 99%) under stirring at 20°C for 10 minutes until complete dissolution. The aqueous phase was prepared by dissolving 750 mg of polyvinyl alcohol (PVA, Mw $\sim$ 31 kDa, hydrolysis degree = 88%) in 75 mL of water under continuous stirring at 40°C. After dissolving the PVA, the organic phase was added to the aqueous phase under mechanical stirring at 500 rpm for two hours, allowing DCM evaporation. The temperature of the aqueous phase (T_{emu}) varied between 20 and 80°C. For $T_{\mathrm{emu}} \geq 50°\mathrm{C}$, the organic phase was carefully introduced to minimize foaming, given DCM's boiling point (40°C). After synthesis, the microspheres were allowed to cool to room temperature, washed with water to remove excess PVA, and drop-cast onto $1x1$ cm silicon wafers. These were left for at least 8 hours to ensure complete solvent evaporation.

For degradation kinetics and Eu release studies, microspheres prepared at different T_{emu} values were immersed in PBS (pH 7.4, with 0.05% TWEEN®20) at 25°C for 30 days, to simulate the exact environment inside the human body. Aliquots were periodically extracted, with $t = 0$ corresponding to the moment the microspheres were added to the PBS solution. Batches of Eu-PLLA microspheres were exposed to 100 Gy X-ray irradiation using a W-target X-ray tube (20 kV, 20 mA) to investigate the eventual radiation-induced molecular modifications.

Optical microscopy was employed for size distribution analyses, while scanning electron microscopy (SEM) was used to investigate the microsphere surface and internal structure. Microsphere cross-sections were prepared by embedding them in epoxy resin and cutting them with a lapping machine. Samples were mounted on aluminum stubs with double-sided adhesive carbon tape and vacuum-coated with a thin (few nm) gold layer. Further internal structure information come from micro-computed tomography (micro-CT) analysis operating in microfocus mode. Microspheres embedded in epoxy resin were sealed in a polyimide tube (Ø=1.8 mm) for a 360° scanning.

Europium content within the microspheres was assessed with X-ray fluorescence (XRF) by calculating the integral of the characteristic fluorescence peak at $L\alpha_1$ energy (5.85 keV). To make the spectra comparable, they were normalized to Rayleigh scattering (17.4 keV, corresponding to the $K\alpha$ emission of Mo). Grazing incidence X-ray diffraction (GIXD) measurements were carried out at the SAXS beamline of the Elettra synchrotron in Trieste (λ = 1.54 Å). Profiles were recorded in a q range of 2 to 30 nm^{-1} with a grazing incidence angle of ω=0.5°. Data processing and transformation into reciprocal space were performed with GIDVis software [246]. The crystalline fraction of PLLA was calculated as the ratio of integrated narrow reflections to the total integrated pattern, which included the amorphous halo. *In-situ* crystallization was studied with powder X-ray diffraction (PXRD), collecting data over a 2θ range of 5.0-30.0° of samples mounted on a heating stage under inert nitrogen conditions. Thermal characterization was carried out through differential scanning calorimetry (DSC) measurements.

The structures of individual microspheres were examined using Raman spectroscopy with a 633 nm (HeNe laser) excitation source. The same instrumental setup was used for photoluminescence (PL) analysis of Eu^{3+} emission spectra utilizing a 488 nm (Ar^+ ion) laser. Effects of degradation and irradiation were verified by Fourier transform IR spectroscopy (FTIR) in transmission configuration. The Eu^{3+} first coordination shell was examined through XAS analyses performed at the Italian CRG beamline LISA-BM08 of ESRF, Grenoble, examining the EXAFS signal on the L_3 edge.

The structure of $Eu(acac)_3$ was confirmed using the CCDC database (deposition number 1836424, [247]), which identifies it as having a $P2_1/n$ space group with unit cell parameters $a = 8.348$ Å, $b = 21.881$ Å, and $c = 11.232$ Å, and angles $\alpha = \gamma = 90°$ and $\beta = 100.409°$.

5.3 Results and discussion

Impact of synthesis and treatment on microsphere morphology and europium retention

Figures 5.1a-e display representative SEM images of the synthesized Eu-doped PLLA microspheres prepared via emulsification at varying temperatures, confirming the formation of spherical microparticles with sizes in the range of a few tens of micrometers. A more detailed and statistically robust analysis of the size distribution, based on optical microscopy of wider field-of-view images, is shown in Figures 5.1f-j. These measurements indicate that the average microsphere sizes range from approximately 50 to 70 µm.

Interestingly, the observed size distribution reveals values larger than those typically reported for pure PLLA microspheres synthesized under similar conditions (30-60 µm range) [243]. This suggests that europium incorporation enhances polymer chain aggregation during microsphere formation. Additionally, the mean size of the microspheres appears to be influenced by the emulsification temperature. A gradual increase in mean size is noted as the emulsification temperature (T_{emu}) rises from room temperature to 50 °C, then to the glass transition temperature (around 60 °C), and further up to 80 °C. Higher-resolution SEM images provide further insight into surface morphology. Microspheres prepared at temperatures below the glass transition temperature exhibit compact, smooth surfaces with minimal porosity or surface corrugation (Figure 5.2a). In contrast, those synthesized at or above 60 °C display an increased number of pores and surface irregularities (Figure 5.2b, Figure 5.3). Despite these variations in smoothness and porosity, the microspheres demonstrate significant morphological stability, with no notable changes observed after the degradation treatments (Figures 5.2c,d).

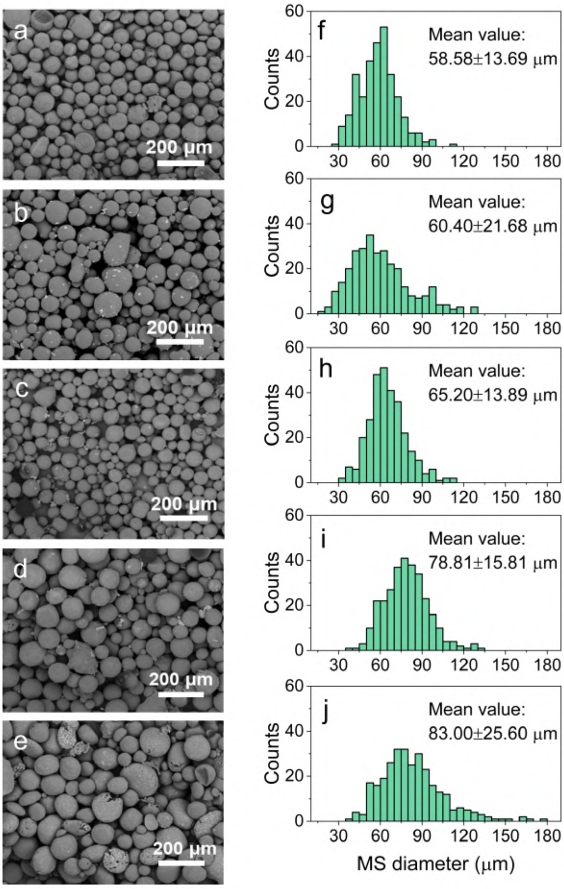

Figure 5.1: (a-e) Representative SEM images of microspheres produced by emulsification at 20, 50, 60, 70, and 80°C, respectively. (f-j) Histograms showing the size distribution of the microsphere batches depicted in (a-e), derived from extensive statistical sampling via optical microscopy.

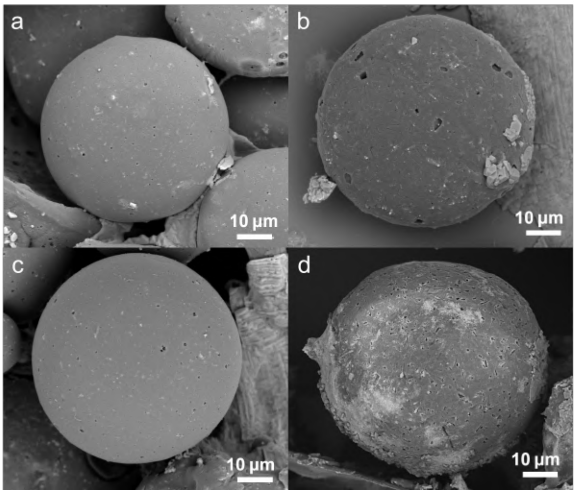

Figure 5.2: (a, b) SEM images of a PLLA microsphere prepared at 20°C and one prepared at 80°C, respectively. (c, d) SEM images of two PLLA microspheres from the batches in (a) and (b), respectively, after 720 hours of treatment in buffer solution.

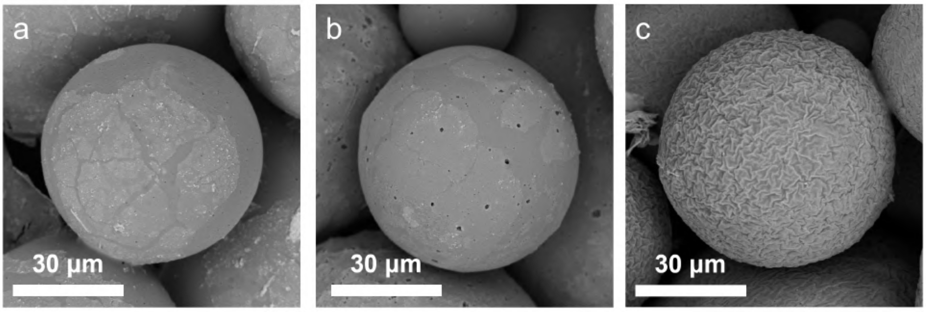

Figure 5.3: SEM images of three representative surface types in microsphere batches synthesized at different temperatures: (a) smooth surface for T_{emu} below T_g, (b) slightly porous surface for T_{emu} above T_g, and (c) corrugated surface for the sample prepared at T_{emu} = 70°C.

The incorporation of europium was quantitatively assessed via X-ray fluorescence (XRF) analysis, which confirms a high yield of Eu integration into the microspheres. Figure 5.4 compares the XRF spectra of Eu-modified PLLA microspheres and a reference sample of Eu(acac)3, normalized to the Rayleigh scattering peak. The characteristic Eu emission lines in the microspheres are slightly weaker (approximately 20% lower intensity) than in the Eu(acac)3 reference, indicating similar Eu concentrations in both systems (34% w/w for Eu(acac)3). Importantly, XRF analysis shows no detectable evidence of Eu release during degradation treatments in buffer solutions up to 4800 hours (Figure 5.5). Furthermore, no Eu was detected in the dried residues of the buffer solutions, confirming the stability of Eu incorporation.

Effects of europium on polymer structure

Figure 5.6a shows a representative XRD pattern of Eu-doped PLLA microspheres (curve 2) compared to a reference Eu-free sample (curve 1) synthesized under identical conditions. The Eu-containing material exhibits a significantly reduced intensity in the broad, unstructured halo at a q vector between 7 and 18 nm^{-1}, indicating a notable reduction in the amorphous fraction, likely due to europium incorporation. This trend is consistent across all Eu-modified microsphere samples compared to pure PLLA microspheres.

Figure 5.7 presents the crystalline fraction calculated from the XRD patterns for the complete set of Eu-doped samples synthesized at varying emulsification temperatures (T_{emu}). Interestingly, the lower limit of the crystalline fraction observed in the Eu-doped samples (data for T_{emu}=60°C) aligns closely with the upper limit for pure PLLA microspheres under similar synthesis conditions (see Chapter 4). Analysis of the peak widths using the Scherrer equation estimates the crystalline domain size to be approximately 30 nm.

Beyond the reduction of the amorphous halo, two additional key differences distinguish the XRD patterns of Eu-modified PLLA microspheres. First, a distinct shift is observed in the primary reflections of the PLLA α-phase at approximately 10, 12, and 13 nm^{-1}, moving towards lower q values by about 0.13 nm^{-1} (inset of Figure 5.6). Sec-

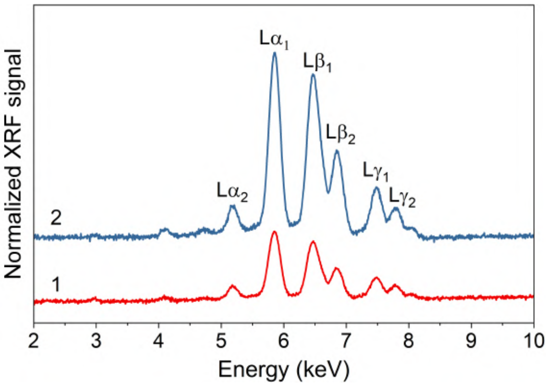

Figure 5.4: XRF spectra highlighting the Eu transitions in a PLLA microsphere sample (curve 1), and in the reference Eu(acac)3 (curve 2), both normalized to the Lα_1 peak of curve 2.

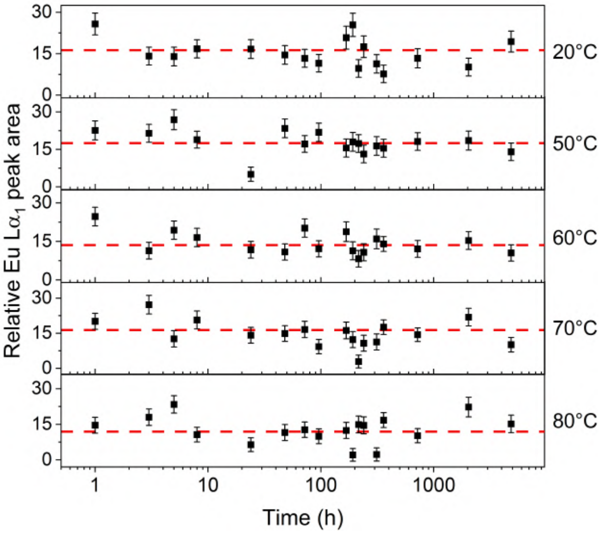

Figure 5.5: Integrated intensity of the Lα_1 XRF peak in PLLA microsphere aliquots measured at various durations in a buffer solution. Red dashed lines indicate the average integrated intensity over time.

ond, all Eu-doped samples exhibit an additional reflection at small q values (5 nm^{-1}), highlighted in Figure 5.6a.

The shift in PLLA reflections suggests that Eu^{3+} ions are incorporated into the crystalline domains of PLLA, modifying the unit cell and slightly expanding the lattice parameters. The low-q reflection, which is absent in the diffraction pattern of pure PLLA, appears unique to the Eu-doped system. Although the origin of this feature remains uncertain, it aligns with similar observations reported in other Eu-doped polymers [237, 240, 248].

The high scattering factor and intensity of the 5 nm^{-1} reflection, comparable to the matrix pattern, imply that it arises from ordered arrangements of Eu ions, which possess high electron density. The low q value corresponds to a large spacing (1.2 nm), likely influenced by steric effects from the chelating organic groups in the Eu coordination shell, as seen in other polymer matrices [237]. Notably, a diffraction peak at a similar position is also present in $\mathrm{Eu(acac)_3}$, where acetylacetone molecules are part of the coordination shell (bottom panel of Figure 5.6b). However, in $\mathrm{Eu(acac)_3}$, the low-q peak is accompanied by additional reflections not observed in Eu-modified PLLA.

This discrepancy suggests that while the 5 nm^{-1} reflection in Eu-modified PLLA supports the presence of Eu ions, the absence of other $\mathrm{Eu(acac)_3}$ diffraction peaks points to a distinct structural organization in the polymer microspheres. Complementary spectroscopic data, discussed in subsequent sections, provide further insights into the local environment of Eu^{3+} ions and their integration into the microsphere structure.

Regardless of the specific mechanism of incorporation, the results in Figure 4b — highlighting significant increases in crystallinity under fixed synthesis conditions — underscore the potential role of europium in shaping the final PLLA structure within the microspheres. Further data presented in the next section delve deeper into this aspect, offering additional evidence and interpretation.

Europium-induced crystallinity and crystallization tendency

The DSC curves shown in Figure 5.8a reveal significant differences between Eu-doped and pure PLLA microspheres. In the Eu-doped batches, cold crystallization is nearly

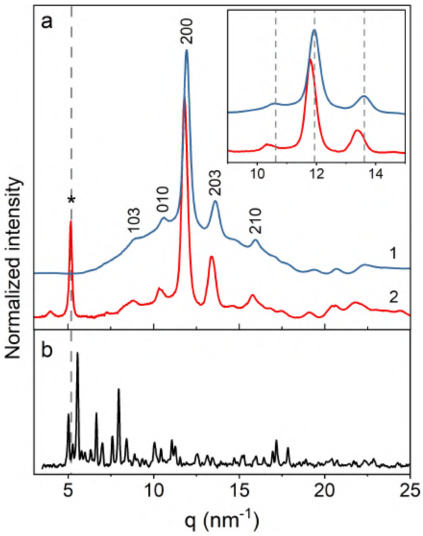

Figure 5.6: (a) XRD patterns of PLLA (curve 1) and Eu-modified PLLA microsphere samples (curve 2) prepared at 20°C. The asterisk marks an additional feature in the Eu-PLLA sample. Inset: magnified view with dashed lines showing the shift in the main reflections. (b) XRD pattern of Eu(acac)$_3$ as a reference.

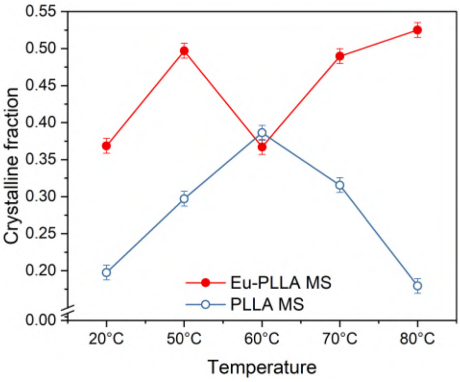

Figure 5.7: Crystalline fraction – from the area of the amorphous halo and the integrated pattern – in samples obtained at different temperatures for Eu-modified microspheres (red curve) and Eu-free microspheres (blue curve).

absent, with only the sample synthesized at 60°C — characterized by the most intense amorphous halo in the diffraction pattern — exhibiting a higher enthalpy compared to the reference Eu-free batch (Figure 5.8b). Moreover, in Eu-modified samples, the cold crystallization temperature (T_{cc}), when present, is shifted to higher values compared to pure PLLA microspheres. Simultaneously, the Eu-doped batches' melting temperature (T_m) decreases from 175°C to approximately 165°C. Importantly, no evidence of melting for segregated Eu(acac)3, which would occur around 130°C (curve 3 in Figure 5), is observed in any Eu-modified batch.

These findings strongly suggest that europium is integrated into the polymer structure of the microspheres, contributing to increased PLLA crystallinity (as corroborated by the XRD analysis in Figure 5.6). This hypothesis is further supported by the absence of any cold crystallization peak, even after cooling from the melt and during subsequent reheating (Figure 5.8a). Unlike the Eu-free microspheres, the Eu-doped polymer demonstrates a pronounced tendency to crystallize directly from the melt.

An alternative interpretation of the absence of exothermic peaks during the cooling ramp—suggesting the formation of a completely rigid amorphous structure after melting—is ruled out by temperature-resolved XRD measurements. Figure 5.9 display XRD patterns of a representative Eu-doped microsphere sample during heating from room temperature to 180 °C (above T_m) in 10 °C increments (Figure 5.9a) and subsequent cooling back to 20 °C (Figure 5.9b).

Three key observations emerge from these data:

1. The primary PLLA diffraction peaks, which disappear above 180°C as expected, reappear immediately upon cooling below T_m. This confirms that the enhanced crystallization propensity from the melt is responsible for the absence of cold crystallization peaks during cooling and reheating in the DSC curves of Figure 5.8.

2. The additional diffraction peak at low q values ($\sim$5 nm^{-1}, corresponding to 7.2° in the 2θ XRD patterns in Figure 5.9) remains unchanged at intermediate temperatures, including 130 °C, the T_m of Eu(acac)3. This peak also persists after

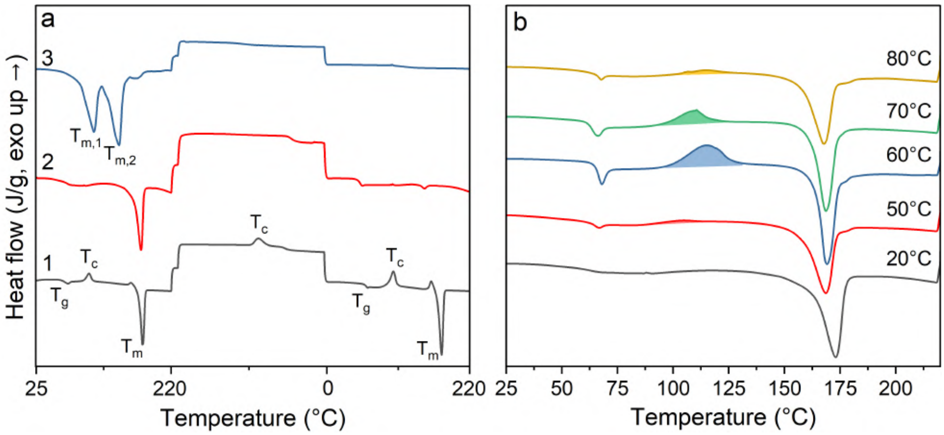

Figure 5.8: (a) DSC curves during the heating ramp from 20 to 220°C, followed by cooling to 0°C and a subsequent heating cycle to 220°C, are shown for Eu-free (curve 1) and Eu-modified (curve 2) PLLA microspheres prepared at 20°C, alongside Eu(acac)3 (curve 3). In Eu(acac)3, an additional endothermic peak appears around 102°C (labelled as $T_{m,1}$), likely due to bound water within the molecule, in addition to the melting peak at 130°C ($T_{m,2}$). (b) DSC curves during the first heating cycle for Eu-modified microspheres prepared at various T_{emu}. The shaded regions represent the enthalpy of cold crystallization.

heating to 180 °C and reappears during cooling, alongside the recrystallization of PLLA from the melt.

3. The stability of this additional diffraction peak suggests that it originates from ordered domains distinct from Eu(acac)3. These domains are thermally more stable than both Eu(acac)3 and Eu-free PLLA, surviving even at elevated temperatures.

These results indicate that the ordered domains associated with europium incorporation act as nucleation sites, promoting crystallization from the amorphous melt at 180 °C. This behavior explains the absence of cold crystallization peaks in the DSC curves of Eu-doped PLLA microspheres, contrasting sharply with the results for Eu-free PLLA microspheres.

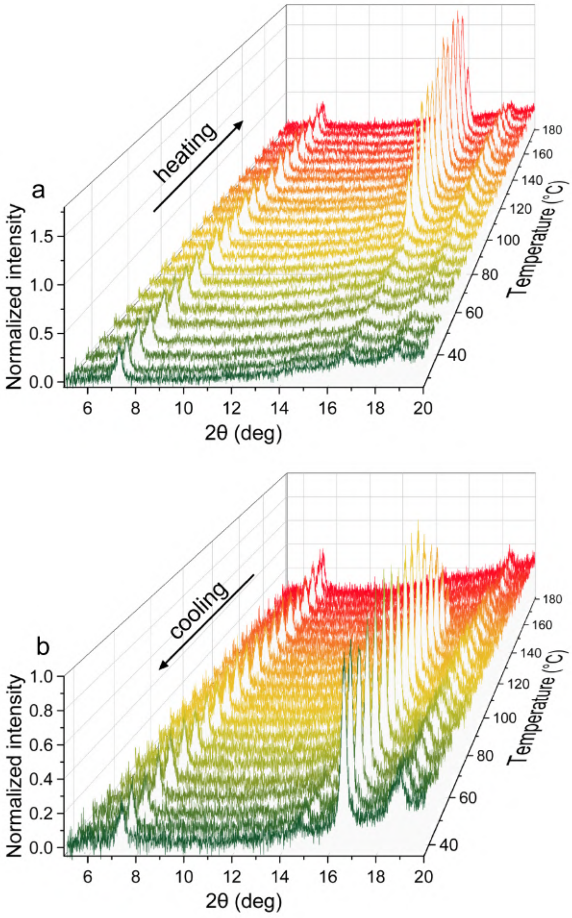

Figure 5.9: XRD patterns of Eu-modified PLLA microspheres prepared at 20°C, recorded at various temperatures: (a) during heating from room temperature to 180°C and (b) during cooling from 180°C in 10°C increments.

Distribution of europium-modified domains

The XRD detection of an Eu-modified structure persisting even after the melting of PLLA suggests the formation of Eu-rich regions within the microspheres, surrounded by an Eu-poor PLLA matrix. Supporting evidence for this phenomenon is provided by SEM analysis of microsphere cross-sections (Figure 5.10a, b) and micro-CT imaging of diluted microsphere dispersions (Figure 5.10c, d). These analyses offer valuable insights into the micromorphology of europium distribution. Both SEM and micro-CT data reveal the presence of localized bright zones, which result from enhanced electron or X-ray scattering, and they are not present in Eu-free microsphere samples (Figure 5.10a, c). These zones correspond to regions of significantly higher density within the otherwise compact polymer matrix, attributable to areas of Eu incorporation. Importantly, these high-density regions are consistently observed to be distributed within the microspheres rather than on their surfaces or at their inner cores. The 360° micro-CT scans confirm that these dense regions are situated just beneath the microsphere surfaces across the analyzed ensemble. This raises a critical question: how is europium incorporated into these regions? The subsequent sections delve into this question through photoluminescence spectroscopy of the embedded Eu^{3+} ions and phonon spectrum analysis of the Eu-modified microspheres. These investigations aim to shed light on the structures and local environments created by the presence of Eu ions.

Spectroscopic insights into europium incorporation in microspheres

The photoluminescence (PL) spectrum of the f-f transitions of Eu^{3+} ions serves as a probe of their immediate environment, providing insights into the first coordination shell and highlighting any deviations from the parent molecular cage in $Eu(acac)_3$. Figure 8 illustrates the PL spectrum for the first three transitions, ${}^5D_0 \rightarrow {}^7F_J$ (with $J = 0, 1, 2$), excited at 488 nm, in a representative sample of Eu-modified PLLA microspheres (Figure 5.11a) and in $Eu(acac)_3$ under identical conditions (Figure 5.11b). The comparison reveals notable differences in the emissions' relative intensities and shapes, indicating significant changes in the symmetry and strength of the electrostatic field

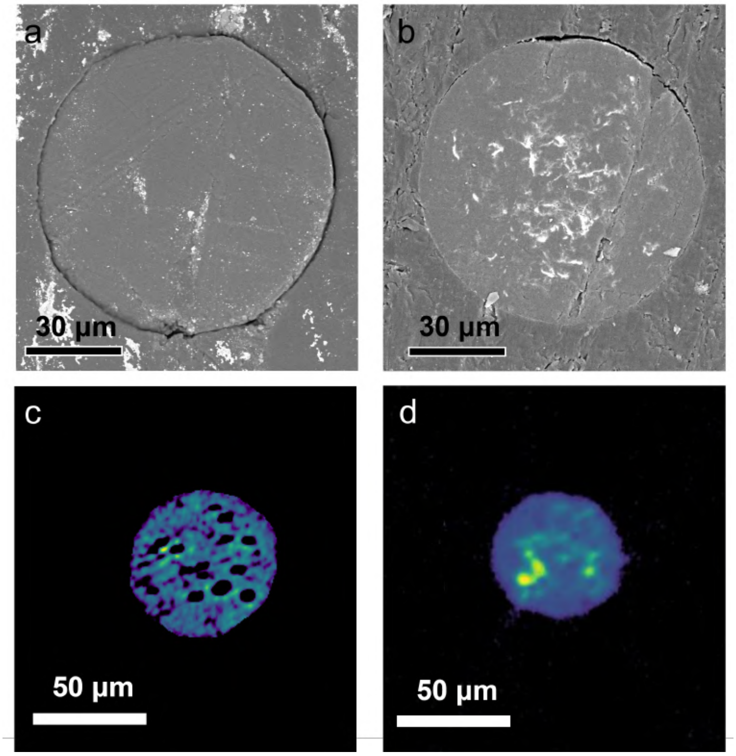

Figure 5.10: SEM and micro-CT images of representative sections of Eu-free PLLA microspheres (a, c) and Eu-modified microspheres (b, d). The bright areas correspond to the presence of europium.

produced by the ligands in the first coordination shell of the Eu^{3+} ions. A complete overview of the europium luminescence spectrum is presented in Appendix B.

The emission band at $\sim$ 595 nm, arising from the magnetic dipole transition $^5D_0 \rightarrow {}^7F_1$, serves as an intensity reference because its integrated intensity is mainly unaffected by the surrounding electrostatic field [249, 250]. In contrast, the narrow peak at $\sim$ 580 nm, corresponding to the non-degenerate $^5D_0 \rightarrow {}^7F_0$ transition, is forbidden under high-symmetry conditions and only becomes detectable under low-symmetry environments due to J-mixing within the $4f^6$ configuration [250]. Its detection here, with an intensity comparable to or exceeding that of the $^5D_0 \to {}^7F_1$ transition, suggests that the Eu^{3+} ions experience a low-symmetry environment in the microspheres.

Additionally, the splitting observed in the $^5D_0 \to {}^7F_0$ peak, such as in the spectrum of Eu(acac)3, does not originate from degenerate energy levels but rather indicates the presence of multiple coordination sites in the system. The band at $\sim$ 615 nm, corresponding to the $^5D_0 \to {}^7F_2$ transition, is the most intense and its shape and intensity are particularly sensitive to changes in symmetry and ligand field strength [249]. A comparison of the PL spectra of Eu^{3+} in PLLA microspheres with those in Eu(acac)3 (Figure 5.11) reveals significant deviations in emission intensities and band shapes. This suggests that the coordination environment of Eu^{3+} in PLLA is distinct, likely differing in local symmetry, coordination number, and ligand distances. Variability in the PL spectra among different microspheres (inset of Figure 5.11a) is minor compared to the differences observed between Eu-modified PLLA and Eu(acac)3, where site-to-site variations are also evident (inset of Figure 5.11b).

Figure 5.12 presents a quantitative analysis of the key spectral features, comparing the normalized integrated intensities of the $^5D_0 \to {}^7F_0$ and $^5D_0 \to {}^7F_2$ transitions relative to the $^5D_0 \to {}^7F_1$ reference transition. This comparison highlights significant differences between Eu sites in PLLA microspheres and those in Eu(acac)3, with the variations among microspheres being relatively small, as shown by the error bars in Figure 5.12.

These findings suggest that the local ligand field in PLLA microspheres is less effective at inducing J-mixing, as indicated by the smaller relative intensities of both $^5D_0 \to {}^7F_0$ and $^5D_0 \to {}^7F_2$ transitions compared to Eu(acac)3 (Figure 5.12). This implies that Eu^{3+} sites in PLLA are characterized by higher symmetry and/or weaker ligand field strength. The latter may result from an increased mean Eu-O distance or a reduction in the number of coordinating ligands.

One key source of asymmetry in the ligand field of Eu(acac)3 is the presence of two water molecules in its eight-fold coordination shell [247]. Replacing these water molecules with carboxyl groups from PLLA chains could increase local symmetry, re-

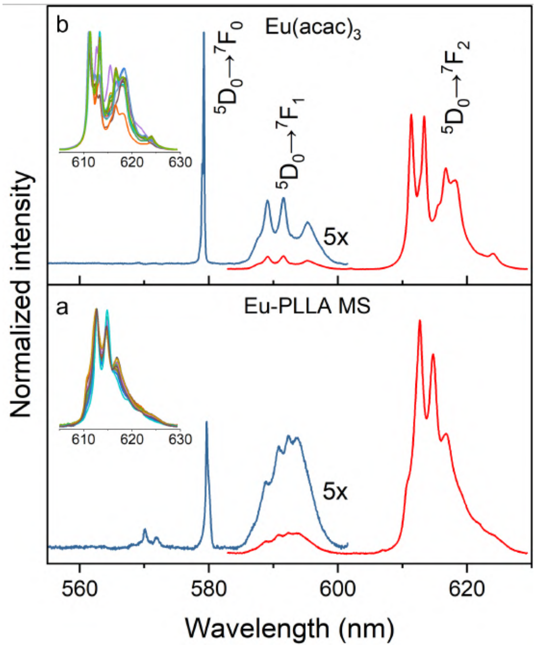

Figure 5.11: (a) PL spectrum of Eu^{3+} ions excited at 488 nm in a representative PLLA microsphere prepared at 20°C, recorded in the 555–630 nm range. Inset: spectral envelope obtained from multiple microspheres within the same batch under similar conditions. (b) PL spectrum as in (a), but for a powdered sample of Eu(acac)3. Inset: spectra recorded at different points of the sample. The corresponding Eu^{3+} transitions are labeled.

ducing J-mixing as indicated by the data in Figure 5.12. Additionally, the weaker ligand field in PLLA may stem from a larger mean Eu-O distance, as the average spacing between carboxyl groups in PLLA chains ($\sim$ 0.293 nm) is slightly greater than that in Eu(acac)3 ($\sim$ 0.278 nm) [85, 247].

The following section explores Raman and IR spectroscopy, offering further insights into the coordination environment of Eu^{3+} ions in PLLA microspheres. These results reveal molecular structures that are similar to but distinct from Eu(acac)3, reflecting the incorporation of Eu into the polymer matrix.

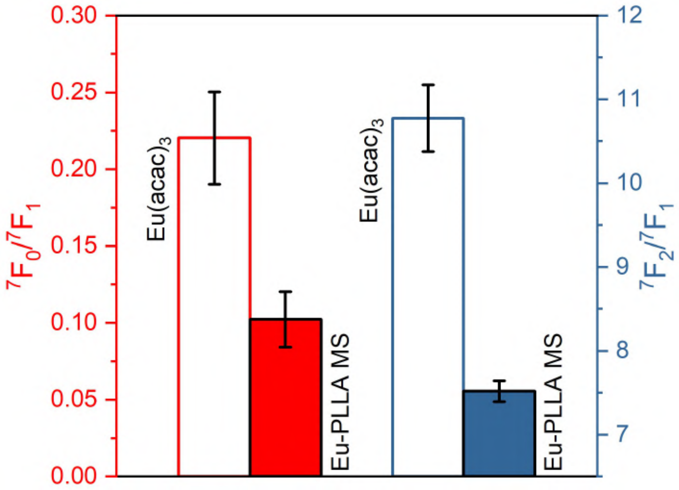

Figure 5.12: Integrated intensities of the PL $^5D_0 \rightarrow {}^7F_0$ and $^5D_0 \rightarrow {}^7F_2$ transitions (left and right axes, respectively) relative to the $^5D_0 \rightarrow {}^7F_1$ transition for Eu^{3+} ions in PLLA microspheres prepared at 20°C (filled bars) and Eu(acac)$_3$ (empty bars). Error bars are the standard deviation from repeated measurements on the same sample.

Europium-induced perturbations in the PLLA phonon spectrum

The Raman spectrum of Eu-modified PLLA microspheres exhibits distinct anomalies compared to pure PLLA, providing insight into how Eu is structurally incorporated within the microspheres. Curve 1 in Figure 5.13 presents the Raman spectrum of a pure PLLA microsphere, serving as a reference, in the spectral range of 200-1800 cm^{-1}. All detected modes correspond to those expected for PLLA [109]. Curves 2 and 3 in the same figure show single-particle Raman spectra of two Eu-modified microspheres, representing two limiting cases: one with minimal spectral alterations (curve 2) and another with more pronounced changes (curve 3) relative to pure PLLA. The most notable differences involve additional phonon modes absent from the vibrational spectrum of PLLA, which align, to some extent, with modes observed in the Raman spectrum of Eu(acac)3 (curve 4 in Figure 5.13).

A weak, structured feature is also visible in the range of 1500-1600 cm^{-1}, attributed to weak photoluminescence from the $^7F_4 \rightarrow {}^5D_0$ transition of Eu^{3+}, excited by the Raman spectrometer's 633 nm laser. This weak emission arises with very low efficiency on the tail of the $^5D_0 \rightarrow {}^7F_2$ transition. The attribution is confirmed by similar emissions observed (Figure 5.14) when the same microspheres (curves 2 and 3 in Figure 5.13) are excited at 488 nm, with only the laser source changed. Notably, the additional phonon modes in the Raman spectra – not part of the Eu-free PLLA phonon spectrum – are more intense in microspheres where the Eu^{3+} emission at 1500-1600 cm^{-1} is stronger. This observation, corroborated by analyzing numerous microspheres across different batches, suggests that these modes arise from molecular groups closely associated with Eu^{3+} incorporation into the microspheres.

A comparison with the Raman spectrum of Eu(acac)$_3$ indicates that the additional modes in Eu-modified PLLA microspheres likely originate from three main types of molecular groups, as inferred from similar spectral features in Eu(acac)$_3$ [251, 252]. The first group includes Eu-O units and chelating C=O groups, with stretching modes potentially contributing to the spectral features at 411 and 946 cm^{-1}. The second group comprises CH$_3$ groups, whose in-plane and out-of-plane deformation modes may correspond to peaks at 570, 1273, and 1369 cm^{-1}. Finally, Eu-(O=C)$_2$ coordination rings, analogous to those in Eu(acac)$_3$, likely contribute to the deformation mode near 668 cm^{-1}, possibly with additional contributions from C-CH$_3$ stretching.

Notably, while many of these modes align with those in Eu(acac)$_3$, some exhibit measurable shifts (e.g., the modes at 668 and 1273 cm^{-1}, each shifted by approximately 8 cm^{-1}) or are entirely absent (e.g., Eu(acac)$_3$ modes at 1020 and 1193 cm^{-1}). These discrepancies suggest that Eu incorporation in the microspheres does not occur through the simple embedding of Eu(acac)$_3$ molecular units or larger segregated Eu(acac)$_3$ domains. Instead, the coordination of Eu^{3+} ions undergoes modifications, as also indicated by the photoluminescence spectroscopy results (Figures 5.11 and 5.12). The interaction with, or involvement of, PLLA chains appears to play a role in the incorporation process.

This conclusion is supported by the near-complete disappearance of vibrational fin-

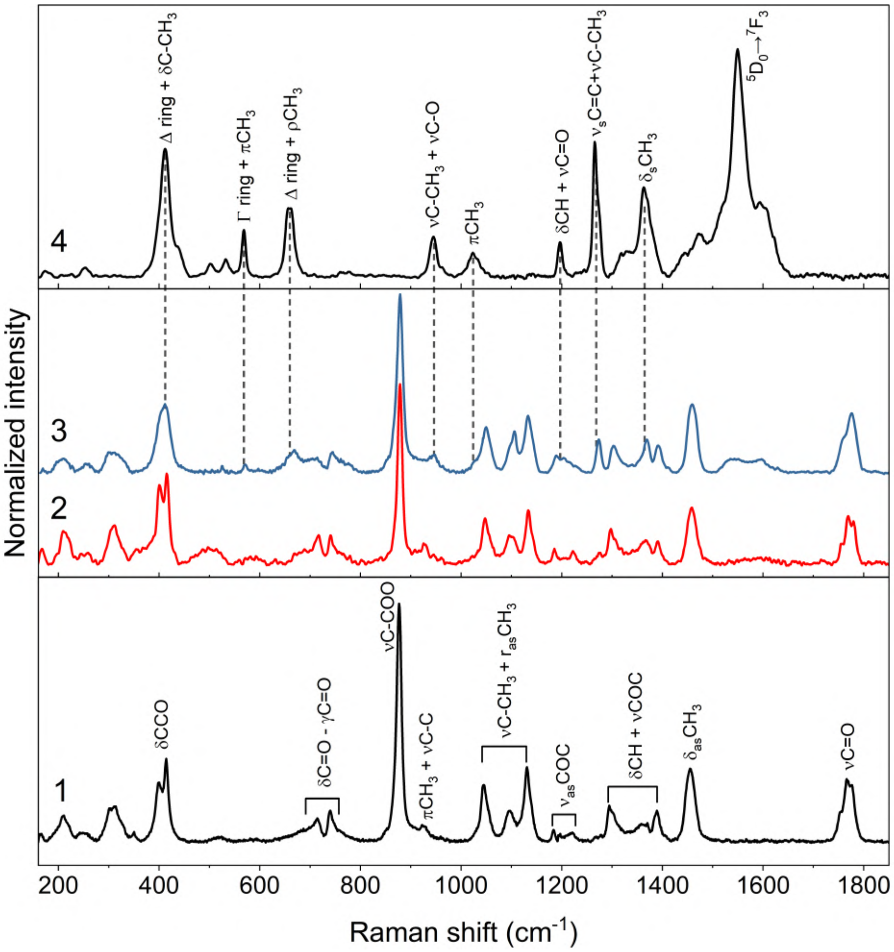

Figure 5.13: Raman spectra of Eu-free PLLA microspheres (curve 1) and Eu-modified PLLA microspheres with low and high Eu content (curves 2 and 3, respectively), qualitatively monitored by the intensity of the Eu^{3+} $^5D_0 \rightarrow {}^7F_4$ transition excited at 633 nm, appearing near an apparent Raman shift of ~1600 cm^{-1}. Dashed vertical lines indicate the positions of the main phonon modes in the spectrum of Eu(acac)3 (curve 4). Phonon mode assignments for molecular groups in PLLA and Eu(acac)3 are annotated with curves 1 and 4, respectively.

gerprints associated with alkene CH groups (olefinic CH), a hallmark of the Eu(acac)$_3$ molecule but absent in PLLA. One such fingerprint is the narrow peak at 1193 cm^{-1} in the Raman spectrum of Eu(acac)$_3$ (curve 4 in Figure 5.13), which arises from an olefinic CH bending mode [251, 253]. The absence of this feature in the Raman spectra of Eu-modified PLLA microspheres supports the hypothesis that alkene CH groups are eliminated during Eu incorporation.

Further evidence comes from the FTIR spectra of Eu-containing PLLA microspheres (curve 1 in Figure 5.15), which lack the olefinic CH stretching mode at 3075 cm^{-1} observed in Eu(acac)$_3$ (curve 2 in Figure 11) [251, 253]. Additionally, the spectral region around 2900-3000 cm^{-1}, corresponding to ethyl and methyl stretching modes, differs significantly from that of Eu(acac)$_3$, notably lacking the CH$_3$ stretching mode at 2925 cm^{-1}. These findings collectively suggest that Eu incorporation into PLLA microspheres does not involve direct embedding of Eu(acac)$_3$ but results in structural modifications to Eu coordination within the polymeric matrix.

The influence of PLLA chains on the Eu^{3+} coordination shell

All spectroscopic results—PL, Raman, and FTIR spectra—point to a common conclusion: Eu^{3+} ions enter PLLA microspheres, forming a coordination environment distinct from that in the precursor compound, Eu(acac)$_3$. Specifically, PL spectra reveal that the coordination shell of Eu^{3+} in PLLA exhibits lower asymmetry and/or a weaker ligand field than Eu(acac)$_3$. Moreover, FTIR spectroscopy shows the absence of key vibrational features of the Eu(acac)$_3$ molecule, ruling out the direct embedding of intact precursor molecules or forming large segregated domains of the precursor.

However, additional molecular groups accompany the incorporation of Eu^{3+} ions into PLLA, as indicated by the appearance of extra vibrational modes in the Raman spectrum. These modes are similar to those associated with Eu coordination in Eu(acac)$_3$. Notably, the molecular groups responsible for these modes are compatible with both modified (acac) fragments and components of PLLA chains. Both systems can potentially form bonds with Eu^{3+} through C=O chelating groups [174], resulting in rings connected to a backbone containing CH$_3$ groups, as shown in Figure 5.16. In this case,

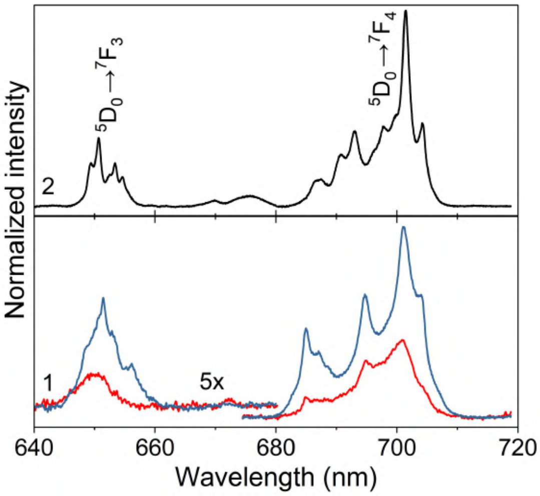

Figure 5.14: Comparison of single-particle PL spectra (λ_{exc} = 488 nm) in the 640–720 nm range for (1) Eu-modified microspheres, illustrating two extreme cases with faint (red curve) and pronounced (blue curve) $^5D_0 \rightarrow {}^7F_3$ and $^5D_0 \rightarrow {}^7F_4$ transitions, and (2) Eu(acac)3.

Eu(acac)3 can act as a ”crosslinker” between the polymer chains.

While the direct embedding of unmodified Eu(acac)3 molecules can be excluded, the spectroscopic data support the formation of Eu^{3+} coordination environments that involve interactions with modified (acac) groups and/or chelating groups along the PLLA chains. This type of coordination, formed through interactions between ion complexes and molecular chains, has been observed in other systems, including those involving polymers prepared with Eu(acac)3 [237–241, 254, 255].

In this case, the interaction between Eu^{3+} and PLLA chains likely arises from two main factors. First, PLLA itself has chelating properties through its carboxyl groups, even though PLA is not typically used as a chelating agent due to the superior chelation capabilities of other molecules. Nevertheless, PLA’s chelating ability is utilized in some applications, such as in food and agriculture, where PLA can act as a natural chelating agent for metal elements in mineral components [256]. The second factor is the difference in the acid dissociation constants (pKa values) between acetylacetone (pKa $\sim$ 9)

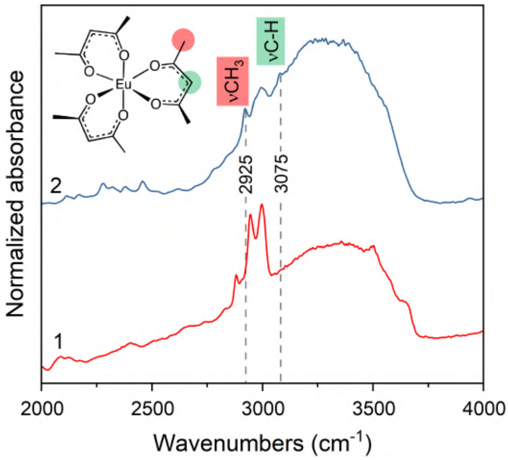

Figure 5.15: Infrared absorption spectra in the region of C–H and O–H stretching modes for Eu-modified PLLA microspheres (curve 1) and Eu(acac)3 (curve 2). Dashed lines at 2925 and 3075 cm^{-1} indicate the modes associated with specific groups in the Eu(acac)3 molecular structure (highlighted in the inset schematic).

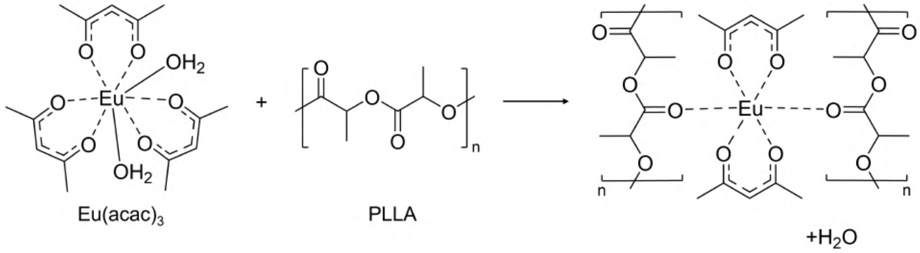

Figure 5.16: Possible mechanism reaction between Eu(acac)3 and PLLA during the formation of microspheres, with the interaction of polymer carbonyl group with one of the carbonyl groups of (acac).

[257] and poly(lactic acid) (pKa $\sim$ 4) [258]. This difference makes it likely that Eu^{3+} ions form coordination bonds with PLLA chains during the emulsification process, where PLLA chains and $Eu(acac)_3$ molecules are fully dissolved in the organic solution and ready to interact in the water phase. During emulsification, the (acac) groups can be partially displaced by Eu^{3+} ions in favor of new bonds with the carboxyl groups of PLLA.

On the other hand, XAS measurements in the EXAFS region, comparing a representative sample of Eu-containing microspheres with $Eu(acac)_3$, confirm that their structures are nearly identical, indicating a similar environment with the number and nature of neighbors (Figure 5.17a, b). From the intensity and frequencies of the oscillations calculated in the k-range 3–10, with a k-weight of 2, a first-shell neighbor is observed, with a peak at 1.93 Å for $Eu(acac)_3$ and 1.97 Å for Eu^{3+} in microspheres, likely corresponding to oxygen. No additional shells are detected, possibly due to increased structural disorder. The fit of the first shell, performed using the Artemis package [259], confirmed that, while the number of neighbors is comparable to the reference, the bond length is longer, likely due to steric hindrance caused by the substitution of a single oxygen atom with an (acac) ligand. However, the discrepancy between the obtained values is minimal, making it challenging to confirm an increase in bond length definitively. Analyzing the second coordination shell would be necessary to validate this hypothesis, but the presence of polymer chains complicates obtaining reliable results.

Impact of Eu-PLLA coordination on polymer structure and structural stability

Based on the spectroscopic results and XRD data discussed above, it can be concluded that Eu^{3+} ions in PLLA form coordination environments that involve not only (acac) molecules but also carboxyl groups along the PLLA chains. Consequently, the Eu^{3+} ions can act as bridges between two or more PLLA chains, creating stable structures where sequences of heavy ions are periodically spaced, with the periodicity governed by the arrangement of carboxyl groups along the PLLA chain. This behavior resemples structures observed in other rare-earth-containing polymers [237, 238, 241]. This hy-

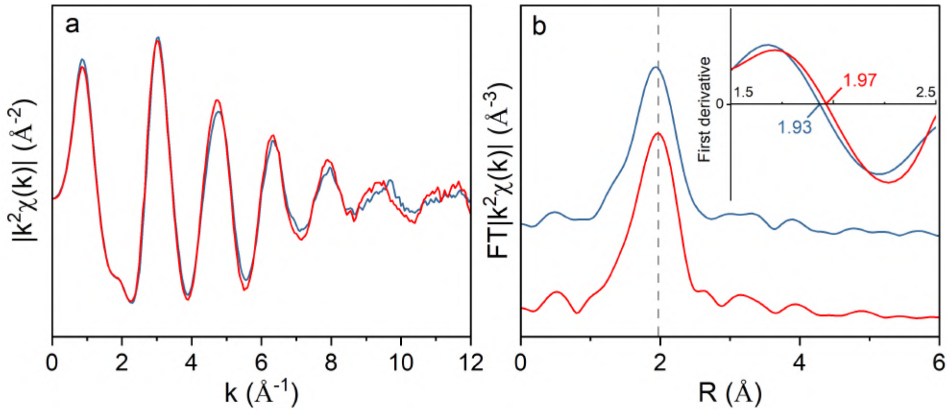

Figure 5.17: (a) EXAFS region of Eu(acac)3 (blue curve) and a representative sample of Eu-containing microspheres (red curve). (b) Fourier Transform of the spectra reported in (a) as a function of the distance. Inset: first derivative of the FT-spectra, where the peak value is indicated.

pothesis is supported by the XRD patterns shown in Figure 5.6a. Specifically, the isolated diffraction peak at approximately 5 nm^{-1} and the shift of the main PLLA diffraction peaks at about 12 and 14 nm^{-1} towards smaller values are consistent with intercalated Eu^{3+} bridges between chains, which slightly expand the unit cell, particularly in the (100) direction.

Importantly, the dissolution of Eu(acac)3 and the formation of O-Eu-O bridges, which replace the interchain hydrogen bonds, can also explain other distinctive features of Eu-modified PLLA microspheres observed in temperature-dependent XRD and DSC measurements. For instance, as shown in Figure 5.9, the single small-angle XRD reflection at around 5 nm^{-1} indicates the presence of low-dimensional, chain-like periodic domains that exhibit enhanced thermal stability compared to pure PLLA. This result is consistent with the formation of structures where a few PLLA chains are held together by O-Eu-O bridges from Eu coordination shells, substituting the less thermally stable interchain hydrogen bonds in pure PLLA. Additionally, the presence of aligned PLLA chains stabilized by Eu coordination shells could also act as crystallization agents, promoting higher crystallinity within the microspheres, both during emulsification and melt crystallization, as confirmed by the experimental data in Figures 5.6b and 5.9. Furthermore, as observed from thermogravimetric analysis (TGA) of Eu-modified microspheres in Figure 5.18, the degradation temperature (approximately 250°C) is significantly lower than that of Eu-free microspheres (approximately 350°C), indicating thermal stability lower than that of nondoped polymeric samples. This variation is most likely attributable to the presence of europium within the structure, as confirmed by the comparison with Eu(acac)3 taken as a reference, which shows a similar weight loss around 250°C. Moreover, the TGA data of the Eu-PLLA complex show the absence of the loss mass event in the range 90-130°C, present in Eu(acac)3, suggesting that the interaction between Eu^{3+} and the polymer occurs via replacement of the water molecules in the coordination compound [260]. The structural stability of Eu-modified PLLA microspheres contributes to the observations in Figure 5.2 and Figure 5.5b, where both the morphological stability of the microspheres and the effective retention of lanthanide ions in buffer solution over extended periods are demonstrated.

This stability can be further analyzed through spectroscopic monitoring of changes in the Eu^{3+} photoluminescence (PL) properties over time in the buffer solution. The results, shown in Figure 5.19, also compare data from microsphere batches prepared at different emulsification temperatures. Most variations observed in degradation time are within the statistical uncertainty, as indicated by the dispersion of values within each sample. This applies to both the relative integrated intensity and the broadening of the Eu^{3+} emission bands. However, in some cases, changes in the relative integrated intensity of the ${}^5D_0 \rightarrow {}^7F_2$ and ${}^5D_0 \rightarrow {}^7F_0$ transitions are noticeable in the early stages of treatment in the buffer solution, with no further significant effects after prolonged exposure. Interestingly, the microsphere batches that show this initial decrease in intensity are those prepared at temperatures comparable to or higher than the glass transition temperature (T_{emu} ranging from 60 to 80°C). However, this effect does not coincide with significant changes in the bandwidth of the ${}^5D_0 \rightarrow {}^7F_2$ emission (Figure 5.19).

The initial change in relative emission intensity suggests a shift in the branching ratio between the different radiative decay channels of the Eu^{3+} ions. This implies changes

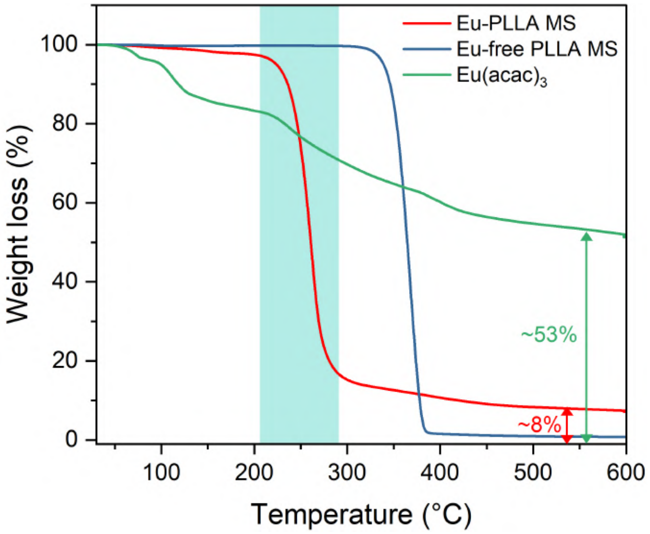

Figure 5.18: Comparison of TGA curves from 25 to 600°C of: Eu-modified PLLA sample (red curve), Eu-free sample (blue curve), and Eu(acac)$_3$ as a reference. The shaded region corresponds to the temperature range at which the main decomposition of Eu(acac)$_3$ occurs. The residual weights of Eu_2O_3 at the end of the measurement for Eu(acac)$_3$ and Eu-modified samples are 53% and 8%, respectively.

in the symmetry and/or polarizability of the Eu^{3+} ion environment, possibly due to structural modifications arising from water molecule adsorption during the buffer solution treatment. Water adsorption could alter the emission bands' relative intensities and, to some extent, the overall emitted intensity by activating non-radiative decay pathways. Despite its hydrophobic nature, PLLA can adsorb and diffuse water molecules, which are influenced by surface morphology and porosity. This is supported by SEM images (Figure 5.3), which show slightly higher surface porosity in microspheres prepared at higher temperatures.

Further evidence of hydration is found in the FTIR spectra. Curves 1 and 2 in Figure 5.20a display the infrared spectra of a sample prepared at T_{emu} of 60°C, both before and after treatment in the buffer solution, focusing on the stretching modes of water

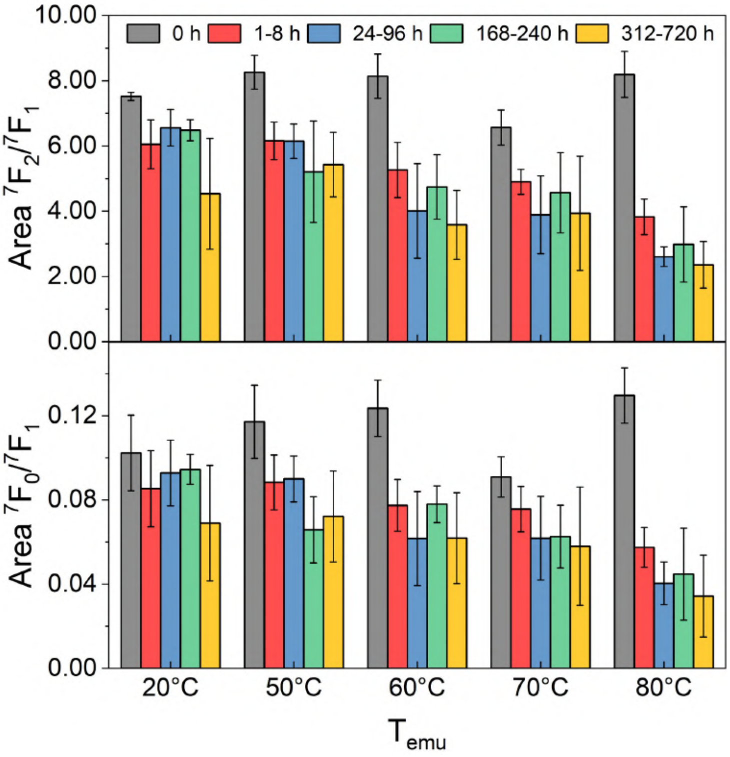

Figure 5.19: Normalized integrated intensity of the $^5D_0 \rightarrow {}^7F_0$ and $^5D_0 \rightarrow {}^7F_2$ transitions relative to the $^5D_0 \rightarrow {}^7F_1$ transition of Eu^{3+} ions in PLLA microspheres, prepared at varying emulsification temperatures and degradation times in buffer solution. Error bars are the standard deviation of the values in the data population.

molecules around 3300 cm^{-1}. A broadband corresponding to water molecules at 3300 cm^{-1} is more prominent after treatment, suggesting the incorporation of H_2O into the microspheres and potential changes to the Eu^{3+} ion environment. Surprisingly, these changes do not significantly affect the broadening of the $^5D_0 \rightarrow {}^7F_2$ emission (Figure 5.19). However, some effects are apparent when examining the shape of the emission band. The inset of Figure 5.20a shows two PL spectra collected before and after 1 hour of buffer solution treatment, revealing a detectable redistribution of emission intensity. Notably, such effects are significant only in samples prepared at 60, 70, and 80°C, where the PL spectra show an intensity reduction and a shape change of the $^5D_0 \rightarrow {}^7F_2$ transition at high degradation times (Figure 5.21). These results indicate that more pronounced changes occur in the ligand field when the sample experiences a slight but measurable decrease in PL intensity after buffer solution treatment, even though the band broadening remains largely unaffected. Additionally, the compact morphology of the microspheres, evident in the SEM images (Figure 5.10a, b), likely prevents extensive water molecule embedding, contributing to the stability of the microsphere structure against hydration. Moreover, no evidence of Eu^{3+} photoluminescence (PL) was observed in the buffer solution after treatment. In particular, no PL signals were detected from water-coordinated Eu^{3+} ions, which are typically characterized by a very weak $^5D_0 \rightarrow^7 F_0$ peak and a notably lower intensity of the $^5D_0 \rightarrow^7 F_2$ band compared to the $^5D_0 \rightarrow^7 F_1$ band [261, 262]. +Figure 5.20b also presents the FTIR spectrum of the same batch (prepared at 60°C) after exposure to an X-ray irradiation test dose of 100 Gy (curve 1), which was used to assess potential radiation-induced molecular damage in the PLLA microsphere structure. No significant molecular modifications are observed in the spectrum. Specifically, no evidence is found of phonon modes (such as those at 2850 and 2925 cm^{-1}, which indicate the transformation of methyl groups to CH_2 groups, or at 3180 and 3390 cm^{-1}, which are associated with hydroxylation of carbonyl groups) that typically arise from the early stages of radiation damage to PLLA at similar X-ray doses (curve 2).

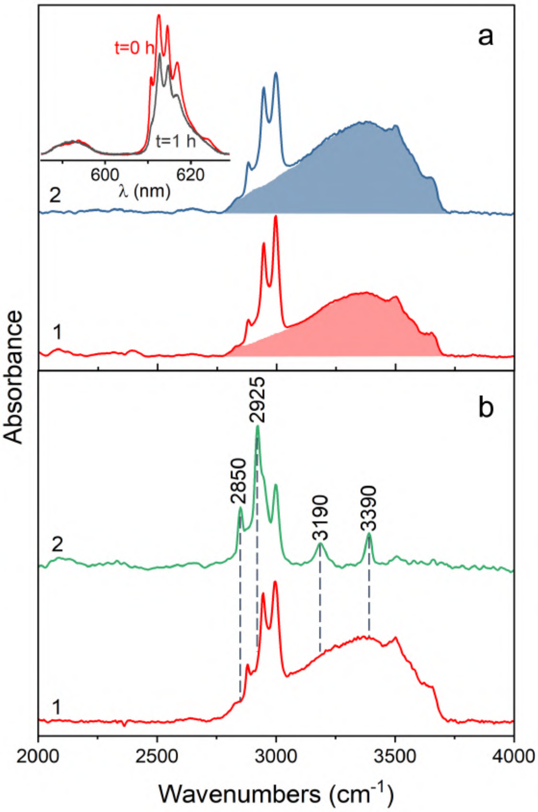

Figure 5.20: (a) Infrared absorption spectra in the C-H and O-H stretching regions for Eu-modified PLLA microspheres prepared at 60°C, shown before (curve 1) and after (curve 2) 720 hours of degradation in buffer solution. Shaded regions indicate the water O-H stretching band. Inset: Photoluminescence (PL) spectra captured before and after 1 hour of degradation in buffer solution. (b) Infrared spectrum of PLLA microspheres prepared at 60°C following exposure to an X-ray dose of 100 Gy (curve 1), compared to the spectrum of a bulk PLLA sample exposed to the same dose (curve 2), highlighting radiation-induced degradation effects (labels on curve 2).

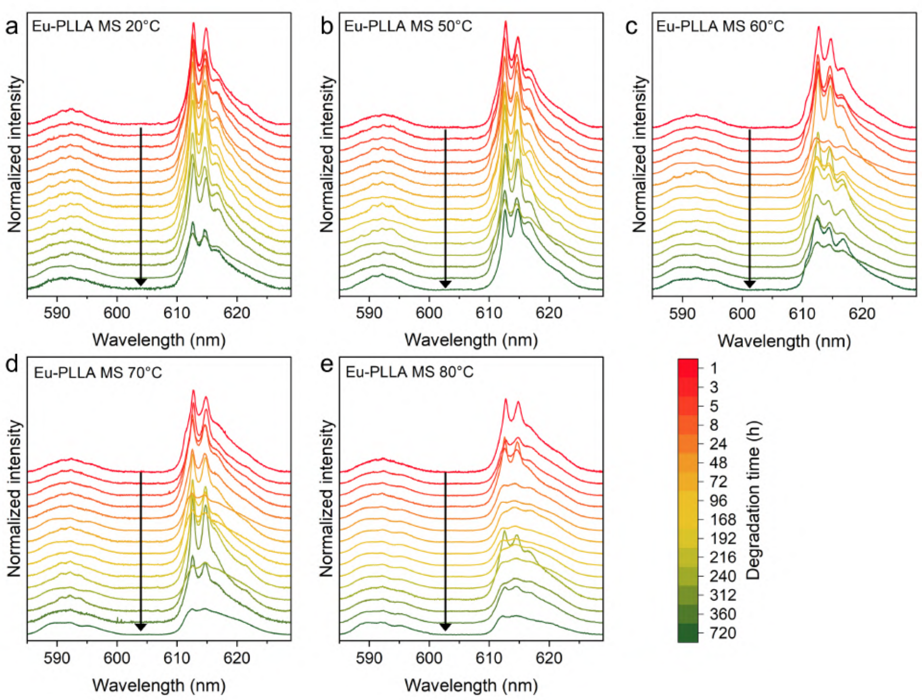

Figure 5.21: Changes in the shape and intensity of the $^5D_0 \rightarrow {}^7F_2$ transition with degradation time for Eu-PLLA microsphere batches prepared at different T_{emu}. All spectra were normalized to the integral of the $^5D_0 \rightarrow {}^7F_1$ transition for comparability. The black arrows indicate the progression of the degradation.

5.4 Conclusions

Incorporating a rare-earth ion such as europium into PLLA microspheres has proven to be a transformative approach for enhancing their structural, thermal, and morphological properties. The collected data — derived from complementary techniques including microscopy, diffractometry, calorimetry, and spectroscopy — offered valuable insights into the mechanisms underlying europium incorporation into microspheres via emulsification.

The integration of Eu^{3+} ions into the polymer matrix forms a coordination shell distinct from that of the precursor compound (supported by PL data), interacting with polymer chains and coordinating with PLLA carboxyl groups, evidenced by spectroscopic analyses. This coordination enables Eu^{3+} ions to act as bridges between PLLA chains, enhancing the polymeric matrix's crystallinity and stability (confirmed by XRD and DSC) and resulting in a compact micro-morphology. The data also demonstrate that the interaction between lanthanide ions and the polymer can be tuned by adjusting the emulsification temperature, allowing control over the matrix's resistance to rapid degradation, structural damage, and ion release.

Furthermore, this research has shown that europium incorporation significantly alters the thermal behavior of PLA microspheres. Suppressed cold crystallization and improved crystallization from the melt highlight the dynamic role of europium in enhancing the material's thermal resilience. This modification not only improves the mechanical stability of the microspheres but also contributes to their resistance to environmental factors such as radiation and prolonged exposure to aqueous media, such as a buffer solution. Notably, the absence of significant europium leaching underlines the system's reliability for applications where the retention of functional species is critical.

These findings underscore the potential of europium-modified PLA microspheres in applications that demand high structural stability, such as medical devices and biocompatible luminescent systems. Thus, they establish a reliable foundation for designing systems tailored to specific applications.

CHAPTER SIX

GENERAL CONCLUSIONS

The research presented in this thesis explores innovative ways to synthesize and characterize poly(lactic acid) (PLA) microspheres as carriers for targeted internal radiotherapy. It addresses critical challenges in current cancer treatments, including limited therapeutic specificity, harmful side effects, accumulation in healthy tissues, and the need for environmental sustainability, thus highlighting the potential of PLA microspheres as versatile carriers for radioisotopes and imaging markers.

In the context of selective internal radiation therapy, this work provides a strong foundation for using PLA microspheres as effective and sustainable carriers of radioisotopes. Compared to traditional materials like glass or resin microspheres, PLA offers several advantages: it is lightweight, biodegradable, and has a density close to human plasma, which helps ensure smooth injection and even distribution in blood vessels. These properties, combined with the ability to encapsulate radioactive isotopes in the matrix securely, make PLA an ideal candidate for targeted therapies that minimize side effects while focusing on tumor detection.

The research emphasizes the importance of controlling PLA's structural and physicochemical properties to improve its performance in biomedical applications. The work highlights how the conformation of the polymer, so if it is crystalline or amorphous, can affect its radiation hardness, a crucial aspect for specific applications like radioembolization.

One of the main breakthroughs in this thesis is the demonstration that small changes in the microsphere preparation — like emulsification temperature — directly influence the polymer's morphology and functional efficiency. Understanding and controlling crystallinity is essential because it directly affects the mechanical stability, degradation rate, and drug or isotope encapsulation capacity of the microspheres. Radiation-induced modifications in PLA further highlight the polymer's ability to maintain structural integrity while exhibiting predictable degradation pathways. These findings are critical for ensuring the controlled release of encapsulated radioisotopes over the desired treatment period, optimizing therapeutic outcomes.

The thesis also identifies areas where the manufacturing techniques can improve, achieving greater consistency in size, encapsulation efficiency, and functionalization. For example, further refinement of the solvent evaporation and emulsification methods could address current limitations related to batch-to-batch variability and scaling up production. Refining these processes will help make PLA microspheres more accessible for clinical use.

A key innovation in this study is the incorporation of europium as Eu^{3+} into PLA microspheres to mimic the presence of a rare-earth ion used for its diagnostic potential. Incorporating europium into the PLA matrix enhances the material's structural and thermal stability. The europium-doped microspheres exhibit unique spectroscopic behaviors that reveal insights into europium-polymer interactions. The ability to control its crystallinity, molecular structure, and degradation behavior allows for the precise customization of microspheres to meet the exact requirements of specific therapies, such as selective internal radiation therapy (SIRT).

Overall, this work lays the foundation for future advancements in PLA-based biomaterials, particularly for applications that require precise control over material properties and functionality. PLA-based systems offer a promising alternative to non-biodegradable materials, particularly in applications where the long-term presence of microspheres in the body is undesirable. The focus on PLA microspheres aligns with a broader shift toward green fabrication processes, where renewable materials and energy-efficient synthesis methods contribute to developing environmentally responsible medical devices. Moreover, integrating europium as a constituent component of the microspheres opens new possibilities for combining therapeutic and diagnostic capabilities within a single platform. By enabling targeted radiation delivery and real-time monitoring, these PLA microspheres have the potential to revolutionize personalized medicine, addressing current limitations in cancer therapy while improving patient safety and treatment efficacy.

In summary, this thesis demonstrates that poly(lactic acid) microspheres represent a versatile, sustainable, and highly functional material system for modern medicine. Through careful synthesis, characterization, and functionalization, PLA microspheres can be tailored to meet the specific requirements of targeted therapies and diagnostics. The findings presented here contribute to the development of innovative materials for selective internal radiation therapy, and a shift toward safer, more effective, and environmentally responsible healthcare solutions. As research advances, PLA microspheres are poised to play a crucial role in shaping the future of personalized medicine and cancer treatments.

APPENDIX
A

CHARACTERIZATION TECHNIQUES

Thermogravimetrical analyses (TGA)

TGA analyses were conducted with a Mettler Toledo TGA/DSC1HT STARe System at a constant gas flow (50 ml min^{-1}). The thermal profile was the following: first cycle from 25 to 600°C with a heating rate of 10°C min^{-1} under nitrogen, second cycle from 600 to 700°C in air flow with a rate 10°C min^{-1}.

Elemental analysis

Elemental analysis of CHNS was conducted using an Elementar VarioMicro-Cube analyzer on both a PLA pellet and a 100 Gy irradiated pellet (approximately 1–2 mg each). The samples were combusted at 1150°C and reduced at 850°C within a measuring chamber. Pure helium gas served as the reference and carrier gas during the analysis. A thermal conductivity detector (TCD) recorded changes in the thermal conductivity of the helium as combustion gases (N_2, CO_2, H_2O, and SO_2) entered the chamber.

Differential Scanning Calorimetry (DSC)

DSC was employed to determine the thermal properties using a DSC-1 system (Mettler Toledo STARe) equipped with a liquid nitrogen low-temperature apparatus. Heat flow was recorded during heating and cooling ramps between 0°C and 220°C at a rate of 10°C $\min^{-1}$ under a nitrogen atmosphere. Calibration of temperature and heat flow was achieved using indium as the standard. The glass transition temperature (T_g) was determined as the midpoint of the step transition in the calorimetric curve.
To verify the absence of PVA residue in the microspheres, the chosen DSC cycle includes two heating cycles from 0 to 300°C interspersed with cooling to 0°C (since the melting temperature of PVA is about 250°C).

Powder X-ray Diffraction (PXRD)

PXRD analyses were performed using a Rigaku powder diffractometer equipped with a Cu-Kα source (40kV, 30mA). PXRD profiles were collected over a 2θ range of 5.0°–40.0°, with a step size of 0.02° and a scan speed of 2.0°$\min^{-1}$. *In-situ* crystallization studies were conducted using a PANalytical Empyrean diffractometer with a Cu-Kα source (40kV, 40mA). Data were collected over a 2θ range of 5.0–30.0° at a scan speed of 2.0°$\min^{-1}$. Diffraction was detected with a 0.1 mm anti-scatter slit/0.02 rad Soller slit configuration and a PANalytical PIXcel detector. The diffractometer comprises a DHS 900 heating stage (Anton Paar) under inert nitrogen conditions.
The mean size of the crystallite domains (D) was calculated using the Scherrer equation $D = K\lambda/\beta cos(\theta)$, where K is the shape factor (typically 0.9), λ is the X-ray wavelength, β is the line broadening at the FWHM, and θ is the Bragg angle.

Grazing Incidence X-ray Diffraction (GIXD)

GIXD measurements were carried out at the SAXS beamline of the Elettra synchrotron in Trieste, employing a 1.54 $\mathring{A}$ wavelength and silver behenate as a calibrant. Diffraction was detected using a Pilatus 2M detector positioned 225 mm from the sample. Profiles were recorded in a q range of 2 to 30 nm^{-1} with a grazing incidence angle of ω=0.5°. Data processing and transformation into reciprocal space were performed with GIDVis software [246].

Raman Spectroscopy and Photoluminescence (PL)

Raman and PL measurements were performed using the same instrumental setup on a Labram Horiba Jobin-Yvon spectrometer equipped with both a 632.8nm HeNe (for Raman) and a 488 nm Ar$^+$ (for PL) laser sources. The scattered light was collected using 10x and 20x objectives mounted on an Olympus BX40 microscope head, and the signal was detected with a CCD-Sincerity system (Jobin-Yvon) with a spectral resolution of 1 cm^{-1}.

Fourier Transform IR spectroscopy (FT-IR)

FTIR characterization was performed using a Thermo Fisher Nicolet iN10 infrared microscope (675–4000 cm^{-1}) in transmission and attenuated total reflectance (ATR) configurations. The detection setup consists of a double detector, DTGS (deuterated L-alanine doped triglycine sulphate) and MCT (Mercury Cadmium Telluride), cooled with liquid nitrogen. ATR-FTIR spectra were collected on a gold substrate with a single crystal Ge tip (350 µm diameter). Transmission FTIR spectra were obtained with LED illumination on a 0.5x0.5 cm^2 CVD-deposited diamond substrate.

Nuclear Magnetic Resonance (NMR)

^{1}H NMR spectra were recorded using a Bruker Avance NEO spectrometer operating at 400.13MHz for ^{1}H with a 5mm broadband probe. The NMR tube was prepared with 20 mg of sample dissolved in 5 µL of deuterated chloroform ($CDCl_3$) as a solvent. The obtained spectra were analyzed using the software TopSpin.

Gel Permeation Chromatography (GPC)

Molecular weight distributions were determined by GPC using a Waters 1515 isocratic HPLC pump equipped with a refractive index detector and four Styragel columns. 10 mg of the sample was dissolved in 2 mL of THF, adding 7 µL of toluene, and the chromatograms were recorded with a flow of 1.0 ml min^{-1} at 35°C. Calibration with a polystyrene standard was used to calculate molecular weights.

Optical Microscope

Optical microscope images were acquired using a Leica DM LM microscope equipped with a Leica DFC280 digital color camera and a 10× objective lens. Digital images were analyzed using the program ImageJ to estimate the statistical distribution of microsphere sizes.

Scanning Electron Microscopy (SEM)

SEM images on materials were obtained by using a Thermo Fisher Phenom G6 SEM equipped with a backscattered electrons detector (BSD) operating at 10 kV. Samples were mounted on aluminum stubs with double-sided adhesive carbon tape and coated with a thin Au layer for imaging.

Micro-computed Tomography (micro-CT)

Micro-CT analysis was conducted using a UniTOM HR (Tescan, Czech Republic) operating in microfocus mode. The instrument was set to 50 kV accelerating voltage with 1.3 W target power. Tilt series were acquired at 0.9 µm voxel size over 2286 projections within a 360° range, with each projection using a 1350 ms exposure and four averages. Reconstruction was performed using TESCAN Panthera software, and the data were visualized using ORS Dragonfly software.

X-ray Flourescence (XRF)

X-ray fluorescence (XRF) spectra were obtained with an ARTAX 200 (Bruker) instrument equipped with a molybdenum-anode X-ray tube operating at 40 kV, 600 μA, for a measurement time of 120 sec. Evaluation of europium content in the samples was assessed by calculating the integral of the characteristic fluorescence peak at $L\alpha 1$ energy (5.85 keV). To make the spectra comparable, they were normalized with respect to Rayleigh scattering (17.4 keV, corresponding to the $K\alpha$ emission of Mo).

X-ray Absorption Spectroscopy (XAS)

XAS analyses have been performed at the Italian CRG beamline LISA-BM08 of ESRF [263], Grenoble. The beamline is downstream a bending magnet, whose beam is parallelized with a mirror over the monochromator. For this experiment, the energy of the radiation is chosen with a Si(111) N_2-cooled double crystal monochromator (DCM); the harmonics are then rejected with a second silicon mirror placed after the detector. The beam and transmitted intensities are then measured using two ionization chambers filled with 1 atm of N_2, placed respectively before and after the sample. Europium acetylacetonate and Eu-PLLA MS samples have been pelletized in a 1.5 mm die using 25 mg of sample mixed with 15 mg of cellulose. The samples were then measured in transmission at a temperature of 70K to enhance the EXAFS signal. The XAS spectra collected on the L3 edge have been recorded from 6777 to 6957 eV with a step of 5eV, from 6957 to 7007 with a step of 0.4 eV and until 7834eV with a k-step of 0.05 $\AA$.

APPENDIX

B

PHOTOLUMINESCENCE PROPERTIES OF EU^{3+}

The trivalent europium ion (Eu^{3+}) displays intense red photoluminescence when exposed to UV radiation. This characteristic photoluminescence is observed not only in Eu^{3+} ions doped into crystalline host matrices or glasses but also in europium(III) complexes with organic ligands. These ligands function as antennas, absorbing excitation light and transferring the energy to the higher energy levels of the Eu^{3+} ion, subsequently populating the emitting excited states [249].

In addition to its red luminescence, Eu^{3+} is notable for its narrow transitions in absorption and luminescence spectra—distinctive features recognized since the discovery of the chemical element europium. These transitions' fine structure and relative intensities serve as probes of the local environment surrounding the Eu^{3+} ion. Spectroscopic data can reveal the point group symmetry of the Eu^{3+} site and, in some cases, provide insights into its coordination geometry.

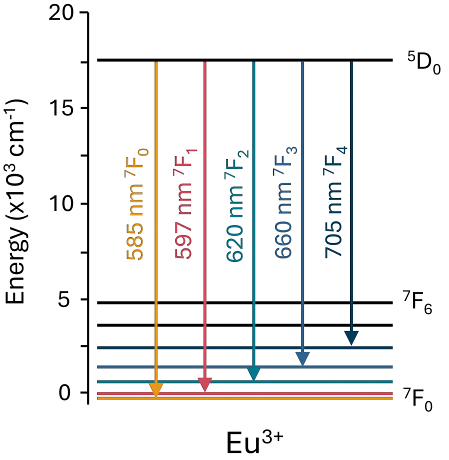

Figure B.1: Energy-level diagram of Eu^{3+} ion with $^5D_0 \to {}^7F_J$ transitions and respective emission wavelength.

Selection rules and Judd-Ofelt theory

The luminescence spectra of europium(III) compounds provide more detailed information than their absorption spectra. Many europium(III) compounds exhibit intense photoluminescence, primarily due to the $^5D_0 \to {}^7F_J$ transitions (J = 0–6) from the $^5D_0$ excited state to the ^7F levels of the ground state. Transitions to the $^7F_5$ and $^7F_6$ levels are often not observed, as they typically fall outside the detection range of standard spectrofluorimeter detectors. Emission from higher excited states such as $^5D_1$ and $^5D_2$ is typically suppressed by non-radiative decay pathways, especially at room temperature [264]. However, these emissions can become observable at cryogenic temperatures or in specific host matrices where phonon interactions are minimized. Such observations provide additional information about the dynamics of excited-state relaxation and energy transfer mechanisms. The main Eu^{3+} transitions from the ground state $^5D_0$ are reported in Fig. B.1.

Most transitions visible in the luminescence spectrum are induced electric dipole

(ED) transitions. These transitions result from the interaction between the lanthanide ion and the electric field vector via an electric dipole involving a linear charge movement. The transitions observed in Eu(III) luminescence are significantly weaker than ordinary electric dipole transitions. They are thus called ”induced” or ”forced” electric dipole transitions rather than conventional ones. The intensities of these ED transitions can be quantitatively described using the Judd–Ofelt theory [265, 266]. In free ions, these transitions are parity-forbidden; however, in a solid matrix, the crystal field effects partially lift this restriction. The crystal field induces a mixing of electronic states, enabling transitions that are otherwise forbidden in isolated ions.

The theory quantitatively models this mixing using three phenomenological parameters, denoted as Ω_λ (where $\lambda = 2, 4, 6$). These parameters reflect the asymmetric nature of the crystal field and are essential for calculating transition probabilities, oscillator strengths, and radiative lifetimes of excited states. These insights are critical for designing and developing photonic devices such as lasers and optical amplifiers. According to Judd-Ofelt theory, electric dipole transitions are parity-forbidden in centrosymmetric environments but become partially allowed when symmetry is broken. This results in deviations from strict selection rules, as crystal-field effects and charge-transfer interactions mix states of different parity. Magnetic dipole transitions, which are less sensitive to symmetry changes, remain allowed in centrosymmetric environments.

Some transitions, such as the $^5D_0 \rightarrow {}^7F_1$ transition, exhibit magnetic dipole (MD) character. Magnetic dipole transitions are allowed, but their intensities are weak and comparable to induced electric dipole transitions. The intensity of a magnetic dipole transition is largely independent of the surrounding environment and can be considered constant to a first approximation.

$^5\mathbf{D_0} \rightarrow {}^7\mathbf{F_0}$ transition

The $^5D_0 \rightarrow {}^7F_0$ transition is strictly forbidden according to the standard Judd–Ofelt theory, as a 0–0 transition is prohibited by the ΔJ selection rule. However, the occurrence of this transition is a well-known example of the breakdown of the selection rules of the Judd–Ofelt theory. A common explanation is that this transition arises due to J-mixing or the mixing of low-lying charge-transfer states into the wavefunctions of the $4f^6$ configuration [267–269]. J-mixing is caused by the crystal-field perturbation, which leads to the mixing of wavefunctions of terms with different J values. After J-mixing, the wavefunction of the $^7F_0$ state also includes contributions from the $J = 2, 4, 6$ states. These two mechanisms are not independent; it has been observed that there is an inverse relationship between the energy of the transfer state and the crystal-field strength: lower energies for the charge-transfer states result in stronger crystal-field effects, which in turn enhance J-mixing.

The $^5D_0 \rightarrow {}^7F_0$ transition is one of the narrowest 4f–4f transitions ever observed. Its occurrence indicates that the Eu^{3+} ion occupies a site with C_{nv}, C_n, or C_s symmetry. This can be understood by considering the selection rules. A $J = 0$ state must transform as the identity representation of the point symmetry group, meaning some components of the electric dipole operator must also transform as the identity representation. This condition is met for point groups where the crystal-field potential contains C_1 spherical harmonics, such as the C_{nv}, C_n, and C_s symmetry groups.

In most europium(III) spectra, the $^5D_0 \rightarrow {}^7F_0$ transition is weak, even for complexes with C_{nv}, C_n, or C_s symmetry. However, this transition is unusually intense in the β-diketonate complex with the Eu^{3+} ion at a site with C_3 symmetry [270]. In the luminescence spectrum of this complex, the $^5D_0 \rightarrow {}^7F_0$ transition has a higher peak height than the $^5D_0 \rightarrow {}^7F_1$ transition. However, the latter has the largest integrated peak area due to the extreme narrowness of the $^5D_0 \rightarrow {}^7F_0$ transition.

The $^5D_0 \rightarrow {}^7F_0$ transition is also helpful in detecting the presence of non-equivalent sites in a host crystal or for determining the number of different europium(III) species in solution, as only one peak is expected for a single site or species due to the non-degeneracy of the $^7F_0$ and $^5D_0$ levels. The observation of multiple peaks in the spectroscopic region where the $^5D_0 \rightarrow {}^7F_0$ transition is expected indicates the presence of more than one site or species, but it does not provide information on the exact number of sites or species, as sites or species with symmetry other than C_{nv}, C_n, or C_s do not give an observable $^5D_0 \rightarrow {}^7F_0$ transition. If the structural differences between two sites are small, the energy differences between the peaks in the $^5D_0 \rightarrow {}^7F_0$ region will also be small. The presence of more than one site will be revealed by an asymmetric shape or a shoulder in the $^5D_0 \rightarrow {}^7F_0$ line. However, the presence of two distinct geometrical isomers in a crystal structure can lead to a significant energy difference between the transitions in the $^5D_0 \rightarrow {}^7F_0$ region.

$^5\mathbf{D_0} \rightarrow {}^7\mathbf{F_1}$ transition

The $^5D_0 \rightarrow {}^7F_1$ transition is a magnetic dipole (MD) transition. While the intensity of a magnetic dipole transition is largely independent of the Eu^{3+} ion's environment, it is important to note that the invariability of the intensity of the $^5D_0 \rightarrow {}^7F_1$ transition applies only to the total integrated intensity of this transition, not to the individual intensities of the crystal-field components [271]. The total intensity of the $^5D_0 \rightarrow {}^7F_1$ transition can be influenced by J-mixing. Nevertheless, this transition is often considered to have a constant intensity, and it is used to calibrate the intensity of europium(III) luminescence spectra.

The $^5D_0 \rightarrow {}^7F_1$ transition directly reflects the crystal-field splitting of the $^7F_1$ level. The $^7F_1$ level remains unsplit in cubic or icosahedral crystal fields. The $^7F_1$ level splits into a non-degenerate and a twofold degenerate crystal-field level in hexagonal, tetragonal, and trigonal crystal fields. In orthorhombic or lower symmetries, the complete removal of crystal-field degeneracies results in three sublevels for $^7F_1$.

The $^5D_0 \rightarrow {}^7F_1$ transition is the most intense in the spectra of solids with a centrosymmetric crystal structure. The presence of more than three lines for the $^5D_0 \rightarrow {}^7F_1$ transition suggests the presence of multiple non-equivalent sites for the Eu^{3+} ion. This transition can be used to detect multiple sites, particularly if the $^5D_0 \rightarrow {}^7F_0$ transition is forbidden. However, caution must be taken to avoid confusing vibronic transitions with purely electronic transitions.

$^5D_0 \rightarrow {}^7F_2$ transition

The $^5D_0 \rightarrow {}^7F_2$ transition is referred to as a "hypersensitive transition," meaning that its intensity is significantly more influenced by the local symmetry of the Eu^{3+} ion and the nature of the ligands compared to the intensities of other electric dipole (ED) transitions. Hypersensitive transitions follow the selection rules $|\Delta S| = 0$, $|\Delta L| \leq 2$, and $|\Delta J| \leq 2$. The intensity of the $^5D_0 \rightarrow {}^7F_2$ transition is often used as an indicator of the asymmetry of the Eu^{3+} site [272]. Significant variations are observed in the intensity of this transition depending on the type of europium(III) compound. Europium(III) *β*-diketonate complexes, including both Lewis base adducts of tris complexes and tetrakis complexes, typically exhibit a very intense hypersensitive $^5D_0 \rightarrow {}^7F_2$ transition. It is not uncommon for the $^5D_0 \rightarrow {}^7F_2$ transition to be up to 10 times more intense than the $^5D_0 \rightarrow {}^7F_1$ transition in these types of complexes. The $^5D_0 \rightarrow {}^7F_2$ transition often dominates the spectrum. While the high intensity is typically attributed to the low symmetry of the Eu^{3+} ion, it is more accurate to consider the high polarizability of the chelating *β*-diketonate ligands as the mechanism responsible for the intensity enhancement.

$^5D_0 \rightarrow {}^7F_3$ and $^5D_0 \rightarrow {}^7F_4$ transitions

The $^5D_0 \rightarrow {}^7F_3$ transition is generally very weak, as it is forbidden according to the Judd–Ofelt theory. This transition can only gain intensity through J-mixing. An intense $^5D_0 \rightarrow {}^7F_3$ transition indicates strong J-mixing and a significant crystal-field perturbation. As a result, this transition is typically not considered when the Eu^{3+} ion is used as a spectroscopic probe.

Care must be taken when interpreting the intensity of the $^5D_0 \rightarrow {}^7F_4$ electric dipole (ED) transition. This transition occurs in a spectral region where most photomultiplier tubes have low sensitivity. To avoid drawing erroneous conclusions, correction of the luminescence spectra is necessary. Without correction, the intensity of the $^5D_0 \rightarrow {}^7F_4$ transition appears too weak relative to other transitions, while over-correction can lead to an exaggerated intensity for this transition. The intensity of the $^5D_0 \to {}^7F_4$ transition should not be considered in absolute terms but rather compared to the intensity of the $^5D_0 \to {}^7F_1$ magnetic dipole transition. In many europium luminescence spectra, the $^5D_0 \to {}^7F_4$ transition is weaker than the $^5D_0 \to {}^7F_2$ transition, though several exceptions exist. For compounds with D_{4d} symmetry, the $^5D_0 \to {}^7F_4$ transition often dominates the luminescence spectrum [273].

BIBLIOGRAPHY

[1] F. Bray, M. Laversanne, H. Sung, J. Ferlay, R. L. Siegel, I. Soerjomataram, and A. Jemal. Global cancer statistics 2022: GLOBOCAN estimates of incidence and mortality worldwide for 36 cancers in 185 countries. *CA: A Cancer Journal for Clinicians*, 2024.

[2] M. R. Toh, E. Y. T. Wong, S. H. Wong, A. W. T. Ng, L.-H. Loo, P. K.-H. Chow, and J. Ngeow. Global epidemiology and genetics of hepatocellular carcinoma. *Gastroenterology*, 164(5):766–782, 2023.

[3] R.-J. M. van Geuns, P. A. Wielopolski, H. G. de Bruin, B. J. Rensing, P. M. A. van Ooijen, M. Hulshoff, M. Oudkerk, and P. J. de Feyter. Basic principles of magnetic resonance imaging. *Progress in Cardiovascular Diseases*, 42(2):149–156, 1999.

[4] S. S. Rajan. Contrast agents. In *MRI: A Conceptual Overview*, chapter 5, pages 66–75. Springer, 1 edition, 1998.

[5] U. Hampel. X-ray computed tomography. In *Industrial Tomography: Systems and Applications*. Woodhead Publishing, 2022.

[6] T. Murakami, Y. Imai, M. Okada, T. Hyodo, W.-J. Lee, M.-J. Kim, T. Kim, and B. I. Choi. Ultrasonography, computed tomography and magnetic resonance

imaging of hepatocellular carcinoma: Toward improved treatment decisions. *Oncology*, 81(Suppl. 1):86–99, 2011.

[7] K. Lameka, M. D. Farwell, and M. Ichise. Positron emission tomography. In J. C. Masdeu and R. G. González, editors, *Neuroimaging Part I*, volume 135 of *Handbook of Clinical Neurology*, chapter 11, pages 209–227. Elsevier, 2016.

[8] S. Yasuda, M. Ide, H. Fujii, T. Nakahara, Y. Mochizuki, W. Takahashi, and A. Shohtsu. Application of positron emission tomography imaging to cancer screening. *British Journal of Cancer*, 83(12):1607–1611, 2000.

[9] J. B. Bomanji, D. C. Costa, and P. J. Ell. Clinical role of positron emission tomography in oncology. *The Lancet Oncology*, 2(3):157–164, 2001.

[10] A. G. Arranja, V. Pathak, T. Lammers, and Y. Shi. Tumor-targeted nanomedicines for cancer theranostics. *Pharmacological Research*, 115:87–95, 2017.

[11] K. Cho, X. Wang, S. Nie, Z. G. Chen, and D. M. Shin. Therapeutic Nanoparticles for Drug Delivery in Cancer. *Clinical Cancer Research*, 14(5):1310–1316, 2008.

[12] G. Pöpperl, T. Helmberger, W. Münzing, R. Schmid, T. F. Jacobs, and K. Tatsch. Selective internal radiation therapy with SIR-spheres® in patients with nonresectable liver tumors. *Cancer Biotherapy and Radiopharmaceuticals*, 20(2):200–208, 2005.

[13] J. Scheele and A. Altendorf-Hofmann. Resection of colorectal liver metastases. *Langenbeck's Archives of Surgery*, 384(4):313–327, 1999.

[14] P. Nygren. What is cancer chemotherapy? *Acta Oncologica*, 40(2-3):166–174, 2001.

[15] J. J.G. Marin, O. Briz, E. Herraez, E. Lozano, M. Asensio, S. Di Giacomo, M. R. Romero, L. M. Osorio-Padilla, A. I. Santos-Llamas, M. A. Serrano, C. Armengol, T. Efferth, and R. I.R. Macias. Molecular bases of the poor response of liver cancer to chemotherapy. *Clinics and Research in Hepatology and Gastroenterology*, 42(3):182–192, 2018.

[16] M. Schuster, A. Nechansky, and R. Kircheis. Cancer immunotherapy. *Biotechnology Journal*, 1(2):138–147, 2006.

[17] J. Li, S. Xuan, P. Dong, Z. Xiang, C. Gao, M. Li, L. Huang, and J. Wu. Immunotherapy of hepatocellular carcinoma: Recent progress and new strategy. *Frontiers in Immunology*, 14, 2023.

[18] H. Ikeda and H. Shiku. Immunotherapy of solid tumor: perspectives on vaccine and cell therapy. *Nihon rinsho. Japanese journal of clinical medicine*, 70(12):2043 – 2050, 2012.

[19] F. M. Khan and J. P. Gibbons. *Kahn's The Physics of Radiation Therapy*. Lippincott Williams and Wilkins, fifth edition, 2014.

[20] D. A. Jaffray and M. K. Gospodarowicz. Radiation Therapy for Cancer. In *Disease Control Priorities (Volume 3): Cancer*. World Bank Publications, 2015.

[21] L. E. Gerweck, S. Vijayappa, A. Kurimasa, K. Ogawa, and D. J. Chen. Tumor Cell Radiosensitivity Is a Major Determinant of Tumor Response to Radiation. *Cancer Research*, 66(17):8352–8355, 2006.

[22] F. X. Sundram and J. R. Buscombe. Selective internal radiation therapy for liver tumours. *Clinical Medicine*, 17(5):449–453, 2017.

[23] A. Arjuna, B. Milborne, A. R. Putra, T. R. Mulyaningsih, H. Setiawan, M. T. Islam, R. Felfel, and I. Ahmed. Development of samarium-doped phosphate glass microspheres for internal radiotheranostic applications. *International Journal of Pharmaceutics*, 653:123919, 2024.

[24] O. L. Johnson, W. Jaworowicz, J. L. Cleland, L. Bailey, M. Charnis, E. Duenas, C. Wu, D. Shepard, S. Magil, T. Last, A. J. S. Jones, and S. D. Putney. The stabilization and encapsulation of human growth hormone into biodegradable microspheres. *Pharmaceutical Research*, 14(6):730–735, 1997.

[25] C.-Y. Lin, S.-J. Lin, Y.-C. Yang, D.-Y. Wang, H.-F. Cheng, and M.-K. Yeh. Biodegradable polymeric microsphere-based vaccines and their applications in infectious diseases. *Human Vaccines and Immunotherapeutics*, 11(3):650–656, 2015.

[26] R. Sharma, C. Benwood, and S. M. Willerth. Drugreleasing microspheres for stem cell differentiation. *Current Protocols*, 1(12), 12 2021.

[27] Y. Cao, Q. Zhang, C. Wang, Y. Zhu, and G. Bai. Preparation of novel immunomagnetic cellulose microspheres via cellulose binding domain-protein A linkage and its use for the isolation of interferon α-2b. *Journal of Chromatography A*, 1149(2):228–235, 2007.

[28] W. Zhou, M. Zhang, X. Liu, W. Hussain, B. Zhu, H. Yu, S. Wang, and L. Zhou. Collagen-modified chitosan microsphere as a novel hemoperfusion adsorbent for efficient removal of bilirubin from human plasma. *Separation and Purification Technology*, 337:126303, 2024.

[29] A. M. de Figueiredo, J. C. Glória, Y. O. Chaves, W. L. L. Neves, and L. A. M. Mariúba. Diagnostic applications of microsphere-based flow cytometry: A review. *Experimental Biology and Medicine*, 247(20):1852–1861, 2022.

[30] L. Ruan, M. Su, X. Qin, Q. Ruan, W. Lang, M. Wu, Y. Chen, and Q. Lv. Progress in the application of sustained-release drug microspheres in tissue engineering. *Materials Today Bio*, 16:100394, 2022.

[31] U. O. Häfeli. Radioactive Microspheres for Medical Applications. In *Physics and Chemistry Basis of Biotechnology. Focus on Biotechnology*. Springer, 2001.

[32] P. d'Abadie, M. Hesse, A. Louppe, R. Lhommel, S. Walrand, and F. Jamar. Microspheres used in liver radioembolization: From conception to clinical effects. *Molecules*, 26(13):3966, 2021.

[33] Ahsun Riaz. Radioembolization for liver tumors (chapter 84a. In W. R. Jarnagin and L. H. Blumgart, editors, *Blumgart's Surgery of the Liver, Pancreas and Biliary Tract*, pages 1362–1369.e2. Elsevier, 2012.

[34] J. C. Harbert. Therapy with intra-arterial radioactive particles. In *Nuclear Medicine: Diagnosis and Therapy*, pages 1141–1155. Thieme Medical Pub, New York, 1996.

[35] Y. Zhou, Y. Gao, G. Duan, L. Wen, S. Shan, S. Wu, J. Zeng, and M. Gao. Radioactive microspheres for selective internal radiation therapy of hepatocellular carcinoma. *Advanced NanoBiomed Research*, 3(6), 2023.

[36] J.F.W. Nijsen. Radioactive Holmium Poly(L-Lactic Acid) Microspheres for Treatment of Liver Malignancies, 2001.

[37] C.-B. Liu, G.-Z. Liu, N. Liu, Y.-M. Zhang, J. He, M. Rusckowski, and D. J. Hnatowich. Radiolabeling morpholinos with ^{90}y, ^{111}in, ^{188}re and ^{99m}tc. *Nuclear Medicine and Biology*, 30(2):207–214, 2003.

[38] L. Van de Sande, S. Cosyns, Wouter Willaert, and W. Ceelen. Albumin-based cancer therapeutics for intraperitoneal drug delivery: A review. *Drug Delivery*, 27(1):40–53, 2019.

[39] G. Wunderlich, J. Pinkert, M. Andreeff, M. Stintz, F. F. Knapp, Jr, J. Kropp, and W.-G. Franke. Preparation and biodistribution of rhenium-188 labeled albumin microspheres B 20: A promising new agent for radiotherapy. *Applied Radiation and Isotopes*, 52(1):63–68, 2000.

[40] N. Watanabe, N. Oriuchi, K. Endo, T. Inoue, S. Tanada, H. Murata, and Y. Sasaki. Yttrium-90-labeled human macroaggregated albumin for internal

radiotherapy: Combined use with DTPA. *Nuclear Medicine and Biology*, 26(7):847–851, 1999.

[41] N. Willmott, T. Murray, R. Carlton, Y. Chen, H. Logan, G. McCurrach, R. G. Bessent, J. A. Goldberg, J. Anderson, J. H. McKillop, and C. S. McArdle. Development of radiolabelled albumin microspheres: A comparison of gamma-emitting radioisotopes of iodine (^{131}i) and indium (^{111}in/^{113m}in). *International Journal of Radiation Applications and Instrumentation. Part B. Nuclear Medicine and Biology*, 18(7):687–694, 1991.

[42] A. Alrfooh, A. Patel, and S. Laroia. Transarterial radioembolization agents: A review of the radionuclide agents and the carriers. *Nuclear Medicine and Molecular Imaging*, 55(4):162–172, 2021.

[43] D. E. Day and T. E. Day. Radiotherapy Glasses. In J. Wilson and L. L. Hench, editors, *An introduction to bioceramics, (2nd edition)*, pages 305–317. World Scientific Publishing Company, 2013.

[44] G. N. Atroshchenko, V. I. Savinkov, A. Paleari, P. D. Sarkisov, and V. N. Sigaev. Glassy microspheres with elevated yttrium oxide content for nuclear medicine. *Glass and Ceramics*, 69(1-2):39–43, 2012.

[45] C. Chiesa, M. Mira, M. Maccauro, C. Spreafico, R. Romito, C. Morosi, T. Camerini, M. Carrara, S. Pellizzari, A. Negri, G. Aliberti, C. Sposito, S. Bhoori, A. Facciorusso, E. Civelli, R. Lanocita, B. Padovano, M. Migliorisi, M. C. De Nile, E. Seregni, A. Marchianò, F. Crippa, and V. Mazzaferro. Radioembolization of hepatocarcinoma with 90y glass microspheres: Development of an individualized treatment planning strategy based on dosimetry and radiobiology. *European Journal of Nuclear Medicine and Molecular Imaging*, 42(11):1718–1738, 2015.

[46] V. N. Sigaev, G. N. Atroschenko, V. I. Savinkov, P. D. Sarkisov, G. Babajew, K. Lingel, R. Lorenzi, and A. Paleari. Structural rearrangement at the

yttrium-depleted surface of HCl-processed yttrium aluminosilicate glass for 90y-microsphere brachytherapy. *Materials Chemistry and Physics*, 133(1):24–28, 2012.

[47] M. Kawashita. Ceramic microspheres for biomedical applications. *International Journal of Applied Ceramic Technology*, 2(3):173–183, 2005.

[48] S. D. Conzone, U. O. Häfeli, D. E. Day, and G. J. Ehrhardt. Preparation and properties of radioactive rhenium glass microspheres intended forin vivo radioembolization therapy. *Journal of Biomedical Materials Research*, 42(4):617–625, 1998.

[49] S. Ho, W. Y. Lau, T. W. T. Leung, and P. J. Johnson. Internal radiation therapy for patients with primary or metastatic hepatic cancer. *Cancer*, 83(9):1894–1907, 1998.

[50] M. M. Welling, N. Duszenko, M. P. van Meerbeek, T. J. M. Molenaar, T. Buckle, F. W. B. van Leeuwen, and D. D. D. Rietbergen. Microspheres as a carrier system for therapeutic embolization procedures: Achievements and advances. *Journal of Clinical Medicine*, 12(3):918, 2023.

[51] M. Jay, S. S. Khare, R. S. Mumper, and U.Y. Ryo. Microencapsulation of activable radiotherapeutic agents. *Biological and Synthetic Membranes*, 292:293–300, 1989.

[52] K. Saralidze, L. H. Koole, and M. L. W. Knetsch. Polymeric microspheres for medical applications. *Materials*, 3(6):3537–3564, 2010.

[53] V. Lassalle and M. L. Ferreira. Pla nano and microparticles for drug delivery: An overview of the methods of preparation. *Macromolecular Bioscience*, 7(6):767–783, 2007.

[54] C. Bitz and E. Doelker. Influence of the preparation method on residual solvents in biodegradable microspheres. *International Journal of Pharmaceutics*, 131(2):171–181, 1996.

[55] F. X. Lacasse, P. Hildgen, and J. N. McMullen. Surface and morphology of spray-dried pegylated PLA microspheres. *International Journal of Pharmaceutics*, 174(1-2):101–109, 1998.

[56] T. Casalini, F. Rossi, A. Castrovinci, and G. Perale. A perspective on polylactic acid-based polymers use for nanoparticles synthesis and applications. *Frontiers in Bioengineering and Biotechnology*, 7, 2019.

[57] M. Li, O. Rouaud, and D. Poncelet. Microencapsulation by solvent evaporation: State of the art for process engineering approaches. *International Journal of Pharmaceutics*, 363(1-2):26–39, 2008.

[58] C. Wischke and S. P. Schwendeman. Principles of encapsulating hydrophobic drugs in PLA/PLGA microparticles. *International Journal of Pharmaceutics*, 364(2):298–327, 2008.

[59] X. Fu, Q. Ping, and Y. Gao. Effects of formulation factors on encapsulation efficiency and release behaviourin vitroof huperzine A-PLGA microspheres. *Journal of Microencapsulation*, 22(7):705–714, 2005.

[60] R. A. Jain, C. T. Rhodes, A. M. Railkar, A. W. Malick, and N. H. Shah. Controlled release of drugs from injectable in situ formed biodegradable PLGA microspheres: Effect of various formulation variables. *European Journal of Pharmaceutics and Biopharmaceutics*, 50(2):257–262, 2000.

[61] N.S. Berchane, K.H. Carson, A.C. Rice-Ficht, and M.J. Andrews. Effect of mean diameter and polydispersity of PLG microspheres on drug release: Experiment and theory. *International Journal of Pharmaceutics*, 337(1-2):118–126, 2007.

[62] J. Siepmann, N. Faisant, J. Akiki, J. Richard, and J.P. Benoit. Effect of the size of biodegradable microparticles on drug release: Experiment and theory. *Journal of Controlled Release*, 96(1):123–134, 2004.

[63] S. Mohan, O. S. Oluwafemi, N. Kalarikkal, S. Thomas, and S. P. Songca. Biopolymers – application in nanoscience and nanotechnology. In *Recent Advances in Biopolymers*. InTech, 2016.

[64] K. J. Jem and B. Tan. The development and challenges of poly (lactic acid) and poly (glycolic acid). *Advanced Industrial and Engineering Polymer Research*, 3(2):60–70, 2020.

[65] V. DeStefano, S. Khan, and A. Tabada. Applications of PLA in modern medicine. *Engineered Regeneration*, 1:76–87, 2020.

[66] L. Ranakoti, B. Gangil, S. K. Mishra, T. Singh, S. Sharma, R. A. Ilyas, and S. El-Khatib. Critical review on polylactic acid: Properties, structure, processing, biocomposites, and nanocomposites. *Materials*, 15(12):4312, 2022.

[67] D. Garlotta. A literature review of Poly(Lactic Acid). *Journal of Polymers and the Environment*, 9(2):63–84, 2001.

[68] M. Ajioka, K. Enomoto, K. Suzuki, and A. Yamaguchi. The basic properties of poly(lactic acid) produced by the direct condensation polymerization of lactic acid. *Journal of Environmental Polymer Degradation*, 3(4):225–234, 1995.

[69] A. Ahmad, F. Banat, H. Alsafar, and S. W. Hasan. An overview of biodegradable poly (lactic acid) production from fermentative lactic acid for biomedical and bioplastic applications. *Biomass Conversion and Biorefinery*, 14(3):3057–3076, 2022.

[70] A. Södergård and M. Stolt. Properties of lactic acid based polymers and their correlation with composition. *Progress in Polymer Science*, 27(6):1123–1163, 2002.

[71] O. Dechy-Cabaret, B. Martin-Vaca, and D. Bourissou. Controlled ring-opening polymerization of lactide and glycolide. *Chemical Reviews*, 104(12):6147–6176, 2004.

[72] M. Santoro, S. R. Shah, J. L. Walker, and A. G. Mikos. Poly(lactic acid) nanofibrous scaffolds for tissue engineering. *Advanced Drug Delivery Reviews*, 107:206–212, 2016.

[73] R. P. John, K. M. Nampoothiri, and A. Pandey. Fermentative production of lactic acid from biomass: An overview on process developments and future perspectives. *Applied Microbiology and Biotechnology*, 74(3):524–534, 2007.

[74] M. S. Lopes, A.L. Jardini, and R. M. Filho. Poly (lactic acid) production for tissue engineering applications. *Procedia Engineering*, 42:1402–1413, 2012.

[75] J. Tan, M. A. Abdel-Rahman, and K. Sonomoto. Biorefinery-Based lactic acid fermentation: Microbial production of pure monomer product. In *Synthesis, Structure and Properties of Poly(lactic acid)*, pages 27–66. Springer International Publishing, Cham, 2017.

[76] J. M. Nduko and S. Taguchi. Microbial production of biodegradable lactate-based polymers and oligomeric building blocks from renewable and waste resources. *Frontiers in Bioengineering and Biotechnology*, 8, 2021.

[77] C. I. Gkountela and S. N. Vouyiouka. Enzymatic polymerization as a green approach to synthesizing bio-based polyesters. *Macromol*, 2(1):30–57, 2022.

[78] E. Balla, V. Daniilidis, G. Karlioti, T. Kalamas, M. Stefanidou, N. D. Bikiaris, A. Vlachopoulos, I. Koumentakou, and D. N. Bikiaris. Poly(lactic acid): A versatile biobased polymer for the future with multifunctional properties—from monomer synthesis, polymerization techniques and molecular weight increase to PLA applications. *Polymers*, 13(11):1822, 2021.

[79] W. Hoogsteen, A. R. Postema, A. J. Pennings, G. Ten Brinke, and P. Zugenmaier. Crystal structure, conformation and morphology of solution-spun poly(L-lactide) fibers. *Macromolecules*, 23(2):634–642, 1990.

[80] J. Kobayashi, T. Asahi, M. Ichiki, A. Oikawa, H. Suzuki, T. Watanabe, E. Fukada, and Y. Shikinami. Structural and optical properties of poly lactic acids. *Journal of Applied Physics*, 77(7):2957–2973, 1995.

[81] C. Alemán, B. Lotz, and J. Puiggali. Crystal Structure of the α-Form of Poly(l-lactide). *Macromolecules*, 34(14):4795–4801, 2001.

[82] Shuhui Kang, Shaw Ling Hsu, Howard D. Stidham, Patrick B. Smith, M. Anne Leugers, and Xiaozhen Yang. A Spectroscopic Analysis of Poly(lactic acid) Structure. *Macromolecules*, 34(13):4542–4548, 2001.

[83] S. Sasaki and T. Asakura. Helix Distortion and Crystal Structure of the α-Form of Poly(l-lactide). *Macromolecules*, 36(22):8385–8390, 2003.

[84] K. Aou and S. L. Hsu. Trichroic Vibrational Analysis on the α-Form of Poly(lactic acid) Crystals Using Highly Oriented Fibers and Spherulites. *Macromolecules*, 39(9):3337–3344, 2006.

[85] K. Wasanasuk, K. Tashiro, M. Hanesaka, T. Ohhara, K. Kurihara, R. Kuroki, T. Tamada, T. Ozeki, and T. Kanamoto. Crystal Structure Analysis of Poly(l-lactic Acid) α Form On the basis of the 2-Dimensional Wide-Angle Synchrotron X-ray and Neutron Diffraction Measurements. *Macromolecules*, 44(16):6441–6452, 2011.

[86] B. Lotz. Crystal Polymorphism and Morphology of Polylactides. In *Synthesis, Structure and Properties of Poly(lactic acid)*, pages 273–302. Springer, 2017.

[87] J. Zhang, Y. Duan, H. Sato, H. Tsuji, I. Noda, S. Yan, and Y. Ozaki. Crystal Modifications and Thermal Behavior of Poly(l-lactic acid) Revealed by Infrared Spectroscopy. *Macromolecules*, 38(19):8012–8021, 2005.

[88] L. Aliotta, P. Cinelli, M. B. Coltelli, M. C. Righetti, M. Gazzano, and A. Lazzeri. Effect of nucleating agents on crystallinity and properties of poly (lactic acid) (PLA). *European Polymer Journal*, 93:822–832, 2017.

[89] J. Puiggali, Y. Ikada, H. Tsuji, L. Cartier, T. Okihara, and B. Lotz. The frustrated structure of poly(L-lactide). *Polymer*, 41(25):8921–8930, 2000.

[90] L. Cartier, T. Okihara, Y. Ikada, H. Tsuji, J. Puiggali, and B. Lotz. Epitaxial crystallization and crystalline polymorphism of polylactides. *Polymer*, 41(25):8909–8919, 2000.

[91] P. Pan and Y. Inoue. Polymorphism and isomorphism in biodegradable polyesters. *Progress in Polymer Science*, 34(7):605–640, 2009.

[92] S. Saeidlou, M. A. Huneault, H. Li, and C. B. Park. Poly(lactic acid) crystallization. *Progress in Polymer Science*, 37(12):1657–1677, 2012.

[93] R. Androsch and B. Wunderlich. The link between rigid amorphous fraction and crystal perfection in cold-crystallized poly(ethylene terephthalate). *Polymer*, 46(26):12556–12566, 2005.

[94] M. Kattan, E. Dargent, and J. Grenet. Three phase model in drawn thermoplastic polyesters: Comparison of differential scanning calorimetry and thermally stimulated depolarisation current experiments. *Polymer*, 43(4):1399–1405, 2002.

[95] N. Delpouve, M. Arnoult, A. Saiter, E. Dargent, and J.-M. Saiter. Evidence of two mobile amorphous phases in semicrystalline polylactide observed from calorimetric investigations. *Polymer Engineering and Science*, 54(5):1144–1150, 2013.

[96] J. Lin, S. Shenogin, and S. Nazarenko. Oxygen solubility and specific volume of rigid amorphous fraction in semicrystalline poly(ethylene terephthalate). *Polymer*, 43(17):4733–4743, 2002.

[97] R. Picciochi, Y. Wang, N. M. Alves, and J. F. Mano. Glass transition of semicrystalline PLLA with different morphologies as studied by dynamic mechanical analysis. *Colloid and Polymer Science*, 285(5):575–580, 2006.

[98] M. L. Di Lorenzo, M. Cocca, and M. Malinconico. Crystal polymorphism of poly(l-lactic acid) and its influence on thermal properties. *Thermochimica Acta*, 522(1-2):110–117, 2011.

[99] L. Fambri and C. Migliaresi. Crystallization and Thermal Properties. In *Poly(lactic acid): Synthesis, Structures, Properties, Processing, and Applications*, pages 113–124. John Wiley & Sons, 2010.

[100] E. W. Fischer, H. J. Sterzel, and G. Wegner. Investigation of the structure of solution grown crystals of lactide copolymers by means of chemical reactions. *Kolloid-Zeitschrift und Zeitschrift für Polymere*, 251(11):980–990, 1973.

[101] T. M. Ovitt and G. W. Coates. Stereochemistry of lactide polymerization with chiral catalysts: New opportunities for stereocontrol using polymer exchange mechanisms. *Journal of the American Chemical Society*, 124(7):1316–1326, 2002.

[102] Y. Ikada, K. Jamshidi, H. Tsuji, and S. H. Hyon. Stereocomplex formation between enantiomeric poly(lactides). *Macromolecules*, 20(4):904–906, 1987.

[103] J. F. Mano, Y. Wang, J. C. Viana, Z. Denchev, and M. J. Oliveira. Cold crystallization of PLLA studied by simultaneous SAXS and WAXS. *Macromolecular Materials and Engineering*, 289(10):910–915, 2004.

[104] Y. Wang, J. L. Gómez Ribelles, M. Salmerón Sánchez, and J. F. Mano. Morphological Contributions to Glass Transition in Poly(l-lactic acid). *Macromolecules*, 38(11):4712–4718, 2005.

[105] J. Henricks, M. Boyum, and W. Zheng. Crystallization kinetics and structure evolution of a polylactic acid during melt and cold crystallization. *Journal of Thermal Analysis and Calorimetry*, 120(3):1765–1774, 2015.

[106] B. Wunderlich. Reversible crystallization and the rigid–amorphous phase in semicrystalline macromolecules. *Progress in Polymer Science*, 28(3):383–450, 2003. [Online; accessed 2024-11-18].

[107] A.H. Kuptsov and G.N. Zhizhin. *Handbook of Fourier Transform Raman and Infrared spectra of Polymers*, volume 45. Elsevier, 1998.

[108] J. Zhang, H. Tsuji, I. Noda, and Y. Ozaki. Structural changes and crystallization dynamics of poly(l-lactide) during the cold-crystallization process investigated by infrared and two-dimensional infrared correlation spectroscopy. *Macromolecules*, 37(17):6433–6439, 2004.

[109] G Kister, G Cassanas, and M Vert. Effects of morphology, conformation and configuration on the IR and Raman spectra of various poly(lactic acid)s. *Polymer*, 39(2):267–273, 1998.

[110] E. Meaurio, E. Zuza, N. López-Rodríguez, and J. R. Sarasua. Conformational behavior of poly(l-lactide) studied by infrared spectroscopy. *The Journal of Physical Chemistry B*, 110(11):5790–5800, 2006.

[111] D. Qin and R. T. Kean. Crystallinity determination of polylactide by ft-raman spectrometry. *Applied Spectroscopy*, 52(4):488–495, 1998.

[112] J. Zhang, H. Tsuji, I. Noda, and Y. Ozaki. Weak intermolecular interactions during the melt crystallization of poly(l-lactide) investigated by two-dimensional infrared correlation spectroscopy. *The Journal of Physical Chemistry B*, 108(31):11514–11520, 2004.

[113] B. G. Frushour and J. L. Koenig. Raman spectra of D and L amino acid copolymers. PolyDLalanine, polyDLleucine, and polyDLlysine. *Biopolymers*, 14(2):363–377, 1975.

[114] E. Andreassen. Infrared and Raman spectroscopy of polypropylene. In *Polypropylene. Polymer Science and Technology Series, vol.2*, pages 320–328. Springer, 1999.

[115] F. Alexis. Factors affecting the degradation and drug release mechanism of poly(lactic acid) and poly[(lactic acid)co(glycolic acid)]. *Polymer International*, 54(1):36–46, 2004.

[116] H. Tsuji. Hydrolytic degradation. In *Poly(lactic acid): Synthesis, Structures, Properties, Processing, and Applications*, pages 345–381. John Wiley and Sons, 2010.

[117] M. F. Gonzalez, R. A. Ruseckaite, and T. R. Cuadrado. Structural changes of polylactic-acid (PLA) microspheres under hydrolytic degradation. *Journal of Applied Polymer Science*, 71(8):1223–1230, 1999.

[118] S.J de Jong, E.R Arias, D.T.S Rijkers, C.F van Nostrum, J.J Kettenes-van den Bosch, and W.E Hennink. New insights into the hydrolytic degradation of poly(lactic acid): Participation of the alcohol terminus. *Polymer*, 42(7):2795–2802, 2001.

[119] A.M. Reed and D.K. Gilding. Biodegradable polymers for use in surgery — poly(glycolic)/poly(Iactic acid) homo and copolymers: 2. In vitro degradation. *Polymer*, 22(4):494–498, 1981.

[120] H. Tsuji, A. Mizuno, and Y. Ikada. Properties and morphology of poly(L-lactide). III. Effects of initial crystallinity on long-termin vitro hydrolysis of high molecular weight poly(L-lactide) film in phosphate-buffered solution. *Journal of Applied Polymer Science*, 77(7):1452–1464, 2000.

[121] S. Pérez Davila, L. González Rodríguez, S. Chiussi, J. Serra, and P. González. How to sterilize polylactic acid based medical devices? *Polymers*, 13(13):2115, 2021.

[122] J.S.C. Loo, C.P. Ooi, and F.Y.C. Boey. Degradation of poly(lactide-co-glycolide) (PLGA) and poly(l-lactide) (PLLA) by electron beam radiation. *Biomaterials*, 26(12):1359–1367, 2005.

[123] M. B. Sintzel, A. Merkli, C. Tabatabay, and R. Gurny. Influence of irradiation sterilization on polymers used as drug carriers—a review. *Drug Development and Industrial Pharmacy*, 23(9):857–878, 1997.

[124] E. C. Grosvenor, J. C. Hughes, C. W. Stanfield, R. L. Blanchard, A. C. Fox, O. L. Mihok, K. Lee, J. R. Brodsky, A. Hoy, A. Uniyal, S. M. Whitaker, C. Acha,

K. Gibson, L. Ding, C. A. Lewis, L. González López, C. M. Wentz, L. R. Sita, and M. Al-Sheikhly. On the Mechanism of Electron Beam Radiation-Induced Modification of Poly(lactic acid) for Applications in Biodegradable Food Packaging. *Applied Sciences*, 12(4):1819, 2022.

[125] M. Vidotto, B. Mihaljević, G. Žauhar, E. Vidović, N. Maltar-Strmečki, D. Klepac, and S. Valić. Effects of γ-radiation on structure and properties of poly(lactic acid) filaments. *Radiation Physics and Chemistry*, 184:109456, 2021.

[126] A. Alsabbagh, R. Abu Saleem, R. Almasri, S. Aljarrah, and S. Awad. Effects of gamma irradiation on 3d-printed polylactic acid (PLA) and high-density polyethylene (HDPE). *Polymer Bulletin*, 78(9):4931–4945, 2020.

[127] T. Aouat, M. Kaci, J.-M. Lopez-Cuesta, E. Devaux, and M. Mahlous. The effect of gamma-irradiation on morphology and properties of melt-spun poly (lactic acid)/cellulose fibers. *Polymer Degradation and Stability*, 160:14–23, 2019.

[128] M.-L. Cairns, G. R. Dickson, J. F. Orr, D. Farrar, K. Hawkins, and F. J. Buchanan. Electron-beam treatment of poly(lactic acid) to control degradation profiles. *Polymer Degradation and Stability*, 96(1):76–83, 2011.

[129] A. J.R. Lasprilla, G. A.R. Martinez, B. H. Lunelli, A. L. Jardini, and R. M. Filho. Poly-lactic acid synthesis for application in biomedical devices — A review. *Biotechnology Advances*, 30(1):321–328, 2012.

[130] S. Farah, D. G. Anderson, and R. Langer. Physical and mechanical properties of PLA, and their functions in widespread applications — A comprehensive review. *Advanced Drug Delivery Reviews*, 107:367–392, 2016.

[131] S. Suzuki and Y. Ikada. Medical applications. In *Poly(Lactic Acid): Synthesis, Structures, Properties, Processing, Applications, and End of Life, Second Edition*, pages 581–604. Wiley, 2022.

[132] Z. Sheikh, S. Najeeb, Z. Khurshid, V. Verma, H. Rashid, and M. Glogauer. Biodegradable materials for bone repair and tissue engineering applications. *Materials*, 8(9):5744–5794, 2015.

[133] S. M. Davachi and B. Kaffashi. Polylactic acid in medicine. *Polymer-Plastics Technology and Engineering*, 54(9):944–967, 2015.

[134] L. Wang, L. Jiao, S. Pang, P. Yan, X. Wang, and T. Qiu. The development of design and manufacture techniques for bioresorbable coronary artery stents. *Micromachines*, 12(8):990, 2021.

[135] N. G. Khouri, J. O. Bahú, C. Blanco-Llamero, P. Severino, V. O.C. Concha, and E. B. Souto. Polylactic acid (PLA): Properties, synthesis, and biomedical applications – A review of the literature. *Journal of Molecular Structure*, 1309:138243, 2024.

[136] B. Tyler, D. Gullotti, A. Mangraviti, T. Utsuki, and H. Brem. Polylactic acid (PLA) controlled delivery carriers for biomedical applications. *Advanced Drug Delivery Reviews*, 107:163–175, 2016.

[137] D J Armstrong, P N C Elliott, J L Ford, D Gadsdon, G P Mccarthy, C Rostron, and M D Worsley. Poly-(d,l-Lactic acid) microspheres incorporating histological dyes for intra-pulmonary histopathological investigations. *Journal of Pharmacy and Pharmacology*, 48(3):258–262, 1996.

[138] M. T.M. Reinders, M. L.J. Smits, C. van Roekel, and A. J.A.T. Braat. Holmium-166 microsphere radioembolization of hepatic malignancies. *Seminars in Nuclear Medicine*, 49(3):237–243, 2019.

[139] S. K. Pandey, D. K. Patel, R. Thakur, D. P. Mishra, P. Maiti, and C. Haldar. Anti-cancer evaluation of quercetin embedded PLA nanoparticles synthesized by emulsified nanoprecipitation. *International Journal of Biological Macromolecules*, 75:521–529, 2015.

[140] P. B. O'Donnell and J. W. McGinity. Preparation of microspheres by the solvent evaporation technique. *Advanced Drug Delivery Reviews*, 28(1):25–42, 1997.

[141] B. Yu, L. Meng, S. Fu, Z. Zhao, Y. Liu, K. Wang, and Q. Fu. Morphology and internal structure control over PLA microspheres by compounding PLLA and PDLA and effects on drug release behavior. *Colloids and Surfaces B: Biointerfaces*, 172:105–112, 2018.

[142] D. Bondeson and K. Oksman. Polylactic acid/cellulose whisker nanocomposites modified by polyvinyl alcohol. *Composites Part A: Applied Science and Manufacturing*, 38(12):2486–2492, 2007.

[143] Y. Capan, B.H. Woo, S. Gebrekidan, S. Ahmed, and P. P. DeLuca. Influence of formulation parameters on the characteristics of poly(d,l-lactide-co-glycolide) microspheres containing poly(l-lysine) complexed plasmid DNA. *Journal of Controlled Release*, 60(2-3):279–286, 1999.

[144] H. Heiskanen, P. Denifl, P. Pitkänen, and M. Hurme. Effect of concentration and temperature on the properties of the microspheres prepared using an emulsion–solvent extraction process. *Advanced Powder Technology*, 23(6):779–786, 2012.

[145] Y.-Y. Yang, T.-S. Chung, and N.P Ng. Morphology, drug distribution, and in vitro release profiles of biodegradable polymeric microspheres containing protein fabricated by double-emulsion solvent extraction/evaporation method. *Biomaterials*, 22(3):231–241, 2001.

[146] K. J. Houthuijs, J. Martens, A. G. Arranja, G. Berden, J. F. W. Nijsen, and Jos Oomens. Characterization of holmium(iii)-acetylacetonate complexes derived from therapeutic microspheres by infrared ion spectroscopy. *Physical Chemistry Chemical Physics*, 22(27):15716–15722, 2020.

[147] G. Aromi, P. Gamez, and J. Reedijk. Poly beta-diketones: Prime ligands to generate supramolecular metalloclusters. *Coordination Chemistry Reviews*, 252(8-9):964–989, 2008.

[148] H. R. Kricheldorf and S. M. Weidner. Syntheses of polylactides by means of tin catalysts. *Polymer Chemistry*, 13(12):1618–1647, 2022.

[149] N. Chelghoum, M. Guessoum, M. Fois, and N. Haddaoui. Contribution of Catalytic Transesterification Reactions to the Compatibilization of Poly(lactic acid)/Polycarbonate Blends: Thermal, Morphological and Viscoelastic Characterization. *Journal of Polymers and the Environment*, 26(1):342–354, 2017.

[150] A. Larous, M. Guessoum, S. Nekkaa, and M. Fois. Novel biocomposites based on El Retma natural fiber and PLA/PC mixture compatibilized using samarium acetylacetonate catalyzed interchange reactions. *Polymer Science, Series B*, 64(3):313–325, 2022.

[151] N. E.-H. Aouadi, A. Hellati, M. Guessoum, A.-H. I. Mourad, and C. Nizamudeen. Impact of Samarium Acetylacetonate Catalyst on the Compatibilization of Poly(lactic acid)/Poly(ethylene-co-vinyl acetate) Blends: Thermomechanical, Chemical, and Viscoelastic Characterizations. *Polymer Science, Series B*, 63(3):218–231, 2021.

[152] Y.-H. Wong, H.-Y. Tan, A. Kasbollah, B. J. J. Abdullah, R. U. Acharya, and C.-H. Yeong. Neutron-activated biodegradable samarium-153 acetylactonate-poly-L-lactic acid microspheres for intraarterial radioembolization of hepatic tumors. *World Journal of Experimental Medicine*, 10(2):10–25, 2020.

[153] K. Yavari, E. Yeganeh, and H. Abolghasemi. Production and characterization of166ho polylactic acid microspheres. *Journal of Labelled Compounds and Radiopharmaceuticals*, 59(1):24–29, 2015.

[154] R. C. Bakker, R. de Roos, F.F. T. Ververs, M. G.E.H. Lam, M.K. van der Lee, B. A. Zonnenberg, and G. C. Krijger. Blood and urine analyses after ra-

dioembolization of liver malignancies with [166ho]Ho-acetylacetonate-poly(l-lactic acid) microspheres. *Nuclear Medicine and Biology*, 71:11–18, 2019.

[155] J.F.W Nijsen, A.D van het Schip, M.J van Steenbergen, S.W Zielhuis, L.M.J Kroon-Batenburg, M van de Weert, P.P van Rijk, and W.E Hennink. Influence of neutron irradiation on holmium acetylacetonate loaded poly(l-lactic acid) microspheres. *Biomaterials*, 23(8):1831–1839, 2002.

[156] R. J. Mumper, U. Y. Ryo, and M. Jay. Neutron-Activated Holmium- 166-Poly (L-Lactic Acid) Microspheres: A Potential Agent for the Internal Radiation Therapy of Hepatic Tumors. *Journal of Nuclear Medicine*, 32:2139–2143, 1991.

[157] W. Bult, P. R. Seevinck, G. C. Krijger, T. Visser, L. M. J. Kroon-Batenburg, C. J. G. Bakker, W. E. Hennink, A. D. van het Schip, and J. F. W. Nijsen. Microspheres with ultrahigh holmium content for radioablation of malignancies. *Pharmaceutical Research*, 26(6):1371–1378, 2009.

[158] A.G. Arranja, W.E. Hennink, A.G. Denkova, R.W.A. Hendrikx, and J.F.W. Nijsen. Radioactive holmium phosphate microspheres for cancer treatment. *International Journal of Pharmaceutics*, 548(1):73–81, 2018.

[159] M. Jamre, M. Shamsaei, M. G. Maragheh, and S. Sadjadi. Novel 175yb-poly (l-lactic acid) microspheres for transarterial radioembolization of unrespectable hepatocellular carcinoma. *Iranian Journal of Pharmaceutical Research : IJPR*, 18(2), 2019.

[160] S. W. Zielhuis, J. F. W. Nijsen, J.-H. Seppenwoolde, C. J. G. Bakker, G. C. Krijger, H. F. J. Dullens, B. A. Zonnenberg, P. P. van Rijk, W. E. Hennink, and A. D. van het Schip. Long-term toxicity of holmium-loaded poly(l-lactic acid) microspheres in rats. *Biomaterials*, 28(31):4591–4599, 2007.

[161] X.-Y. Qin, X.-X. Liu, Z.-Y. Li, L.-Y. Guo, Z.-Z. Zheng, H.-T. Guan, L. Song, Y.-H. Zou, and T.-Y. Fan. Mri detectable polymer microspheres embedded with

magnetic ferrite nanoclusters for embolization: In vitro and in vivo evaluation. *International Journal of Nanomedicine*, Volume 14:8989–9006, 2019.

[162] S. Madival, R. Auras, S. P. Singh, and R. Narayan. Assessment of the environmental profile of PLA, PET and PS clamshell containers using LCA methodology. *Journal of Cleaner Production*, 17(13):1183–1194, 2009.

[163] E. R. Rezvani Ghomi, F. Khosravi, A. S. Saedi Ardahaei, Y. Dai, R. E. Neisiany, F. Foroughi, M. Wu, O. Das, and S. Ramakrishna. The life cycle assessment for polylactic acid (PLA) to make it a low-carbon material. *Polymers*, 13(11):1854, 2021.

[164] U. Suwanmanee, T. Leejarkpai, and T. Mungcharoen. Assessment of greenhouse gas (GHG) emissions of polylactic acid (pla)/starch and polyethylene terephthalate (PET) trays. *Advanced Materials Research*, 518-523:1468–1474, 2012.

[165] M. P. Desole, C. Aversa, M. Barletta, A. Gisario, and A. Vosooghnia. Life cycle assessment (LCA) of PET and PLA bottles for the packaging of fresh pasteurised milk: The role of the manufacturing process and the disposal scenario. *Packaging Technology and Science*, 35(2):135–152, 2021.

[166] A. Fonseca, E. Ramalho, A. Gouveia, F. Figueiredo, and J. Nunes. Life cycle assessment of PLA products: A systematic literature review. *Sustainability*, 15(16):12470, 2023.

[167] V. Aryan, D. Maga, P. Majgaonkar, and R. Hanich. Valorisation of polylactic acid (PLA) waste: A comparative life cycle assessment of various solvent-based chemical recycling technologies. *Resources, Conservation and Recycling*, 172:105670, 2021.

[168] A. Ashfaq, M.-C. Clochard, X. Coqueret, C. Dispenza, M. S. Driscoll, P. Ulański, and M. Al-Sheikhly. Polymerization reactions and modifications of polymers by ionizing radiation. *Polymers*, 12(12):2877, 2020.

[169] S. Ho, W. Y. Lau, T. W. T. Leung, M. Chan, P. J. Johnson, and A. K. C. Li. Clinical evaluation of the partition model for estimating radiation doses from yttrium-90 microspheres in the treatment of hepatic cancer. *European Journal of Nuclear Medicine*, 24(3):293–298, 1997.

[170] J. S. Welsh. Radiographically identified necrosis after 90y microsphere brachytherapy: A new standard for oncologic response assessment? *American Journal of Roentgenology*, 188(3):765–767, 2007.

[171] M. Rahimi, G. Charmi, K. Matyjaszewski, X. Banquy, and J. Pietrasik. Recent developments in natural and synthetic polymeric drug delivery systems used for the treatment of osteoarthritis. *Acta Biomaterialia*, 123:31–50, 2021.

[172] P. Jana, M. Shyam, S. Singh, V. Jayaprakash, and A. Dev. Biodegradable polymers in drug delivery and oral vaccination. *European Polymer Journal*, 142:110155, 2021.

[173] J. F. W. Nijsen, B. A. Zonnenberg, J. R. W. Woittiez, D. W. Rook, I. A. Swildens-van Woudenberg, P. P. van Rijk, and A. D. van het Schip. Holmium-166 poly lactic acid microspheres applicable for intra-arterial radionuclide therapy of hepatic malignancies: Effects of preparation and neutron activation techniques. *European Journal of Nuclear Medicine and Molecular Imaging*, 26(7):699–704, 1999.

[174] J. F. W. Nijsen, M. J. van Steenbergen, H. Kooijman, H. Talsma, L. M. J. Kroon-Batenburg, M. van de Weert, P. P. van Rijk, A. de Witte, A. D. van het Schip, and W. E. Hennink. Characterization of poly(l-lactic acid) microspheres loaded with holmium acetylacetonate. *Biomaterials*, 22(22):3073–3081, 2001.

[175] J.F. Nijsen, A.D. Schip, W. Hennink, D. Rook, P. van Rijk, and J.M.H. Klerk. Advances in nuclear oncology: Microspheres for internal radionuclide therapy of liver tumours. *Current Medicinal Chemistry*, 9(1):73–82, 2002.

[176] S. W. Zielhuis, J. F. W. Nijsen, R. de Roos, G. C. Krijger, P. P. van Rijk, W. E. Hennink, and A. D. van het Schip. Production of GMP-grade radioactive

holmium loaded poly(l-lactic acid) microspheres for clinical application. *International Journal of Pharmaceutics*, 311(1-2):69–74, 2006.

[177] Y. Yıldırım and A. Oral. The influence of γ-ray irradiation on the thermal stability and molecular weight of Poly(l-Lactic acid) and its nanocomposites. *Radiation Physics and Chemistry*, 96:69–74, 2014.

[178] M.-L. Cairns, G. R. Dickson, J. F. Orr, D. Farrar, C. Hardacre, J. Sa, P. Lemoine, M. Z. Mughal, and F. J. Buchanan. The potential of electron beam radiation for simultaneous surface modification and bioresorption control of PLLA. *Journal of Biomedical Materials Research Part A*, 100A(9):2223–2229, 2012.

[179] T. A. M. Valente, D. M. Silva, P. S. Gomes, M. H. Fernandes, J. D. Santos, and V. Sencadas. Effect of Sterilization Methods on Electrospun Poly(lactic acid) (PLA) Fiber Alignment for Biomedical Applications. *ACS Applied Materials and Interfaces*, 8(5):3241–3249, 2016.

[180] T. J. Madera-Santana, R. Meléndrez, G. González-García, P. Quintana-Owen, and S. D. Pillai. Effect of γ irradiation on physicochemical properties of commercial poly(lactic acid) clamshell for food packaging. *Radiation Physics and Chemistry*, 123:6–13, 2016.

[181] M. Rzepna, J. Sadło, G. Przybytniak, and A. Iuliano. Impact of electron beam treatment on copolymers of polylactide and poly(trimethylene carbonate) in an air atmosphere. *Journal of Applied Polymer Science*, 138(15), 2020.

[182] L. Zaidi, S. Bruzaud, M. Kaci, A. Bourmaud, N. Gautier, and Y. Grohens. The effects of γ irradiation on the morphology and properties of polylactide/Cloisite 30b nanocomposites. *Polymer Degradation and Stability*, 98(1):348–355, 2013.

[183] I. Zembouai, M. Kaci, S. Bruzaud, I. Pillin, J.-L. Audic, S. Shayanfar, and S. D. Pillai. Electron beam radiation effects on properties and ecotoxicity of PHBV/PLA blends in presence of organo-modified montmorillonite. *Polymer Degradation and Stability*, 132:117–126, 2016.

[184] A. Babanalbandi, D. J. T. Hill, J. H. O'Donnell, and P. J. Pomery. An electron spin resonance analysis on γ-irradiated poly(glycolic acid) and its copolymers with lactic acid. *Polymer Degradation and Stability*, 52(1):59–66, 1996.

[185] E. Olewnik-Kruszkowska, I. Koter, J. Skopińska-Wiśniewska, and J. Richert. Degradation of polylactide composites under UV irradiation at 254 nm. *Journal of Photochemistry and Photobiology A: Chemistry*, 311:144–153, 2015.

[186] J. Kowalonek, I. Vuković-Kwiatkowska, D. Moszyński, and H. Kaczmarek. Surface properties of poly(lactic acid)/polyacrylate semi-interpenetrating networks – Effect of UVC radiation. *Polymer Degradation and Stability*, 131:71–81, 2016.

[187] D. Brizzolara, H.-J. Cantow, K. Diederichs, E. Keller, and A. J. Domb. Mechanism of the Stereocomplex Formation between enantiomeric poly(lactide)s. *Macromolecules*, 29(1):191–197, 1996.

[188] George Socrates. *Infrared and Raman Characteristic Group Frequencies, Tables and Charts*. John Wiley & Sons, Ltd., Baffins Lane, Chichester UK, 2001.

[189] M. Bredács, C. Barretta, L.F. Castillon, A. Frank, G. Oreski, G. Pinter, and S. Gergely. Prediction of polyethylene density from FTIR and Raman spectroscopy using multivariate data analysis. *Polymer Testing*, 104:107406, 2021.

[190] S. Bocchini, K. Fukushima, A. Di Blasio, A. Fina, A. Frache, and F. Geobaldo. Polylactic acid and polylactic acid-based nanocomposite photooxidation. *Biomacromolecules*, 11(11):2919–2926, 2010.

[191] L. Nasdala. The incorporation of hydroxyl groups and molecular water in natural zircon (ZrSiO4). *American Journal of Science*, 301(10):831–857, 2001.

[192] J.-W. Cao, J.-Y. Chen, X.-L. Qin, X.-L. Zhu, L. Jiang, Y. Gu, X.-H. Yu, and P. Zhang. Dft investigations of the vibrational spectra and translational modes of ice II. *Molecules*, 24(17):3135, 2019.

[193] Z. Wang, A. Pakoulev, Y. Pang, and D. D. Dlott. Vibrational substructure in the OH stretching transition of water and HOD. *The Journal of Physical Chemistry A*, 108(42):9054–9063, 2004.

[194] T. Seki, K.-Y. Chiang, C.-C. Yu, X. Yu, M. Okuno, J. Hunger, Y. Nagata, and M. Bonn. The bending mode of water: A powerful probe for hydrogen bond structure of aqueous systems. *The Journal of Physical Chemistry Letters*, 11(19):8459–8469, 2020.

[195] H. Hanawa, K. Kunimatsu, M. Watanabe, and H. Uchida. In situ ATR-FTIR analysis of the structure of nafion–Pt/C and nafion–Pt3Co/C interfaces in fuel cell. *The Journal of Physical Chemistry C*, 116(40):21401–21406, 2012.

[196] O. Vyavahare, D. Ng, and S. L. Hsu. Analysis of Structural Rearrangements of Poly(lactic acid) in the Presence of Water. *The Journal of Physical Chemistry B*, 118(15):4185–4193, 2014.

[197] R. Brudler, H. J. de Groot, W. B. van Liemt, W. F. Steggerda, R. Esmeijer, P. Gast, A. J. Hoff, J. Lugtenburg, and K. Gerwert. Asymmetric binding of the 1- and 4-C=O groups of QA in Rhodobacter sphaeroides R26 reaction centres monitored by Fourier transform infra-red spectroscopy using site-specific isotopically labelled ubiquinone-10. *The EMBO Journal*, 13(23):5523–5530, 1994.

[198] A. M. Herrera-González, M. Caldera-Villalobos, A. A. Pérez-Mondragón, C. E. Cuevas-Suárez, and J. A. González-López. Analysis of double bond conversion of photopolymerizable monomers by FTIR-ATR spectroscopy. *Journal of Chemical Education*, 96(8):1786–1789, 2019.

[199] J. R. Rocca-Smith, T. Karbowiak, E. Marcuzzo, A. Sensidoni, F. Piasente, D. Champion, O. Heinz, P. Vitry, E. Bourillot, E. Lesniewska, and F. Debeaufort. Impact of corona treatment on PLA film properties. *Polymer Degradation and Stability*, 132:109–116, 2016.

[200] T. Saiga, S. Sato, and K. Nagai. Water vapor solubility of poly(lactic acid) films modified the surface by vacuum ultraviolet irradiation. *Journal of Applied Polymer Science*, 132(27), 2015.

[201] C. West, R. McTaggart, T. Letcher, D. Raynie, and R. Roy. Effects of γ irradiation upon the mechanical and chemical properties of 3d-printed samples of polylactic acid. *Journal of Manufacturing Science and Engineering*, 141(4), 2019.

[202] F. Navarro-Pardo, G. Martínez-Barrera, A. Martínez-Hernández, V. Castaño, J. Rivera-Armenta, F. Medellín-Rodríguez, and C. Velasco-Santos. Effects on the thermo-mechanical and crystallinity properties of nylon 6,6 electrospun fibres reinforced with one dimensional (1d) and two dimensional (2d) carbon. *Materials*, 6(8):3494–3513, 2013.

[203] E. Ikada. Photo- and bio-degradable polyesters. Photodegradation behaviors of aliphatic polyesters. *Journal of Photopolymer Science and Technology*, 10(2):265–270, 1997.

[204] A. Fujii, E. Fujimaki, T. Ebata, and N. Mikami. A New Type of Intramolecular Hydrogen Bonding: Hydroxyl−Methyl Interactions in the o-Cresol Cation. *Journal of the American Chemical Society*, 120(50):13256–13257, 1998.

[205] A. Ramírez-Hernández, C. Aguilar-Flores, and A. Aparicio-Saguilán. Fingerprint analysis of FTIR spectra of polymers containing vinyl acetate. *DYNA*, 86(209):198–205, 2019.

[206] S. Ghorai, A. Laskin, and A. V. Tivanski. Spectroscopic evidence of keto−enol tautomerism in deliquesced malonic acid particles. *The Journal of Physical Chemistry A*, 115(17):4373–4380, 2011.

[207] J.S. Yoon, H.W. Jung, M.N. Kim, and E.S. Park. Diffusion coefficient and equilibrium solubility of water molecules in biodegradable polymers. *Journal of Applied Polymer Science*, 77(8):1716–1722, 2000.

[208] M. Gazińska, A. Krokos, B. Kryszak, P. Dzienny, M. Olejarczyk, P. Gruber, R. Kwiatkowski, and A. Antończak. Influence of thermal annealing on the sinterability of different grades of polylactide microspheres dedicated for laser sintering. *Materials*, 14(11):2999, 2021.

[209] F. Ramazani, W. Chen, C. F. van Nostrum, G. Storm, F. Kiessling, T. Lammers, W. E. Hennink, and R. J. Kok. Strategies for encapsulation of small hydrophilic and amphiphilic drugs in PLGA microspheres: State-of-the-art and challenges. *International Journal of Pharmaceutics*, 499(1-2):358–367, 2016.

[210] H. K. Kim and T. G. Park. Comparative study on sustained release of human growth hormone from semi-crystalline poly(l-lactic acid) and amorphous poly(d,l-lactic-co-glycolic acid) microspheres: Morphological effect on protein release. *Journal of Controlled Release*, 98(1):115–125, 2004.

[211] Yi-Yan Yang, Tai-Shung Chung, Xin-Lai Bai, and Woon-Khiong Chan. Effect of preparation conditions on morphology and release profiles of biodegradable polymeric microspheres containing protein fabricated by double-emulsion method. *Chemical Engineering Science*, 55(12):2223–2236, 2000.

[212] Y. Hua, Y. Su, H. Zhang, N. Liu, Z. Wang, X. Gao, J. Gao, and A. Zheng. Poly(lactic-co-glycolic acid) microsphere production based on quality by design: A review. *Drug Delivery*, 28(1):1342–1355, 2021.

[213] J. Zhou, J. Walker, R. Ackermann, K. Olsen, J. K. Y. Hong, Y. Wang, and S. P. Schwendeman. Effect of manufacturing variables and raw materials on the composition-equivalent PLGA microspheres for 1-month controlled release of leuprolide. *Molecular Pharmaceutics*, 17(5):1502–1515, 2020.

[214] G. Tamburini, S. Bertagnoli, G. Tarricone, S. Piva, A. Sassella, R. Lorenzi, and A. Paleari. Early stages of X-ray induced molecular unit modifications in poly(lactic acid). *Polymer Degradation and Stability*, 216:110485, 2023.

[215] K. Shi, G. Liu, H. Sun, B. Yang, and Y. Weng. Effect of biomass as nucleating agents on crystallization behavior of polylactic acid. *Polymers*, 14(20):4305, 2022.

[216] G. Liu, X. Zhang, and D. Wang. Tailoring Crystallization: Towards High-Performance Poly(lactic acid). *Advanced Materials*, 26(40):6905–6911, 2014.

[217] B. Ma, H. Zhang, K. Wang, H. Xu, Y. He, and X. Wang. Influence of scPLA microsphere on the crystallization behavior of PLLA/PDLA composites. *Composites Communications*, 21:100380, 2020.

[218] J. Bao, X. Dong, S. Chen, W. Lu, X. Zhang, and W. Chen. Confined crystallization, melting behavior and morphology in PEG-b-PLA diblock copolymers: Amorphous versus crystalline PLA. *Journal of Polymer Science*, 58(3):455–465, 2020.

[219] K. Chrissopoulou, K. S. Andrikopoulos, S. Fotiadou, S. Bollas, C. Karageorgaki, D. Christofilos, G. A. Voyiatzis, and S. H. Anastasiadis. Crystallinity and chain conformation in PEO/layered silicate nanocomposites. *Macromolecules*, 44(24):9710–9722, 2011.

[220] M. Radjabian, M. H. Kish, and N. Mohammadi. Structure–property relationship for poly(lactic acid) (PLA) filaments: Physical, thermomechanical and shape memory characterization. *Journal of Polymer Research*, 19(6), 2012.

[221] J. M. Carr, D. S. Langhe, M. T. Ponting, A. Hiltner, and E. Baer. Confined crystallization in polymer nanolayered films: A review. *Journal of Materials Research*, 27(10):1326–1350, 2012.

[222] A. Narladkar, E. Balnois, G. Vignaud, and Y. Grohens. Difference in Glass Transition Behavior Between Semi Crystalline and Amorphous poly(lactic acid) Thin Films. *Macromolecular Symposia*, 273(1):146–152, 2008.

[223] R. M. Michell and A. J. Müller. Confined crystallization of polymeric materials. *Progress in Polymer Science*, 54-55:183–213, 2016.

[224] T. L. Nguyen, F. Bédoui, P.-E. Mazeran, and M. Guigon. Mechanical investigation of confined amorphous phase in semicrystalline polymers: Case of PET and PLA. *Polymer Engineering and Science*, 55(2):397–405, 2014.

[225] R. Androsch, C. Schick, and M. L. Di Lorenzo. Kinetics of Nucleation and Growth of Crystals of Poly(l-lactic acid). In *Synthesis, Structure and Properties of Poly(lactic acid)*, pages 235–272. Springer International Publishing, Cham, 2017.

[226] H. Zhang, S. Xiang, Q. Luan, Y. Bao, Q. Deng, M. Zheng, S. Liu, J. Song, H. Tang, and F. Huang. Development of poly (lactic acid) microspheres and their potential application in Pickering emulsions stabilization. *International Journal of Biological Macromolecules*, 108:105–111, 2018.

[227] Y. Hong, C. Gao, Y. Shi, and J. Shen. Preparation of porous polylactide microspheres by emulsionsolvent evaporation based on solution induced phase separation. *Polymers for Advanced Technologies*, 16(8):622–627, 2005.

[228] S. Tcholakova, N. Politova, and N. Denkov. Kinetics of drop breakage and drop-drop coalescence in turbulent flow. *Biomath Communications*, 3(1), 2016.

[229] P. Taylor. Ostwald ripening in emulsions. *Advances in Colloid and Interface Science*, 75(2):107–163, 1998.

[230] Y. Kong, A. Nikolov, and D. Wasan. Emulsion stability in the presence of nonionic surfactant micelles: Role of micellar ordering and Ostwald Ripening. *Industrial and Engineering Chemistry Research*, 49(11):5299–5303, 2010.

[231] J. Liu, W. Zhao, Z. Lun, Y. Zhang, Q. Zhang, P. Yang, Y. Li, and C. Sun. Factors and kinetics related to the formation of heavy oil-in-water emulsions. *Energies*, 16(14):5499, 2023.

[232] Y.-Y. Yang, H.-H. Chia, and T.-S. Chung. Effect of preparation temperature on the characteristics and release profiles of PLGA microspheres containing protein fabricated by double-emulsion solvent extraction/evaporation method. *Journal of Controlled Release*, 69(1):81–96, 2000.

[233] M. C. Righetti, M. Gazzano, M. L. Di Lorenzo, and R. Androsch. Enthalpy of melting of α- and α-crystals of poly(l-lactic acid). *European Polymer Journal*, 70:215–220, 2015.

[234] M. L. Di Lorenzo and R. Androsch. Influence of α/α'crystal polymorphism on properties of poly(l-lactic acid). *Polymer International*, 68(3):320–334, 2018.

[235] D. Vadas, Z. K. Nagy, I. Csontos, G. Marosi, and K. Bocz. Effects of thermal annealing and solvent-induced crystallization on the structure and properties of poly(lactic acid) microfibres produced by high-speed electrospinning. *Journal of Thermal Analysis and Calorimetry*, 142(2):581–594, 2020.

[236] M. Cocca, M. L. Di Lorenzo, M. Malinconico, and V. Frezza. Influence of crystal polymorphism on mechanical and barrier properties of poly(l-lactic acid). *European Polymer Journal*, 47(5):1073–1080, 2011.

[237] T. Nakanishi, J. Xu, N. Hirosaki, and T. Takeda. Thermostable europium polymer crystalline spherical beads and their photophysical properties. *Sensors and Materials*, 35(2):529, 2023.

[238] A. Nakajima, T. Nakanishi, Y. Kitagawa, T. Seki, H. Ito, K. Fushimi, and Y. Hasegawa. Hyper-stable organo-EuIII luminophore under high temperature for photo-industrial application. *Scientific Reports*, 6(1), 2016.

[239] O. Essahili, A. El Azzaoui, M. Ilsouk, and O. Moudam. Investigating the long-term stability of photoluminescence lifetimes in PMMA films doped with β-diketonate europium complexes based on bipyridine and terpyridine derivatives. *Journal of Photochemistry and Photobiology A: Chemistry*, 447:115211, 2024.

[240] T. A. Kovacs, M. C. F.C. Felinto, T. B. Paolini, B. Ali, L. K.O. Nakamura, E. E.S. Teotonio, H.F. Brito, and O. L. Malta. Synthesis and photoluminescence properties of [Eu(dbm)3PX] and [Eu(acac)3PX] complexes. *Journal of Luminescence*, 193:98–105, 2018.

[241] Y. Hasegawa and Y. Kitagawa. Luminescent lanthanide coordination polymers with transformative energy transfer processes for physical and chemical sensing applications. *Journal of Photochemistry and Photobiology C: Photochemistry Reviews*, 51:100485, 2022.

[242] A. Nakajima, T. Nakanishi, Y. Kitagawa, K. Fushimi, and Y. Kasegawa. Thermosensitive luminescent lanthanide complex with two photosensitized ligands. *Sensors and Materials*, 28(8):845–850, 2016.

[243] G. Tamburini, G. Tarricone, S. Piva, A. Sassella, S. Bertagnoli, R. Lorenzi, and A. Paleari. Tuning crystallinity of poly(l-lactic acid) microspheres through emulsification temperature changes. *Macromolecules*, 57(18):8826–8836, 2024.

[244] T. Mehtiö, A. AnghelescuHakala, J. Hartman, V. Kunnari, and A. Harlin. Crosslinkable poly(lactic acid)based materials: Biomassderived solution for barrier coatings. *Journal of Applied Polymer Science*, 134(1), 2016.

[245] M. Hamoudeh, H. Fessi, H. Salim, and D. Barbos. Holmium-Loaded PLLA nanoparticles for intratumoral radiotherapy via the TMT technique: Preparation, characterization, and stability evaluation after neutron irradiation. *Drug Development and Industrial Pharmacy*, 34(8):796–806, 2008.

[246] B. Schrode, S. Pachmajer, M. Dohr, C. Röthel, J. Domke, T. Fritz, R. Resel, and O. Werzer. Gidvis: A comprehensive software tool for geometry-independent grazing-incidence X-ray diffraction data analysis and pole-figure calculations. *Journal of Applied Crystallography*, 52(3):683–689, 2019.

[247] R. Ilmi, S. Kansız, N. Dege, and M. S. Khan. Synthesis, structure, Hirshfeld surface analysis and photophysical studies of red emitting europium acetylacetonate complex incorporating a phenanthroline derivative. *Journal of Photochemistry and Photobiology A: Chemistry*, 377:268–281, 2019.

[248] H.-G. Liu, S. Park, K. Jang, W.-S. Zhang, H.-J. Seo, and Y.-I. Lee. Different photoluminescent properties of binary and ternary europium chelates doped in PMMA. *Materials Chemistry and Physics*, 82(1):84–92, 2003.

[249] K. Binnemans. Interpretation of europium(III) spectra. *Coordination Chemistry Reviews*, 295:1–45, 2015.

[250] W. Thor, A. N. Carneiro Neto, R.T. Moura, Jr., K.-L. Wong, and P. A. Tanner. Europium(III) coordination chemistry: Structure, spectra and hypersensitivity. *Coordination Chemistry Reviews*, 517:215927, 2024.

[251] C.F. Liang, E.J. Schmitschek, and J.A. Trias. I.R. and Raman spectra of europium(III) β-diketonates. *Journal of Inorganic and Nuclear Chemistry*, 32(3):811–831, 1970.

[252] V. Tsaryuk, V. Zolin, J. Legendziewicz, R. Szostak, and J. Sokolnicki. Effect of ligand radicals on vibrational IR, Raman and vibronic spectra of europium β-diketonates. *Spectrochimica Acta Part A: Molecular and Biomolecular Spectroscopy*, 61(1-2):185–191, 2005.

[253] S.F. Tayyari and F. Milani-nejad. Vibrational assignment of acetylacetone. *Spectrochimica Acta Part A: Molecular and Biomolecular Spectroscopy*, 56(14):2679–2691, 2000.

[254] R. Bonzanini, E.M. Girotto, M.C. Gonçalves, E. Radovanovic, E.C. Muniz, and A.F. Rubira. Effects of europium (III) acetylacetonate doping on the miscibility and photoluminescent properties of polycarbonate and poly(methyl methacrylate) blends. *Polymer*, 46(1):253–259, 2005.

[255] R. Bonzanini, D.T. Dias, E.M. Girotto, E.C. Muniz, M.L. Baesso, J.M.A. Caiut, Y. Messaddeq, S.J.L. Ribeiro, A.C. Bento, and A.F. Rubira. Spectroscopic properties of polycarbonate and poly(methyl methacrylate) blends doped with europium (III) acetylacetonate. *Journal of Luminescence*, 117(1):61–67, 2006.

[256] P. Ekholm, L. Virkki, M. Ylinen, L. Johansson, and P. Varo. Effects of natural chelating agents on the solubility of some physiologically important mineral elements in oat bran and oat flakes. *Cereal Chemistry*, 77(5):562–566, 2000.

[257] J. Stary and J. O. Liljenzin. Critical evaluation of equilibrium constants involving acetylacetone and its metal chelates. *Pure and Applied Chemistry*, 54(12):2557–2592, 1982.

[258] S. Teixeira, K. M. Eblagon, F. Miranda, M. F. R. Pereira, and J. L. Figueiredo. Towards controlled degradation of poly(lactic) acid in technical applications. *C*, 7(2):42, 2021.

[259] B. Ravel and M. Newville. ATHENA,ARTEMIS,HEPHAESTUS: Data analysis for X-ray absorption spectroscopy usingIFEFFIT. *Journal of Synchrotron Radiation*, 12(4):537–541, 2005.

[260] D. F. Parra, H. F. Brito, J. D.R. Matos, and L. C. Dias. Enhancement of the luminescent intensity of the novel system containing Eu3+βdiketonate complex doped in the epoxy resin. *Journal of Applied Polymer Science*, 83(12):2716–2726, 2002.

[261] P. Mandal, J. Kretzschmar, and B. Drobot. Not just a background: ph buffers do interact with lanthanide ions—a Europium(III) case study. *JBIC Journal of Biological Inorganic Chemistry*, 27(2):249–260, 2022.

[262] L. Labrador-Páez, M. Pedroni, P. Haro-González, E. Camarillo, M. Bettinelli, D. Jaque, and J. García-Solé. Eu^{3+} luminescent ions detect water density anomaly. *Journal of Luminescence*, 223:117263, 2020.

[263] F. d'Acapito, G. O. Lepore, A. Puri, A. Laloni, F. La Manna, E. Dettona, A. De Luisa, and A. Martin. The LISA beamline at ESRF. *Journal of Synchrotron Radiation*, 26(2):551–558, 2019.

[264] B. M. Walsh. Judd-Ofelt theory: Principles and practices. In *Advances in Spectroscopy for Lasers and Sensing*, pages 403–433, Dordrecht, 2006. Springer Netherlands.

[265] B R Judd. Charge transfer and crystal-field theory for rare-earth ions. *Journal of Physics C: Solid State Physics*, 13(14):2695–2701, 1980.

[266] G. S. Ofelt. Intensities of crystal spectra of rare-earth ions. *The Journal of Chemical Physics*, 37(3):511–520, 1962.

[267] G. S. Ofelt. Structure of the f6 Configuration with Application to Rare-Earth Ions. *The Journal of Chemical Physics*, 38(9):2171–2180, 1963.

[268] C. Görller-Walrand and K. Binnemans. Chapter 167 Spectral intensities of f-f transitions. In *Handbook on the Physics and Chemistry of Rare Earths*, pages 101–264. Elsevier, 1998.

[269] X. Shangda and C. Yimin. Effect of J-mixing on the intensities of f-f transitions of rare earth ions. *Journal of Luminescence*, 31-32:204–206, 1984.

[270] A F. Kirby and F. S. Richardson. Detailed analysis of the optical absorption and emission spectra of europium(3+) in the trigonal (C3) Eu(DBM)3.H2O system. *The Journal of Physical Chemistry*, 87(14):2544–2556, 1983.

[271] C. Görller-Walrand, L. Fluyt, A. Ceulemans, and W. T. Carnall. Magnetic dipole transitions as standards for Judd–Ofelt parametrization in lanthanide spectra. *The Journal of Chemical Physics*, 95(5):3099–3106, 1991.

[272] B. Bondzior and P. J. Dereń. The role of hypersensitive transition in Eu3+ optical probe for site symmetry determination in BaScBO-SrScBO solid-solution phosphor. *Journal of Luminescence*, 201:298–302, 2018.

[273] G. Blasse. Luminescence from the EU3+ ion in D4d symmetry. *Inorganica Chimica Acta*, 142(1):153–154, 1988.

LIST OF CONTRIBUTIONS

Publications and Conferences

- G. Tamburini, S. Bertagnoli, G. Tarricone, S. Piva, A. Sassella, R. Lorenzi, A. Paleari. Early stages of X-ray induced molecular unit modifications in poly(lactic acid). *Polym. Degrad. Stab.* **2023** 216, 110485.

- G. Tamburini, S. Bertagnoli, G. Tarricone, S. Piva, A. Sassella, R. Lorenzi, A. Paleari. Tuning crystallinity of poly(L-lactic acid) microspheres through emulsification temperature changes. *Macromolecules* **2024** 57(18), 8826–8836.

- Winter school: Neutron and Synchrotron Radiation (NESY), Bad Aussee, Austria. Poster contribution: G. Tamburini, R. Lorenzi, F. Gasser, E. Machado Charry, R. Resel, A. Paleari, Crystallinity of Eu-doped Poly(L-lactic acid) Microspheres by Emulsification.

- Conference: Polymers for Sustainable Future 2024, Institute of Macromolecular Chemistry, Prague. Poster contribution: G. Tamburini, S. Bertagnoli, G. Tarricone, S. Piva, F. Gasser, E. Machado Charry, A. Sassella, R. Lorenzi, R. Resel, A. Paleari. Tuning the Crystallinity of Eu-Doped Poly(L-Lactic Acid) Microspheres for Tumor Treatments.

La borsa di dottorato cofinanziata con risorse del
Programma Operativo Nazionale Ricerca e Innovazione 2014-2020 (CCI 2014IT16M2OP005),
risorse Fondo Sociale Europeo REACT-EU, Azione I.1 "Dottorati Innovativi con caratterizzazione industriale", Azione IV.4 "Dottorati e contratti di ricerca su tematiche dell'innovazione" e Azione IV.5 "Dottorati su tematiche Green"

UNIONE EUROPEA
Fondo Sociale Europeo
Ministero dell'Università e della Ricerca
PON RICERCA E INNOVAZIONE 2014 - 2020
REACT EU
UNIVERSITÀ DEGLI STUDI DI MILANO BICOCCA